30255

National Library of Canada / Bibliothèque nationale du Canada

CANADIAN THESES ON MICROFICHE / THÈSES CANADIENNES SUR MICROFICHE

NAME OF AUTHOR/*NOM DE L'AUTEUR* Hendrik P.W.L. Blok

TITLE OF THESIS/*TITRE DE LA THÈSE* Fission of Medium Mass Nuclei

UNIVERSITY/*UNIVERSITÉ* Simon Fraser University

DEGREE FOR WHICH THESIS WAS PRESENTED/*GRADE POUR LEQUEL CETTE THÈSE FUT PRÉSENTÉE* Doctor of Philosophy

YEAR THIS DEGREE CONFERRED/*ANNÉE D'OBTENTION DE CE DEGRÉ* 1976

NAME OF SUPERVISOR/*NOM DU DIRECTEUR DE THÈSE* Professor Brian D. Pate

Permission is hereby granted to the NATIONAL LIBRARY OF CANADA to microfilm this thesis and to lend or sell copies of the film.

The author reserves other publication rights, and neither the thesis nor extensive extracts from it may be printed or otherwise reproduced without the author's written permission.

L'autorisation est, par la présente, accordée à la BIBLIOTHÈQUE NATIONALE DU CANADA de microfilmer cette thèse et de prêter ou de vendre des exemplaires du film.

L'auteur se réserve les autres droits de publication; ni la thèse ni de longs extraits de celle-ci ne doivent être imprimés ou autrement reproduits sans l'autorisation écrite de l'auteur.

DATED/*DATÉ* Nov 3 1975 SIGNED/*SIGNÉ*

PERMANENT ADDRESS/*RÉSIDENCE FIXE*

[redacted]

NL-91 (11-73)

FISSION OF MEDIUM MASS NUCLEI

by

HENDRIK PIETER WILLEM LODEWIJK BLOK

ing. (chem. eng.) H.T.S. Dordrecht, Holland, 1967

M.Sc., University of Saskatchewan, 1970

A DISSERTATION SUBMITTED IN PARTIAL FULFILLMENT

OF THE REQUIREMENTS FOR THE DEGREE OF

DOCTOR OF PHILOSOPHY

in the Department

of

Chemistry

SIMON FRASER UNIVERSITY

September 1975

APPROVAL

Name: Hendrik Pieter Willem Lodewijk Blok

Degree: Doctor of Philosophy

Title of Thesis: Fission of Medium Mass Nuclei

Examining Committee

Chairman: A.C. Oehlschlager

B.D. Pate, Professor
Senior Supervisor

R.G. Korteling, Associate Professor

D. Sutton, Associate Professor

I.M. Thorson, Research Associate

T.T. Sugihara, Professor of Chemistry
Texas A&M University
College Station, Texas, U.S.A.

Date Approved: October 10, 1975

PARTIAL COPYRIGHT LICENSE

I hereby grant to Simon Fraser University the right to lend my thesis or dissertation (the title of which is shown below) to users of the Simon Fraser University Library, and to make partial or single copies only for such users or in response to a request from the library of any other university, or other educational institution, on its own behalf or for one of its users. I further agree that permission for multiple copying of this thesis for scholarly purposes may be granted by me or the Dean of Graduate Studies. It is understood that copying or publication of this thesis for financial gain shall not be allowed without my written permission.

Title of Thesis/Dissertation:

Fission of Medium Mass Nuclei

Author:

(signature)

Hendrik P.W.L. Blok

(name)

Nov 3 1975

(date)

Abstract

The feasibility of using mica track detectors in a detailed study of the fission of medium mass nuclei has been explored. Extensive calibration of mica as a heavy ion detector was achieved by measuring the track length of heavy ions with a series of known mass, charge and energy values. The results of these studies were compared with the conventional theoretical stopping models. No satisfactory agreement could be obtained and a semi-empirical relation was derived which describes the track length of heavy ions in mica to within the accuracy of the experimental measurements.

Track length distributions of fission fragments as a function of the angle of emission with respect to the beam of bombarding particles were measured for the following systems: 167-MeV α's + Mo, In and Au; 80-MeV α's + Ag, Te and Au; and 100-MeV and 120-MeV α's + Au. The data were analysed in terms of the total kinetic energy release, center-of-mass motion and the width of the mass and/or energy distribution of the fission fragments. Kinetic energy release values were found to be systematically higher than theoretical estimates. The analysis did not support a dramatic increase in the width of the mass distribution of the fragments from fissioning systems of mass decreasing to that of the 80-MeV α's + Ag system, but was inconclusive with respect to this effect for the 167-MeV α's + Mo system.

In the analysis of angular distribution data, distributions in angular momentum and excitation energy of the fissioning nuclei were obtained by calculating the competition between particle emission and fission in the de-excitation of the excited nuclei, and including the effects of multiple chance fission. Deduced values of the moments of inertia of the saddle point configurations were compared with theoretical predictions.

Acknowledgements

It is with great pleasure that the author wishes to express his gratitude to Professor Brian D. Pate for his continued guidance and extreme patience during the course of this work.

Special appreciation is also due to Dr. F. Michael Kiely for sharing in the tedious task of scanning the mica detectors from the calibration experiments. The many discussions have been very helpful in the completion of this work.

Thanks are also due to

Dr. J. Péter for the arrangement of the many irradiations at Orsay and his numerous helpful suggestions;

L. Lecerf and F. Hanappe for performing the Orsay irradiations and preparing the targets and detectors for those experiments.

Professors T.T. Sūgihara and J.B. Natowitz for their assistance during the TAMVEC runs, and the staff of the Texas A & M University cyclotron for their hospitality during the spring of 1971 and 1972. Special thanks are also due to Professor J.B. Natowitz for supplying a version of the KNOTTY computer program and for lending his scattering chamber during the course of the irradiations;

Dr. J. Grabowski for his many helpful suggestions in writing the evaporation-fission competition program as well as for providing versions of the optical model code DWUCKY and the evaporization code ALICE;

The staff of the Simon Fraser University Computer Center for assisting in carrying out the many calculations;

The faculty and staff of the Chemistry Department of Simon Fraser University and, especially, the nuclear group for providing fellowship and encouragement;

And; the National Research Council for supporting this work through Grant Number A2510 as well as through a Postgraduate Scolarship to the Author.

TABLE OF CONTENTS

List of tables

List of figures

Preface

Fission, more than any other topic in nuclear chemistry and physics, has aroused great public as well as scientific interest. In 1939 Hahn and Strassman discovered that uranium nuclei, after the seemingly minor excitation caused by the absorption of a low energy neutron, often split up into two large fragments, releasing a comparatively very large amount of energy. It was this excessive amount of energy released by such a very small quantity of material that stirred the imagination of many minds and has resulted in the great benefits for today's society, as well as, the ever present fear and anxiety that will linger on as long as the destructive capabilities of the fission process are utilized by even a few.

It is undeniable, however, that because of the presence of other than just scientific motivation the knowledge of the fission process has advanced at an enormous rate, thereby also increasing our understanding of nuclear physics and chemistry in general. Whether this increase in knowledge will pay off the debt that fission so obviously owes us, is a question that we must answer for ourselves.

With the rapid advances being made in the construction of medium and high energy particle accelerators, fission can now be induced in nearly all elements known to man. The fission process of medium mass nuclei (here quite arbitrarily defined

as the fission of nuclei with a mass of around 50 to 200 amu) still releases a large amount of energy, but in order to induce the event an equal or larger amount of energy is required. From an industrial point of view then, the process is not useful. However, a study of the medium mass fission process can illuminate the fission process generally and particularly the influence of larger amounts of excitation energy and angular momentum.

Chapter 1 Introduction

1.1 Fission of medium mass nuclei at moderate excitations.

Theoretical as well as experimental studies of the fission process concentrate mainly on the heavier fissioning nuclei, although most of the treatments have also been extended for nuclei of medium masses. (Here we will quite arbitrarily define the light nuclei as being those with a mass of less than 50 amu, the medium mass nuclei as those with a mass between 50 and 200 amu and the heavier nuclei as those with a mass heavier than 200 amu.) The earliest theoretical studies were mainly concerned with a determination of fission barriers (Mei 39, Boh 39, Pre 40, Pre 46, Fra 47). The uniformly charged liquid drop model was used in all studies. The rationale for using this model was the same as that for use of the same model to calculate masses and mass differences via the semiempirical mass equation, although the liquid drop model for the fission process is simplified by the fact that a number of terms in the mass equation are independent of any distortion of the nucleus.

It soon became evident that in order to agree with the experimental data that were available for some of the heavier nuclei, shell effects could not be excluded. (Mye 66, Str 67). Myers and Swiatecki (Mye 66) did extend their calculations to the region of medium mass nuclei as well, although, because of

a lack of experimental data, it has not been possible to confirm their theoretical estimates. Complicating any direct determination of the fission barriers of medium mass nuclei is the fact that the few theoretical estimates of the shape of the fission barrier that have been made (Nix 67) indicate a dramatic narrowing of the fission barrier for fissility parameters less than 0.65. (The fissility parameter x is defined as the ratio of the coulomb energy of a spherical drop to twice its surface energy, $x = z^2/50.13A$, where z and A are the charge and the mass of the nucleus respectively.) The narrow fission barriers will allow a considerable amount of barrier penetration as well as reflection. From an experimental point of view, this effect will show up in a rather slow variation of the fission cross section, even in the neighborhood of the fission barrier.

In the previously mentioned theoretical studies, the angular momentum of the fissioning nucleus is assumed to be zero. However, with the fission barriers for nuclei with a mass of 50 to 150 amu expected (Mye 66) to be in the order of 50 MeV, a considerable amount of excitation energy has to be induced in the nucleus in order for it to be able to fission. By bombarding the nucleus with 60 MeV alpha particles for example, this excitation energy can be reached but a considerable amount of angular momentum is also induced. The theory of a rotating liquid drop had already been considered around the early

1960's (Pik 58, Pik 62, Pik 62b, Ber 61, His 60) but a complete treatment of this theory was not described until very recently. Cohen et.al (Coh 74) found that the fission barrier will decrease with increasing amounts of angular momentum, and even vanish if sufficient angular momentum is induced in the nucleus.

In order to simplify the treatment of the medium mass fission process, a number of different steps or stages are assumed to take place in the following order (also see Fig. 1.1):

1. The incident particle either forms a "composite" system (Coh 74) with the target nucleus, (in this system the target and projectile have more or less amalgamated, but equilibrium in all degrees of freedom has not been achieved) or an elastic or inelastic scattering, stripping or simple nucleon transfer process occurs. Here we will assume that the residual nucleus of any of these latter interactions will have a much lower excitation energy than the result of complete amalgamation, relative to the expected (Mye 66, Coh 74) fission barrier and hence will not lead to an appreciable contribution to the total probability for any type of fission reaction.

2. The composite nucleus can decay by pre-equilibrium particle emission (Gri 66, Bla 68, Bla 70, Bla 71), or it can undergo "direct" or pre-equilibrium fission. If the composite

nucleus survives long enough to attain equilibrium in all degrees of freedom, the compound nucleus is formed. Residual nuclei from the pre-equilibrium decay process may also eventually attain an equilibrium state, and if sufficient excitation energy remains, the nuclei can still de-excite via the fission process.

3. The compound nucleus can decay by a competition between particle evaporation and fission. The slower gamma de-excitation has been neglected in this scheme.

Most of the earlier experimental studies of the medium mass fission process were for nuclei with masses close to 200 amu.

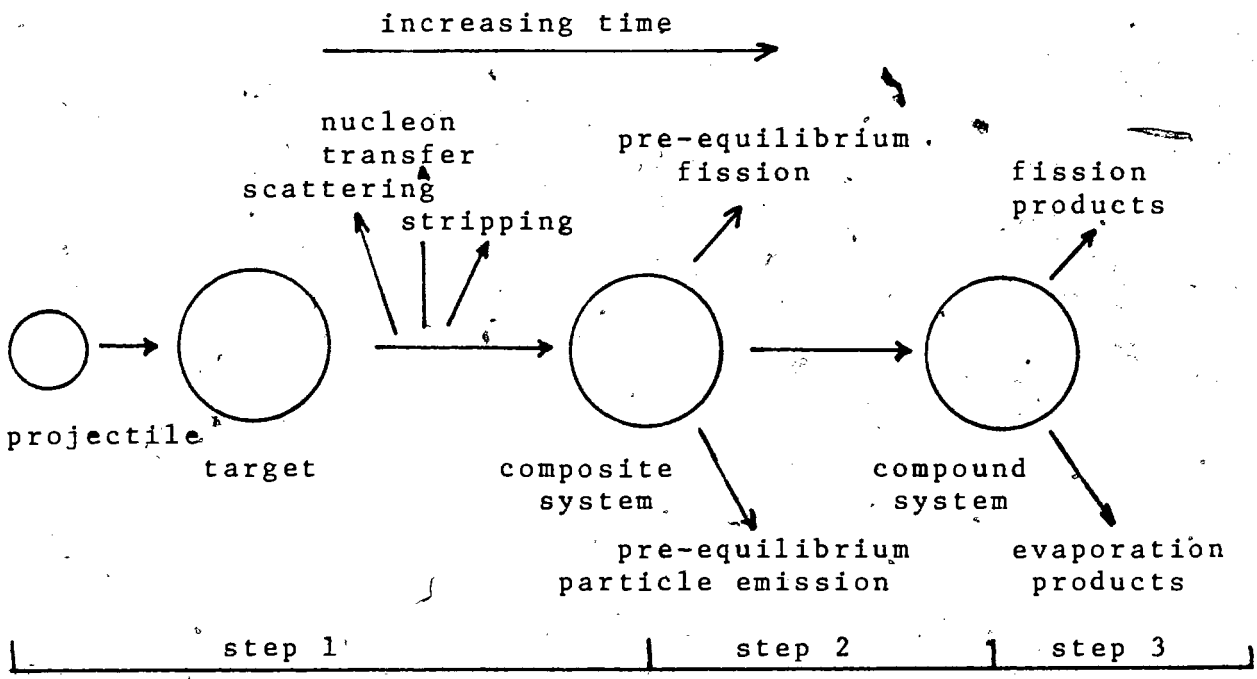

Figure 1.1 Sequence of events for a moderate energy incident particle interacting with a medium mass nucleus.

Fission barriers in this region are only in the order of 20 MeV, and consequently, the excitation energies employed were commonly no more than 50 MeV. (Cha 62, Hui 62, Bur 64).

The reaction scheme of figure 1.1 was simplified considerably in application to those cases. Compound nucleus formation was always assumed, while in the de-excitation of the compound nucleus, only first chance fission was taken into account. Multiple chance fission as well as angular momentum effects were considered from an experimental point of view in the mid sixties (Kho 66), but not until the seventies were these effects properly taken into account. (Bla 73, Pla 73, Fer 73).

Although the theory of pre-equilibrium particle emission has been developed to some extent (Bla 71), it has not been quantitatively applied towards the interpretation of any experimental data on the fission of medium mass nuclei. Hence, although some theoretical models exist to describe all three steps in figure 1.1, the interpretation of experimental data still basically assumes that a compound (or at least equilibrated) system is formed which then decays via particle evaporation or fission. The inherent difficulty in including pre-equilibrium decay is that in order to analyse the angular distributions of fission fragments, one needs to know the distribution in angular momentum of the fissioning nuclei, and all pre-equilibrium decay models in existence today do not

implicitly retain the angular momentum distribution information. Justification for the assumption of compound nucleus formation (i.e. full momentum transfer) has been sought from measurements of angular correlation functions (Sik 62, Vio 71, Pla 73, Vio 74). Although these types of measurements do not indicate a significant departure from full momentum transfer, other researchers using different techniques have come to different conclusions (Bim 71).

But even if one assumes full momentum transfer, this still does not imply a knowledge of the initial angular momentum distribution. For reactions occuring well above the Coulomb barrier, it has been argued that there exists a centrifugal limitation to the complete fusion of target and projectile (Wil 73, Bas 73, Nat 72, Nat 70, Zeb 74). Although these arguments were based on the interpretation of data from heavy ion interactions, it has recently been shown (Vio 74) to apply also to the lighter alpha particles.

All the above illustrates the confusion that is present whenever one attempts to interpret the experimental data from a medium mass fission process. The uncertainty about entrance as well as exit channels of the reaction, coupled with the uncertainty of even the actual fission step itself (as illustrated by the complexity of such a basic parameter as the fission barrier) necessitates a large amount of further experimental as well as theo-

retical work.

1.2 Scope of this work.

This work is an attempt to shed more light on the complex fission process. In it simultaneous measurement has been attempted of as many parameters of the fission process as possible. More specifically an attempt has been made to obtain information with regard to the distribution in mass and energy of the fission fragments, the angular distribution of the fission fragments as well as (by measuring the center-of-mass motion of the fragments) the kinetics of the reaction mechanism. The experimental technique used in this study is that of measuring the track length of fission fragments in solid state nuclear track detectors. Chapter 2 describes the use of mica as such a detector. Extensive calibration of this material as a heavy ion detector is shown to provide one with a suitable tool in the study of the fission of medium mass nuclei. In chapter 3 the experimental data on the fission of some medium mass nuclei induced by alpha particles ranging in energy from 80 to 167 MeV are presented, while in chapter 4 these data are used to extract such fission parameters as total kinetic energy release and center-of-mass motion of the fission fragments. Limits on the width of the fission fragment mass distribution are also deduced. In chapter 5 the angular distributions of the fission fragments are analysed and the rele-

vance of various theories describing entrance and exit channels of the process are discussed. Particular attention is paid to the applicability of the evaporation theory to the de-excitation of an equilibrated nucleus when a fission mode of decay is included.

Chapter 2 Track length of heavy ions in mica.

2.1 Dielectric nuclear track detectors.

Since its development in the early 1960's the dielectric nuclear track detector has been employed in numerous studies (Fle 65, Pri 71). Energetic charged particles leave a semi-permanent damage trail in the lattice of non-metals. These damage trails can often be observed using an electron microscope (Sel 59). Application of sufficient energy to the lattice usually restores the arrangement of the atoms to its original state. In a number of cases it is possible, however, to "fix" the damage trails, usually by applying a chemical etching solution, in which case use is made of the fact that the etching rate of a damaged region in a lattice is much greater than that of the surrounding region. The sensitivity or threshold of these detectors is defined as the minimum mass and/or energy of incident ions which is detectable, and hence deposits a certain critical amount of energy per unit path length into the lattice, so as to create enough damage to leave an etchable track. The characteristics of the lattice and in particular its response to the passage of the incident particle will therefore determine the sensitivity of the given detector material. Some plastics will record proton tracks (Var 70), whereas other media like mica, will only detect much heavier particles (Fle 65).

For the study of the fission process of medium mass elements a detector was needed which would not register the high flux of scattered incident particles and the large number of evaporation products which result from medium energy (≈100 MeV) interactions with these nuclei. Yet, the detector should have a very high efficiency for the registration of fission fragments. Furthermore the damage trails must be permanent. Since one is also interested in relating the length of damage trails to the energies and masses of the fragments causing them, the calibration data on the response of the detector material to heavy charged particles must be available.

Calibration studies of the kind mentioned above have only been done on a limited scale for a few detector materials (Lec 71, Ral 69, Ben 69, Höp 69, Ral 71). Ralarosy et al (Ral 69, Ral 71) studied the track length of charged particles in makrofol. This plastic detects nearly all charged particles, including α-particles and even neutrons (Joz 71). It is therefore, not suitable for our purpose. Benton and Henke (Ben 69) developed semi-empirical range-energy relations for dielectric nuclear track detectors and compared their calculations with some measurements in cellulose nitrate. They found good agreement at high energies, but significant discrepancies in the energy range of fission fragments. Höppner et al (Höp 69) tried to correlate the diameter of tracks in plastics with the mass and energy of the incident fragments. Their

calibration data, however, are based only on the "heavy and light" mass peaks of the fission fragments of ^{235}U. Lecerf (Lec 71) measured the diameter-energy relationship of various energetic heavy ions in glass detectors, the work proceeding at the same time that the present study was undertaken. For the present purpose it was felt desirable to measure track length values rather than diameters, since the earlier study by Höppner (Höp 69) had indicated that there was only a slight mass dependence for the diameter of fission fragment tracks in plastics.

Only if the geometry of the tracks can be related to the path of the ion penetrating the detector material, can useful information be obtained from the measurement of track lengths. Henke and Benton (Hen 71) made a detailed study of the geometry of tracks in plastic detectors, with special attention to the determination of the range of the fragment in the detector material from the final shape of the etched track. Because of the small difference between the etching rate of the damaged and non-damaged regions, the shape of the etched tracks in plastics is critical, and the range of the fragment entering the plastic cannot be determined by measuring the length of the track alone. For a detector material with a much greater difference in the etching rate between the damaged and non-damaged regions, the shape of the tracks will be more cylindrical, and hence track length and range will be more closely

related. No adequate theoretical model has been developed which will predict the shape of the etched track (Bec 68), and an empirical method must be followed to determine the shape of the tracks and to correlate them to the original damage trail.

Muscovite mica with a reported (Fle 64) detection threshold of around 10 MeV.cm^{2}mg^{-1} (which translates to the ability of mica to detect only those fragments that can lose more than 10 MeV of energy per mg/cm^2 while travelling through the mica, i.e. fragments heavier than neon), and in which the tracks are cylindrical in shape (Fle 64), satisfies the requirements of a fission fragment detector.

In the following the "calibration" (relation of the shape and size of the track to the mass and charge of the incident ion) of mica is described.

2.2 Experimental techniques

The objective of the calibration experiments was to obtain sufficient data on the track length in mica of heavy ions of given masses and energies, in order to be able to extrapolate and interpolate these data with enough confidence over the entire spectrum of fission fragments masses and energies covered in this study. The main problem in such an experiment is to obtain various heavy ions in that mass range that have energies ranging from 0.1 to 1.5 MeV/amu.

2.2.1 Rutherford scattering experiments

If the energy of a beam of heavy ions, which is directed at a film of target material, is less that the Coulomb barrier for that system, simple Rutherford scattering takes place. This makes it possible to calculate the exact energy of the scattered projectile and target nuclei at a given angle of observation. This was the basis for an experiment that was performed with beams of $^{20}_{10}Ne$, $^{40}_{18}Ar$ and $^{84}_{36}Kr$ for the linear accelerator injector to the Orsay heavy ion cyclotron, with the cooperation of J. Péter, F. Hanappe and M. Lecerf. Pieces of mica were mounted in a scattering chamber (Fig. 2.1) in such a way that scattered heavy ions arrived at the detector surface at an angle of 30°. The beams of heavy ions had a nominal energy of 1.11 MeV/amu (Gol 70) and just before entering the scattering chamber were collimated to a diameter of 3mm. The targets used in these experiments were mounted at an angle of 30° to the beam, and their composition and thickness are shown in Table II.1. After irradiation, the mica sheets were marked as to their position in the scattering chamber with respect to the target and the beam, and then shipped to Simon Fraser University without any further treatment. The integrated current of the beam was also supplied.

figure 2·1

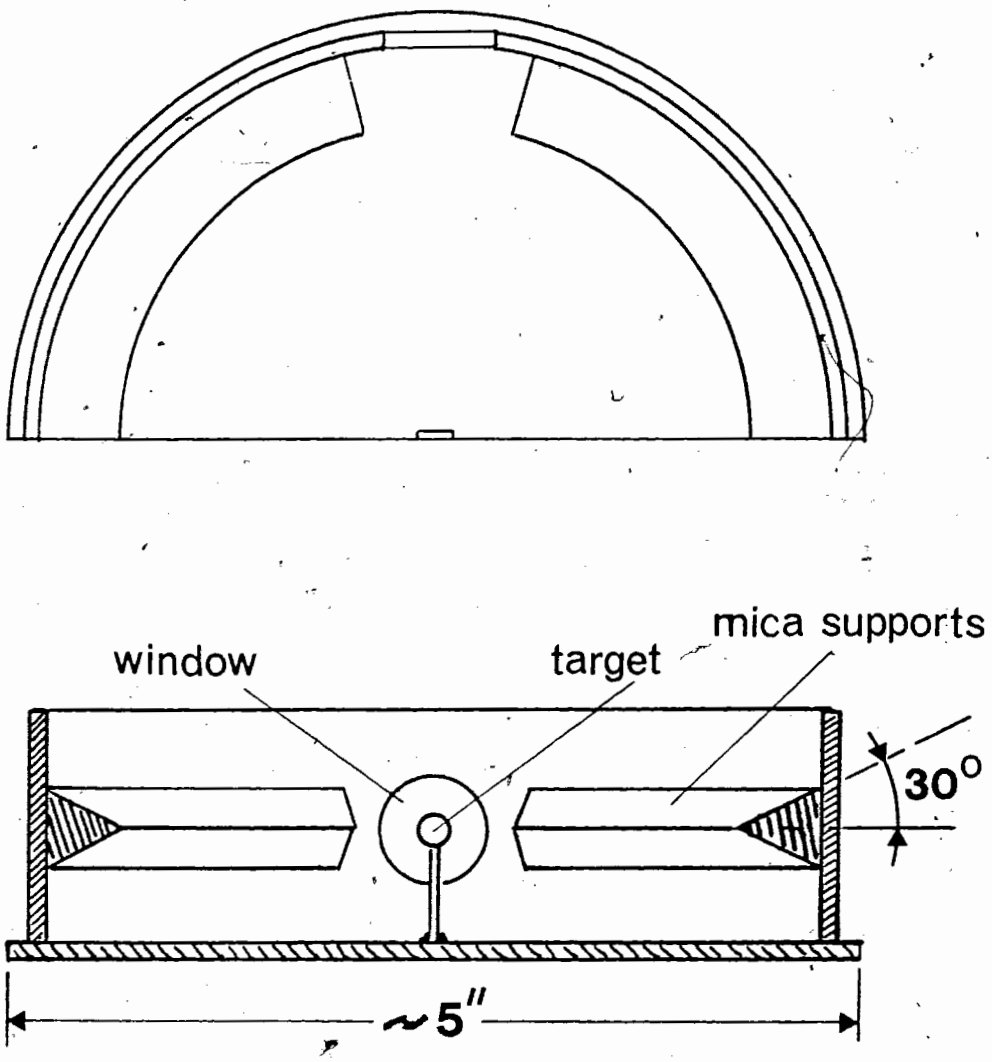

scattering chamber arrangement

Table II.1 Targets for the Rutherford Scattering Experiment

TARGET	COMPOSITION	THICKNESS ($\mu g/cm^2$)
Al	metal	180
Ca	CaF_2 on carbon	126 (Ca) + 71 (C)
Cr	metal on carbon	25 (Cr) + 100 (C)
Ni	metal	43 65
Se	metal on carbon	103 (Se) + 50 (C)
Ag	metal on carbon	50 (Ag) + 50 (C)
Au	metal	125 145

2.2.2 Etching conditions and the measurement of track length

The conditions required for formation of the optimum track profile were studied via some of the mica detectors on which were incident, the products from an irradiation of the aluminum target with a beam of Ne ions. The micas were etched in a 48% HF solution at 20°C for total times of 10, 15, 20, 40 and 60 minutes, and scanned with a Zeiss standard WL research Microscope with a total magnification of 1008X. The total projected length of each track within a given area of detector was measured using an eyepiece graticule calibrated via a Bauch and Lomb 0.01mm stage micrometer. Fig. 2.2 shows the track length distributions of the tracks measured at a laboratory angle of 27° to the Ne beam. The total area scanned

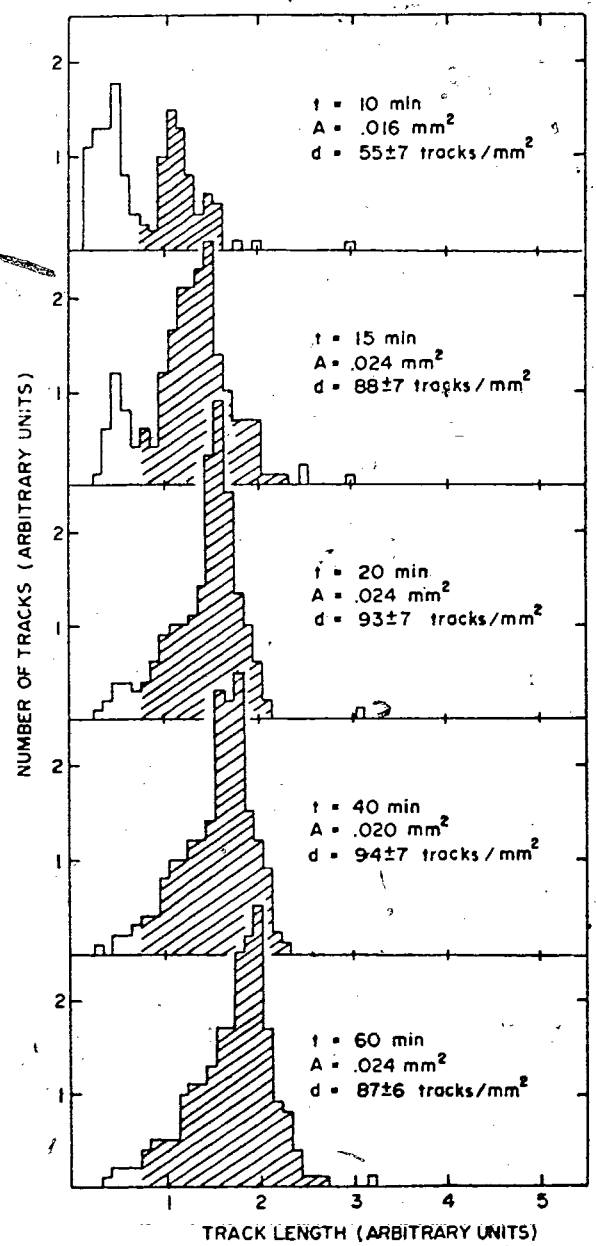
t = 10 min
A = .016 mm²
d = 55±7 tracks/mm²
t = 15 min
A = .024 mm²
d = 88±7 tracks/mm²
t = 20 min
A = .024 mm²
d = 93±7 tracks/mm²
t = 40 min
A = .020 mm²
d = 94±7 tracks/mm²
t = 60 min
A = .024 mm²
d = 87±6 tracks/mm²
NUMBER OF TRACKS (ARBITRARY UNITS)
TRACK LENGTH (ARBITRARY UNITS)

figure 2·2

as well as the density (tracks/mm^2) of tracks of length within the main peak of the distribution (shaded area) are also indicated. The average track length increases rapidly until the etching time is raised to 20 minutes. After that the track length only increases slightly, by an extent corresponding only to etching of unirradiated mica, while the number of tracks observed per unit area stays constant. Fig. 2.3 shows some typical tracks in mica. From this figure it can be seen that all the tracks are clearly cylindrical in shape, indicating that although it takes 20 minutes for the etchant to completely develop the track, the bulk etch rate (the etching rate of unirradiated mica) is much smaller in comparison. This makes it particularly easy to measure the actual length of the damage trail provided some correction can be made for the bulk etch rate. An estimate of the bulk etch rate was obtained by etching a large mica surface under the same conditions as mentioned above and measuring the weight loss as a function of etching time. The value obtained for the bulk etch rate of muscovite mica was $(8\pm1) \times 10^{-4}$ mg.cm^{-2} per 20 minute etching period. With the help of fig. 2.4 it can be seen that if we assume that points E and E' coincide, the corrected track length L for angle of incidence Ψ of the fragment is given by

$$L = (Lp' - d/2 \sin\Psi + t/\tan\Psi)/\cos\Psi \qquad (2.1)$$

where d is the diameter of the track, t is the surface area removed because of the bulk etching rate and Lp' is the pro-

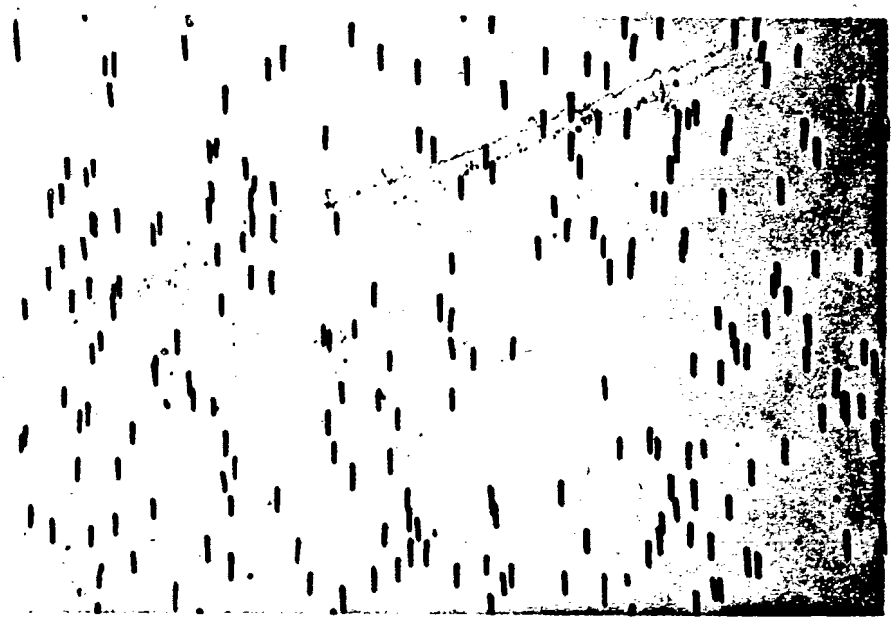

figure 2.3

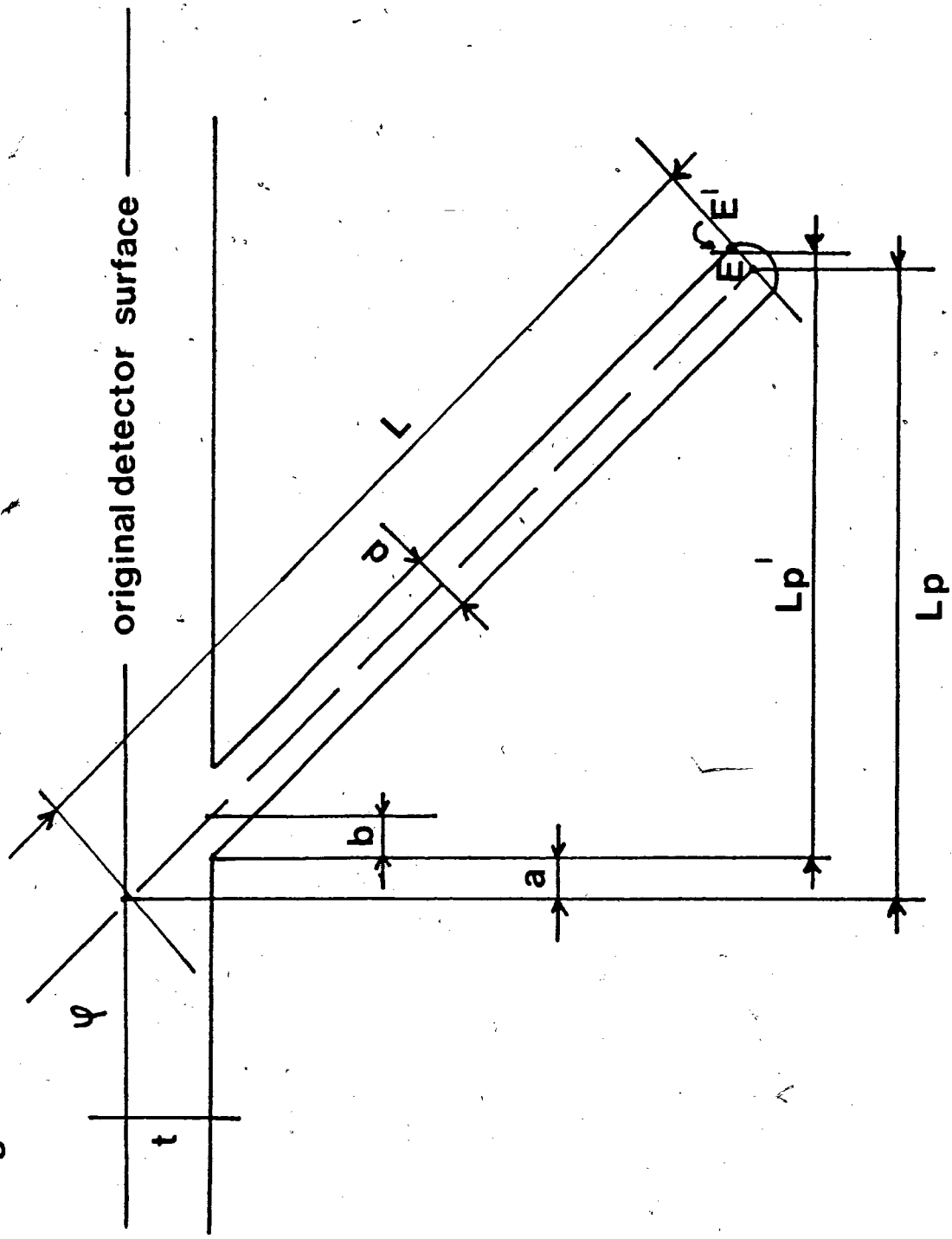

figure 2.4

jected length of the track as seen in a microscope. For most tracks the diameter d is less than 0.1 mg/cm^2 and the two correction factors tend to cancel each other out.

From these results it was decided to etch all mica detectors for 20 minutes in 48% hydrofluoric acid at 20^{o}C. Under these conditions the 'real track length' L is defined by equation (2.1) and will be identical to the length of the etchable damage trail that a fragment will leave in the mica detector.

Ten different fragment masses (7 targets plus 3 projectiles) were available for the calibration studies. Typically strips of detector surface corresponding to a laboratory angular interval of 1^{o} with respect to the beam direction were scanned so that the uncertainty in the incident energy of the fragments forming the tracks scanned was as small as possible. The data were plotted in the form of histograms of the number of tracks of a given measured track length. Some examples of these histograms are shown in figure 2.5.

2.3 Data Analysis

Conversion of the track length histograms to energy-mass-track length data was accomplished by calculation of the energies of the incident particles as a function of the angle of observation, and correlation of these to the average or most probable track length as measured at that angle. Energy calculations were

figure 2·5

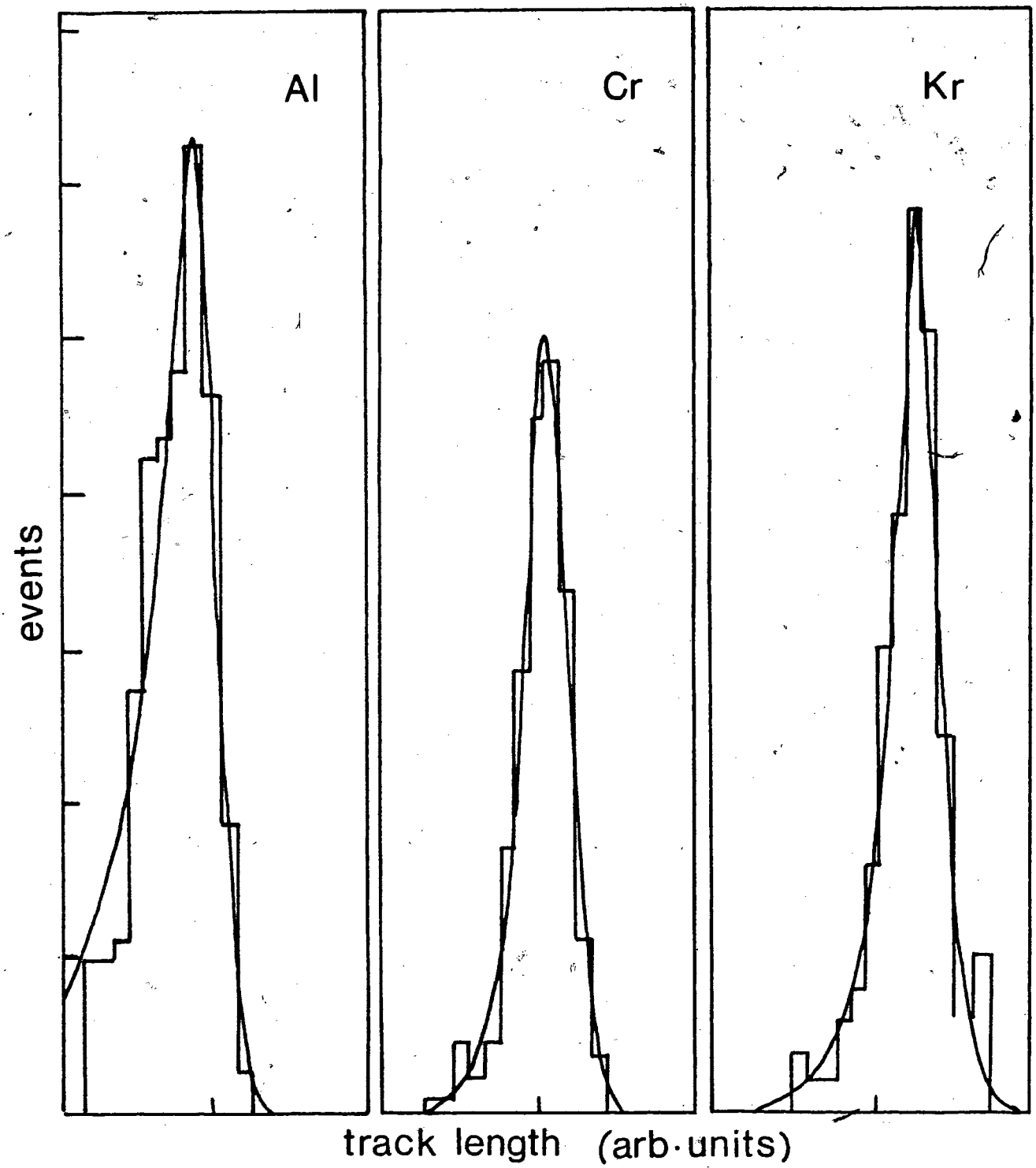

performed using the Rutherford scattering formulae (Rut 11).

$$E_1 = \frac{\{1 + (A_1/A_2)^2 + 2A_1\cos\theta_c/A_2\}\, E_i A_2^2}{(A_1 + A_2)} \qquad 2.2$$

$$E_2 = 2E_i (A_1/A_2)\ (1 + \cos\theta_c)\ \{A_2/(A_1 + A_2)\}^2 \qquad 2.3$$

where the subscripts 1 and 2 refer to the scattered projectile and target nuclei respectively; E is the center-of-mass energy of the scattered fragments, A is the mass of the fragments, E_i is the laboratory kinetic energy of the incident projectile, and θ_c is the center-of-mass scattering angle. The energies were converted to laboratory coordinates making use of the fact that the center-of-mass and laboratory scattering angles θ_c and θ_L are related by

$$\tan\theta_L = \frac{\sin\theta_c}{\cos\theta_c + \frac{A_1}{A_2}} \qquad 2.4$$

Hence for every angle of observation the energies were known of the fragments that were scattered into that direction. In order to distinguish the tracks of the projectile and target nuclei their relative intensity was also calculated, using Rutherford's well known result for the scattering cross section of a projectile in a central force field:

$$\frac{d\sigma_c}{d\Omega} = \frac{1}{4}\left(\frac{Z_1 Z_2 e^2}{2\mu E_i}\right)^2 \cdot \frac{1}{\sin^4(\theta_c/2)} \qquad 2.5$$

Where Z is the charge of the fragment, μ the reduced mass and e the electronic charge.

The laboratory energies of the fragments were corrected for the energy loss which they suffered while travelling through all (projectiles) or, on an average half (target nuclei) of the target film and backing material (if present). Specific energy loss values were obtained for this purpose from the tabulation due to Northcliffe and Schilling (Nor 70). (An interpolation procedure for these tables is discussed in section 4.1 and appendix 1.)

The average or most probable track length was determined by fitting the track length distribution to an appropriate analytical function. Since track length distributions are closely related to the range distributions of the fragments, the track length distributions show a certain amount of "tailing" towards lower length values. The analytical function used for fitting to the data was chosen, therefore, to be gaussian with excess probability towards lower values of track length:

$$P(L) = P_{MAX} \exp\{ T^2(2L - 2\bar{L} + T^2) / 2\rho^2\}$$

$$\text{for } L < (\bar{L} - T^2)$$

$$P(L) = P_{MAX} \exp \{-(L - \bar{L})^2 / 2\rho^2\} \qquad (2.6)$$

$$\text{for } L \geq (\bar{L} - T^2)$$

where P_{MAX} is the maximum height of the distribution, $\bar{L}$ is the corresponding most probable track length, T is a "tailing" parameter and ρ defines the width of the gaussian part of the distribution (ρ = FWHM/2.355).

Some of the track length distributions were measured to rather poor statistical precision. If the shape parameters ρ and T are, however, known from other experiments, a meaningful fit to these data can still be obtained. The general shape of the distribution was examined by fitting some sixteen track length distributions of good statistical precision to equation (2.6). These sixteen distributions were chosen so as to represent the entire range of masses and energies. Table II.2 shows the results. Also indicated in this table is the energy loss in MeV which the fragments will suffer while travelling through 50% of the target and, if present, the backing material. These values again were obtained from the data due to Northcliffe (Nor 70). It is to be expected that the width parameter ρ would vary some what with the energy loss of the penetrating ions in the target material. In Fig. 2.6 the width parameter ρ is given as a function of the estimated energy loss and it can be seen that any such dependence lies outside the accuracy of the present experiment. Similarly no depen-

Table II.2 the fitted shape parameters of sixteen representative track length distributions.

Element	energy MeV/amu	energy loss in ½ targ.	$\bar{L}$ (mg/cm^2)	P_{MAX}	T^2 (mg/cm^2)	ρ (mg/cm^2)	χ^2 (CHI squared)
Al (Ne-Al)	0.286	0.96	0.376±0.010	33.5±2.1	0.048±0.019	0.083±0.011	39.8
Al (Ne-Al)	0.412	1.04	0.579±0.003	45.3±1.5	0.044±0.007	0.061±0.004	24.4
Ar (Ar-Ni)	0.690	0.26	1.574±0.008	14.5±1.4	0.054±0.026	0.060±0.009	11.8
Ar (Ar-Au)	1.050	0.42	2.232±0.003	16.0±0.6	0.085±0.022	0.070±0.004	4.7
Ca (Kr-Ca)	0.859	2.04	1.654±0.002	28.0±0.5	0.141±0.018	0.095±0.002	4.2
Ca (Kr-Ca)	1.260	2.10	2.472±0.006	12.5±0.7	0.077±0.025	0.078±0.007	9.1
Cr (Kr-Cr)	0.869	1.98	2.025±0.002	31.4±1.0	0.051±0.009	0.057±0.003	8.9
Cr (Kr-Cr)	1.021	1.98	2.242±0.002	23.8±0.5	0.063±0.009	0.059±0.002	2.6
Ni (Ne-Ni)	0.255	0.25	0.755±0.008	10.0±0.8	0.028±0.012	0.053±0.008	4.0
Ni (Kr-Ni)	0.480	0.50	1.491±0.005	19.9±0.9	0.069±0.018	0.076±0.006	7.3
Se (Kr-Se)	0.422	1.80	1.558±0.003	14.5±0.7	0.065±0.018	0.051±0.003	4.3
Se (Kr-Se)	0.582	2.08	1.945±0.004	15.3±0.9	0.062±0.028	0.050±0.005	6.1
Kr (Kr-Ag)	0.170	0.84	0.822±0.011	11.0±1.1	0.057±0.040	0.068±0.013	8.6
Kr (Kr-Ni)	0.600	0.69	2.017±0.006	20.5±1.2	0.045±0.014	0.066±0.007	18.8
Ag (Kr-Ag)	0.150	0.95	1.082±0.010	13.1±0.9	0.085±0.029	0.097±0.011	14.2
Au (Ar-Au)	0.099	0.30	0.922±0.008	17.8±1.2	0.042±0.017	0.068±0.009	7.8

figure 2.6

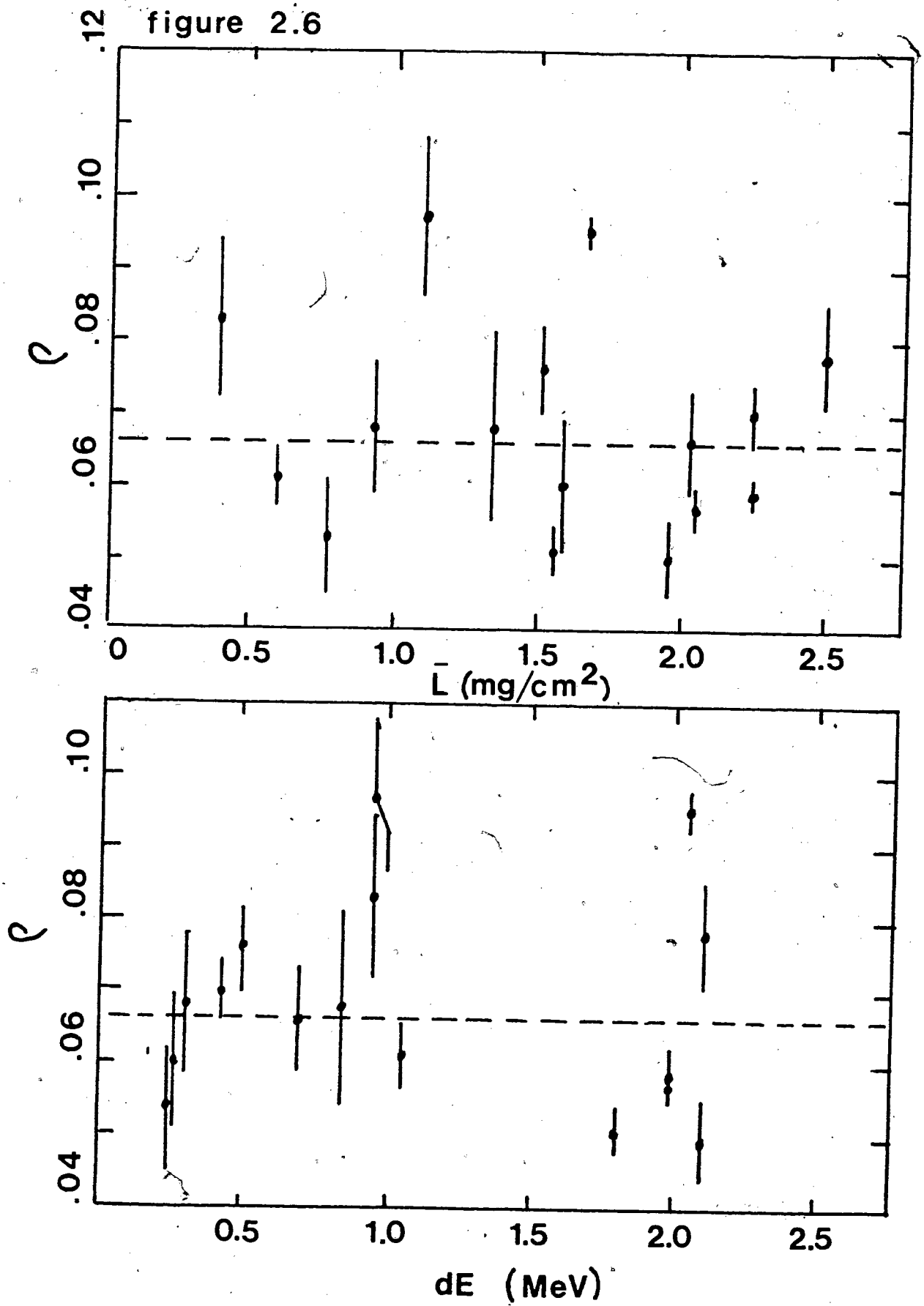
.12
.10
.08
.06
.04
ρ
0
0.5
1.0
1.5
2.0
2.5
L (mg/cm²)
.10
.08
.06
.04
ρ
0.5
1.0
1.5
2.0
2.5
dE (MeV)

dence of the width parameter on the total track length of the penetrating ions is observed (Fig.2.6). It would also be expected that T^2 would decrease somewhat with increasing track length. From Fig. 2.7 it can be seen that such an effect can also not be observed in this experiment. From both figures 2.6 and 2.7 it appears that average values for ρ and T^2 of $0.066 \pm .011$ and $0.062 \pm .017$ mg/cm^2 are good averages for the shape parameters for all ion masses and energies, at least to the extent of the accuracy in the present experiment.

All track length distributions, including those with poorer statistical precision were refitted with these fixed values for the shape parameters. The solid lines in figure 2.5 give an indication of the quality of these fits. The most probable track lengths derived from the fitted histograms are plotted in figure 2.8 as a function of the corresponding energies for all ion masses studied. The error bars represent the uncertainties due to the statistical precision of the fitted track length distributions only.

2.4 Comparison of track length data with theoretical stopping Models.

Before any comparison is made with theoretical models for the stopping process of heavy ions in matter, it should be pointed out that using these models one usually calculates the energy loss of the ion per unit path length as a function of the energy

figure 2.7

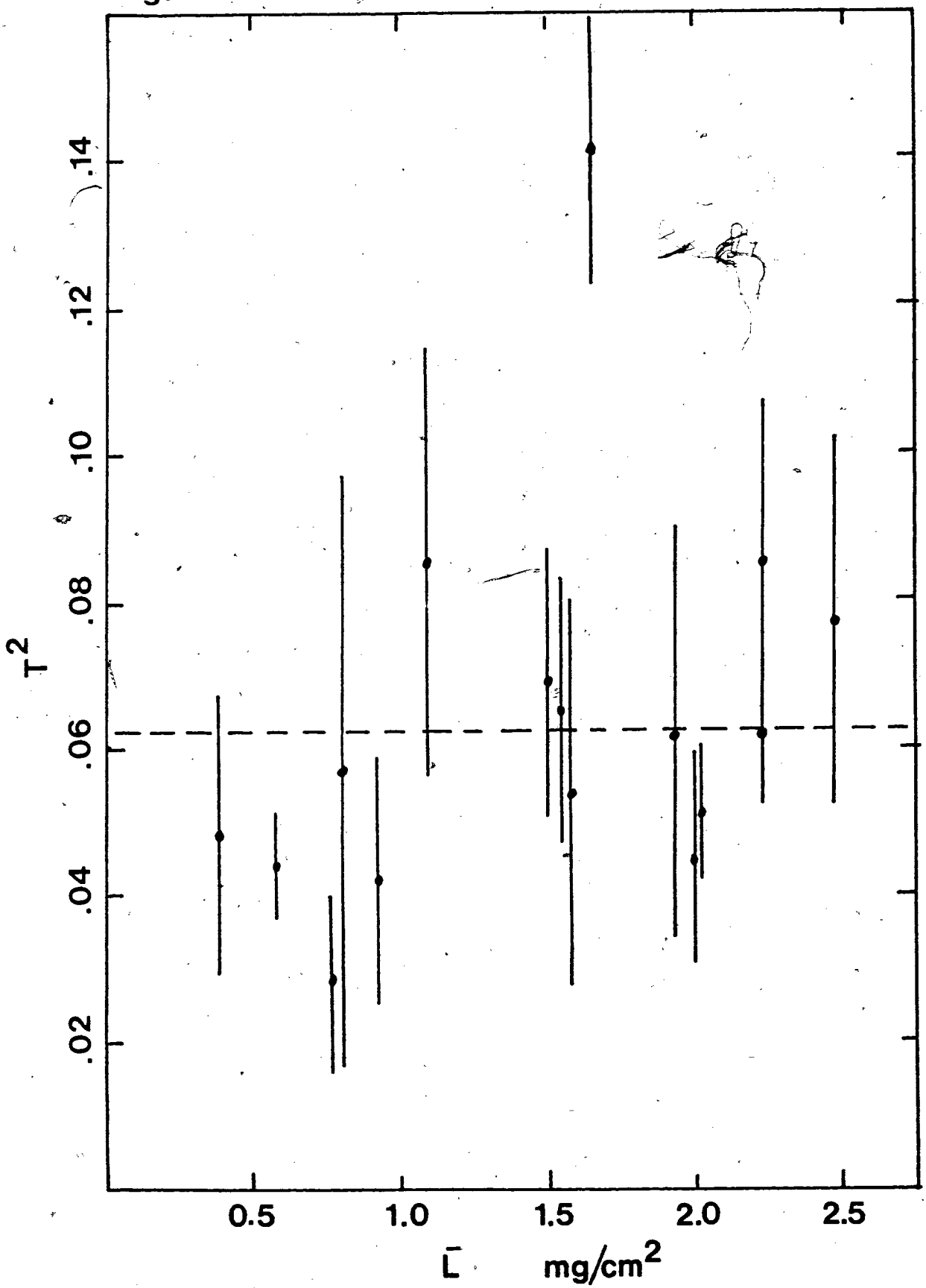

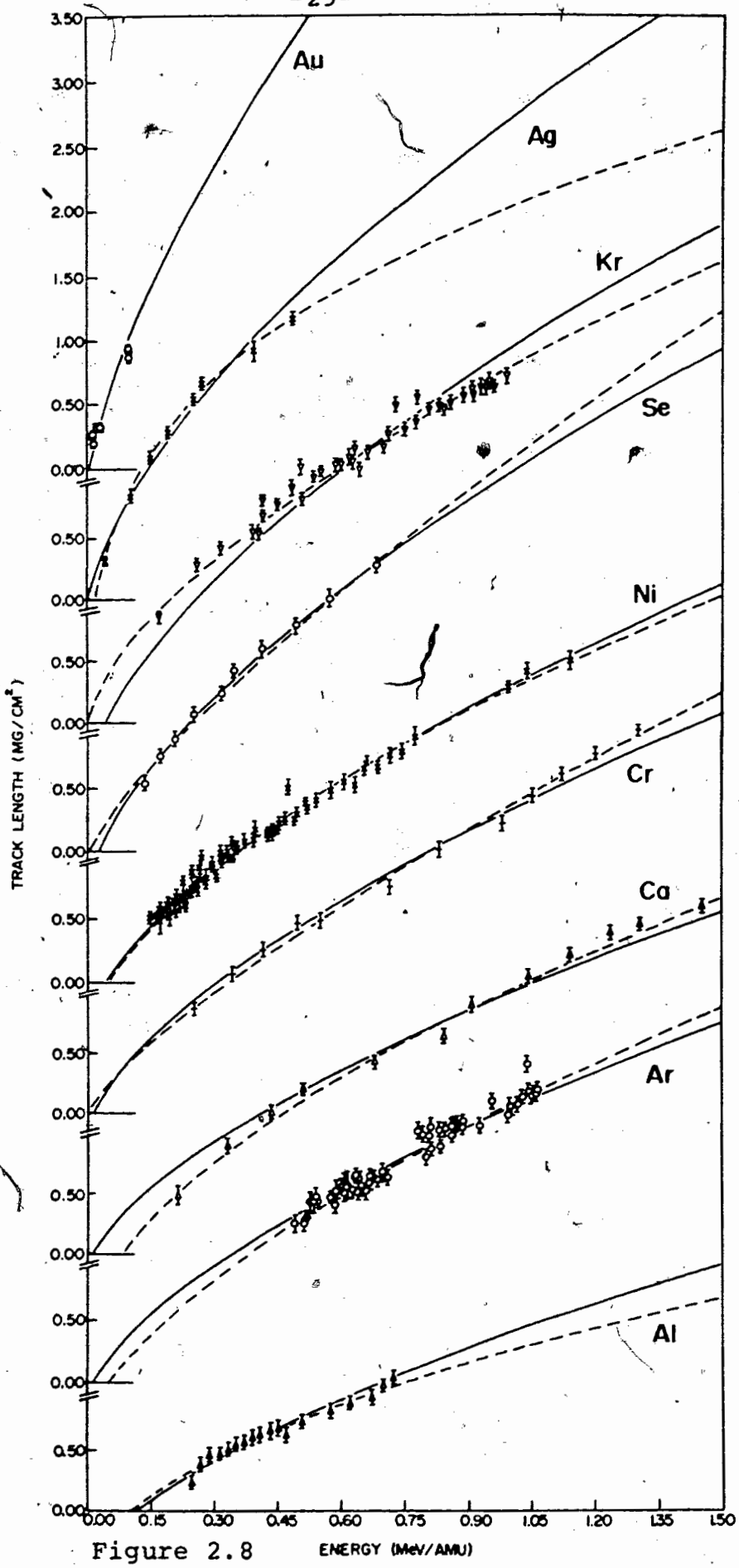
Au
Ag
Kr
Se
Ni
Cr
Ca
Ar
Al
TRACK LENGTH (MG/CM²)
ENERGY (MeV/AMU)
3.50
3.00
2.50
2.00
1.50
1.00
0.50
0.00
0.15
0.30
0.45
0.60
0.75
0.90
1.05
1.20
1.35
1.50

Figure 2.8

of the ion. Integration over energy will yield the range of the ion, and to a good approximation the mean range $\bar{R}$ is related to the track length by:

$$\bar{R} = L + \Delta L_s + \Delta L_t \qquad (2.7)$$

where ΔL_s is the sum of the two correction factors in equation 2.1 and ΔL_t, which we shall call the "terminal track length deficiency", is that part of the mean range $\bar{R}$, for which the ion does not lose sufficient energy per unit path length to leave a permanent damage trail. As was shown in Section 2.2.2 ΔL_s is usually negligible while it is to be expected that ΔL_t will depend on the mass of the ion, since the energy loss per unit path length is also mass dependent.

In order to compare theoretical estimates of $\bar{R}$ with track length data, ΔL_t values can be either estimated independently or, they could be extracted from the experimental data. Independent estimates of ΔL_t would involve establishing the critical energy loss rate of incident ions, and the use of a stopping model to calculate the residual range of the incident ions after they have slowed down to velocities where the critical energy loss rate is no longer exceeded. Extraction of ΔL_t values from the experimental data would involve the extrapolation of the track length data to zero energy. Inspection of the data in figure 2.8 reveals that such an extrapolation would be quite arbitrary without more

data at even lower energy values, or without any knowledge of the functional form of the track length versus energy variation. Either method of determining ΔL_t values, therefore, already relies on an a-priori knowledge of the interaction of the incident ions with the stopping medium, rendering any comparison of theoretical estimates of $\bar{R}$ with $L+\Delta L_t$ not very meaningful. However the objective of the calibration experiments was not so much to check theoretical stopping models, but to be able to determine the track length of any fission fragment in mica. The comparison with theoretical stopping models of the variation of the track length as a function of energy can be used to this aim.

The model which has been sucessful in describing the stopping of heavy ions at energy values embracing those of fission fragments has been formulated by Lindhard, Scharff and Schiøtt (Lin 63) (hereafter refered to as LSS). The functional form of the relationship of track length to energy can be derived from their model. The LSS theory described the stopping process of heavy ions in a medium in terms of a competition between two distinct modes of interaction between the penetrating ion and the stopping medium. The first mode (electronic stopping) is the interaction of the ion with the electrons of the stopping medium. The second mode (nuclear stopping) occurs when the ion undergoes elastic collisions with the atoms of the medium. The second mode will be pre-

dominant at low ion velocities, while the first will be predominant at higher velocities. In Fig. 2.9 the relative importance of nuclear stopping is illustrated for the case of a Kr ion slowing down in a mica medium. Shown is the nuclear stopping power at a given energy relative to the integrated nuclear stopping power (total nuclear stopping power of an ion slowing down to rest from an infinite velocity). The curve was generated by interpolation of the graphical representation of the nuclear stopping as a function of an energy parameter and a parameter which describes the target-ion system in terms of their mass and charge numbers (Lin 63). Also indicated in figure 2.9, by the dotted arrow, is the energy below which no permanent damage trail can be formed (see above), assuming the critical energy loss rate for mica is 10 MeV/(mg/cm^2). It is clear from this figure that for energy values over which a permanent damage trail is created, relatively little of the total nuclear stopping occurs, and since electronic stopping contributes more than nuclear to the overall stopping process in this energy range the nuclear stopping is of negligible importance. The observed track length may, therefore, presumably be interpreted in terms of electronic stopping alone.

The energy loss due to electronic stopping is given by (Lin 63):

$$\left(\frac{dE}{dX}\right)_{elec} = 8\xi_e N e^2 a_o \frac{Z_1 Z_2}{(Z_1^{2/3} + Z_2^{2/3})^{3/2}} \frac{V}{V_o} \qquad 2.8$$

figure 2.9

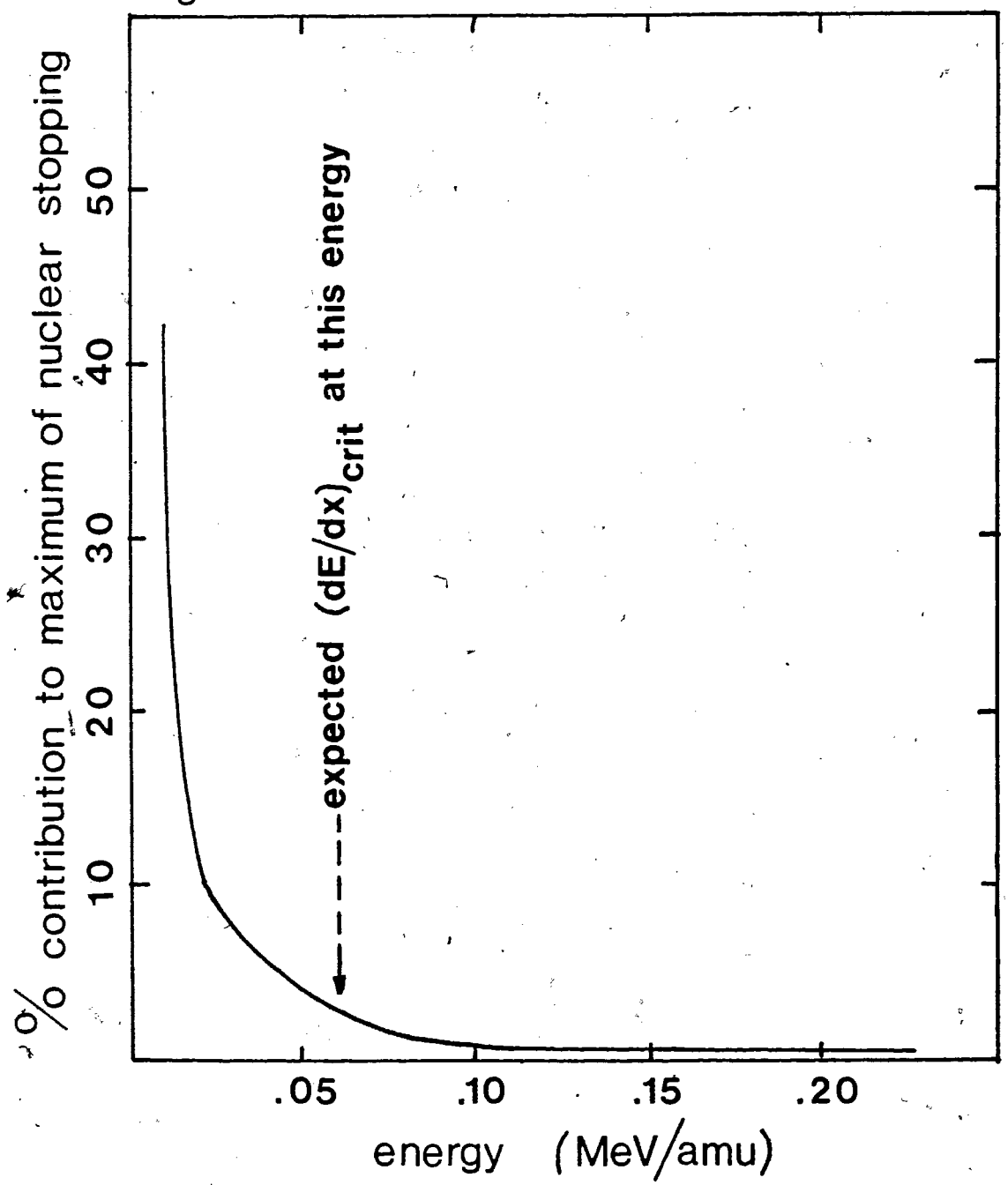
% contribution to maximum of nuclear stopping
10
20
30
40
50
expected (dE/dx)crit at this energy
.05
.10
.15
.20
energy (MeV/amu)

where N is the number of scattering centres per unit volume, a_o the radius of the first Bohr orbit of hydrogen, v_o is the velocity of the electron in that orbit, v is the ionic velocity, e is the electronic charge, while ξ_e has been given as $Z_1^{1/6}$ (Lin 63). The subscripts 1 and 2 denote the penetrating ion and the stopping medium atoms respectively. The mass and charge of the stopping medium atoms is usually taken as the weighted average for the various kinds of atoms present. In the case of muscovite mica, $KAl_2(Si_3AlO_{10})(OH,F)_2$, the uncertainty in the relative number of hydroxy and fluoride groups present, complicates such a procedure. Also, the inclusion of the contribution from the proton stopping process is questionable (Sau 65, Par 63). As a nominal average the values of 20 and 10 were chosen to represent the mass and charge number of the mica stopping medium.

The track length L is calculated through equations 2.7 and 2.8:

$$L = \frac{2v_o A_1 (Z_1^{2/3} + Z_2^{2/3})^{3/2}}{11.31N\,\xi_e\,\pi e^2 a_o Z_1 Z_2} \left(\frac{E}{A_1}\right)^{\frac{1}{2}} - \Delta L_t - \Delta L_s \qquad (2.9)$$

The functional form of the relationship between track length and energy can, therefore, be represented by:

$$L = bE'^{c} - \Delta L \qquad (2.10)$$

where E' is the energy of the penetrating ion in MeV/amu, and $\Delta L = \Delta L_t + \Delta L_s = \Delta L_t$, since ΔL_s is negligible. The exponent c is expected, from equation 2.9, to have a value of 0.5, and from the same equation, the constant b should vary with the mass and charge of the penetrating ion as:

$$b = 0.0552 \frac{A_1}{Z_1^{7/6}} (Z_1^{2/3} + 4.64)^{3/2} \qquad 2.11$$

In order to check this functional form the data of figure 2.8 (with the exception of those for gold ions for which the energy region covered was insufficient) were fitted to equation 2.10. All parameters were left free, and the results are shown in table II.3.

The standard deviations from the mean are large for all parameters, so that a direct comparison with the theoretical b and c values is difficult to make. The c values, with the exception of that for silver, all fall within the range of 0.64±0.15. The low value for silver could be due to the limited energy interval over which track length data are available, and a value of 0,64 for the exponent in this case also gives a reasonable fit to the data. Although the theoretical (Lin 63) value of 0.5 for the exponent does fall within the spread quoted for the mean experimental value, there has been previous evidence (Ale 60) that a value of 2/3 often gives a better fit to experimental data.

Table II.3 The fitted parameters ΔL, b and c of the relationship $L = bE'^{c} - \Delta L$ and their standard deviation from the mean, where E' is in MeV/amu and L in mg/cm^2 (based on a density for mica of 2.91 gm/cm^3).

Incident ion	ΔL	b	c
Al	0.62±0.25	1.88±0.62	0.50±0.33
Ar	0.62±1.01	2.56±1.03	0.64±0.34
Ca	0.65±0.04	2.70±0.35	0.57±0.09
Cr	-0.29±0.20	1.30±0.31	0.77±0.14
Ni	0.62±0.11	2.82±0.21	0.55±0.07
Se	0.96±0.21	3.02±0.15	0.79±0.15
Kr	0.93±0.34	2.74±0.45	0.63±0.16
Ag	1.42±0.26	5.03±0.66	0.26±0.06

By fitting the exponent to the mean value of 0.64 the remaining two parameters b and L can be re-determined with greater accuracy. In table II.4 the result of this is shown in columns 2 and 3, The standard deviations from the mean are much smaller, but they do not, of course, reflect the uncertainty associated with choosing a mean value for exponent c. In column 4 of the same table the theoretical estimate of b

values, as calculated using equation 2.11 are shown. They follow the trend of the experimental data very well, but are systematically higher, as can also be seen from Fig. 2.10 After multiplying with a constant factor of 0.769, reasonable agreement is obtained with the experimental data.

As stated above, the aim of this procedure was to establish shape parameters for the functional form of equation 2.10, describing the track length-energy relationships. In order to generalize these parameters for all possible incident ions, the b parameter was fixed at 0.769 times the theoretical value. The discrepancy from the theoretical value is not too disturbing in view of the difficulty in choosing the proper average mass and charge numbers for the mica stopping medium. Furthermore the parameter ξ_e was chosen to be $Z_1^{1/6}$, although various other values have been used (Ara 65, Kak 69, Hon 71) with equal or better results in respect to other experimental data.

With both shape parameters b and c fixed at the above values the data were fitted once more with ΔL as the only variable. The results of this are also shown in Table II.4 as well as Figure 2.11. From these values, the critical energy (below which no permanent damage trail is produced) can be deduced for each of the incident ions. These values are given in the last column of Table II.4 and in figure 2.12. The solid curves in this figure represent lines of constant dE/dX as calculated

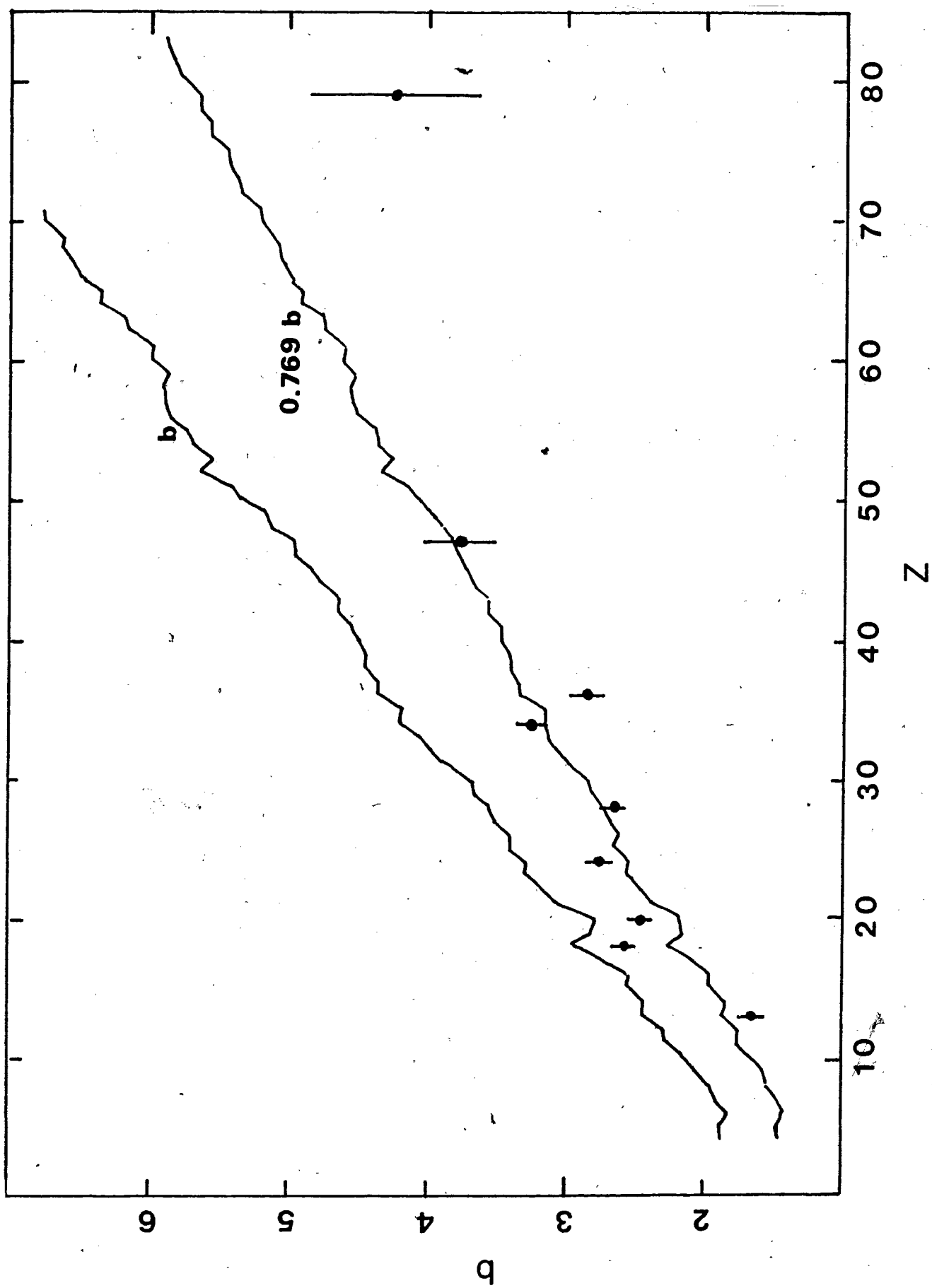

figure 2.10

Table II.4 The fitted parameters b_c and ΔL_c of the relationship $L = bE'^{c} - \Delta L$ with c fixed for all ions at 0.64 as well as b_{theor} values calculated using equation 2.11. The last two columns give ΔL_f and E'_{crit} values obtained by fitting to the relationship $L = 0.769\, b_{theor} E'^{0.64} - \Delta L_t$ while E'_{crit} is defined by:

$$E'^{0.64}_{crit} = \frac{\Delta L_f}{0.769 b_{theor}}$$

Incident Ion	c=0.64		b_{th}	b_f= $0.769 b_{th}$	c=0.64, b=b_f	
	b_c	ΔL_c			ΔL_f	E_{crit} (MeV/amu)
Al	1.64±0.07	0.345±0.003	2.24	1.86	0.48±0.005	0.117±0.001
Ar	2.57±0.07	0.388±0.004	2.96	2.28	0.15±0.004	0.014±0.001
Ca	2.46±0.06	0.419±0.007	2.79	2.15	0.13±0.011	0.012±0.001
Cr	2.73±0.08	0.334±0.009	3.29	2.53	0.17±0.010	0.014±0.001
Ni	2.62±0.05	0.356±0.004	3.43	2.64	0.37±0.004	0.045±0.001
Se	3.25±0.06	0.325±0.004	4.19	3.23	0.31±0.005	0.026±0.001
Kr	2.82±0.10	0.057±0.009	4.33	3.33	0.44±0.010	0.042±0.001
Ag	3.74±0.24	0.084±0.016	4.95	3.81	0.11±0.020	0.004±0.001
Au	4.26±0.58	0.104±0.021	7.35	5.66	0.29±0.040	0.009±0.001

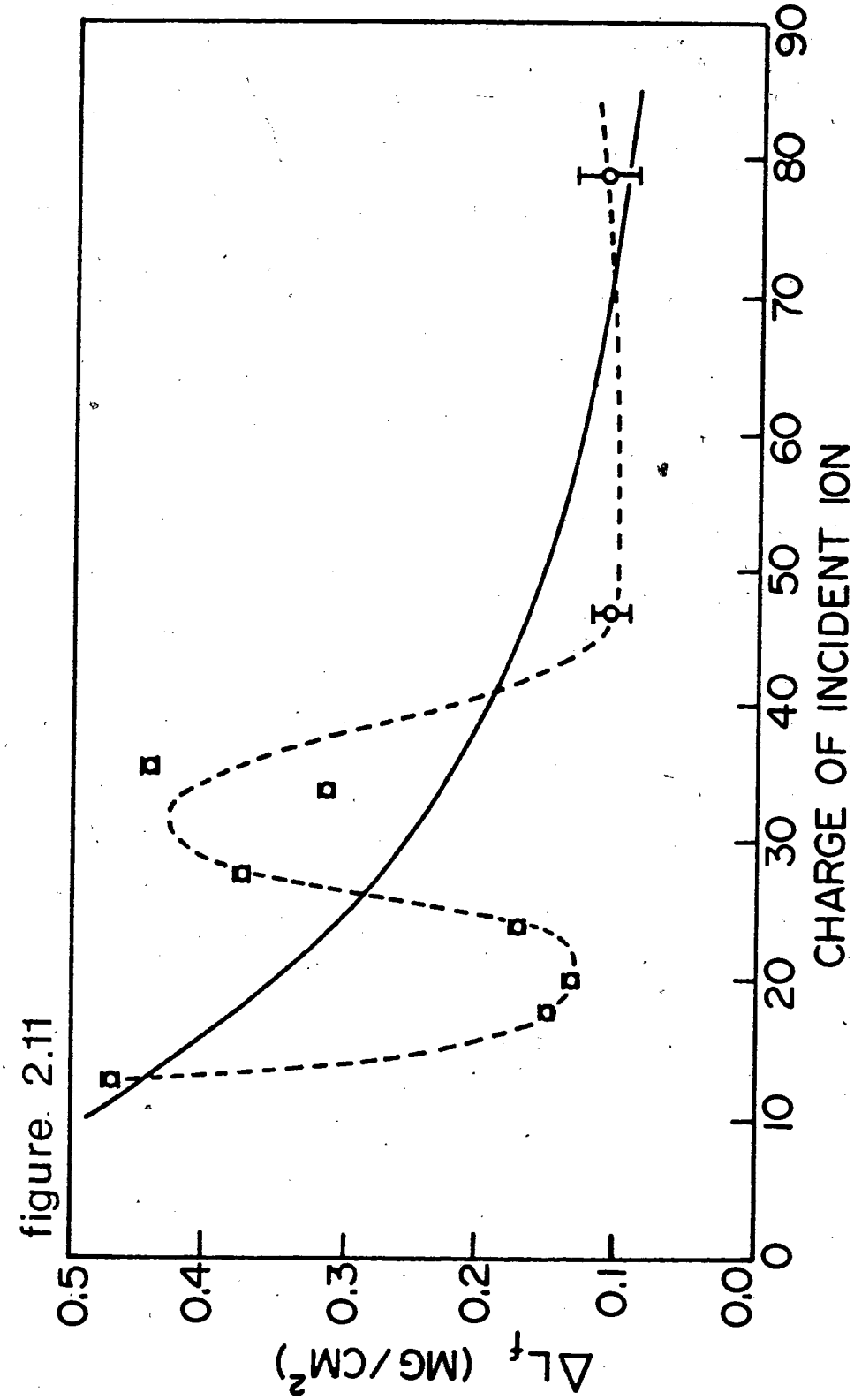
0.5
0.4
0.3
0.2
0.1
0.0
ΔL_f (MG/CM^2)
0
10
20
30
40
50
60
70
80
90
CHARGE OF INCIDENT ION

figure 2.11

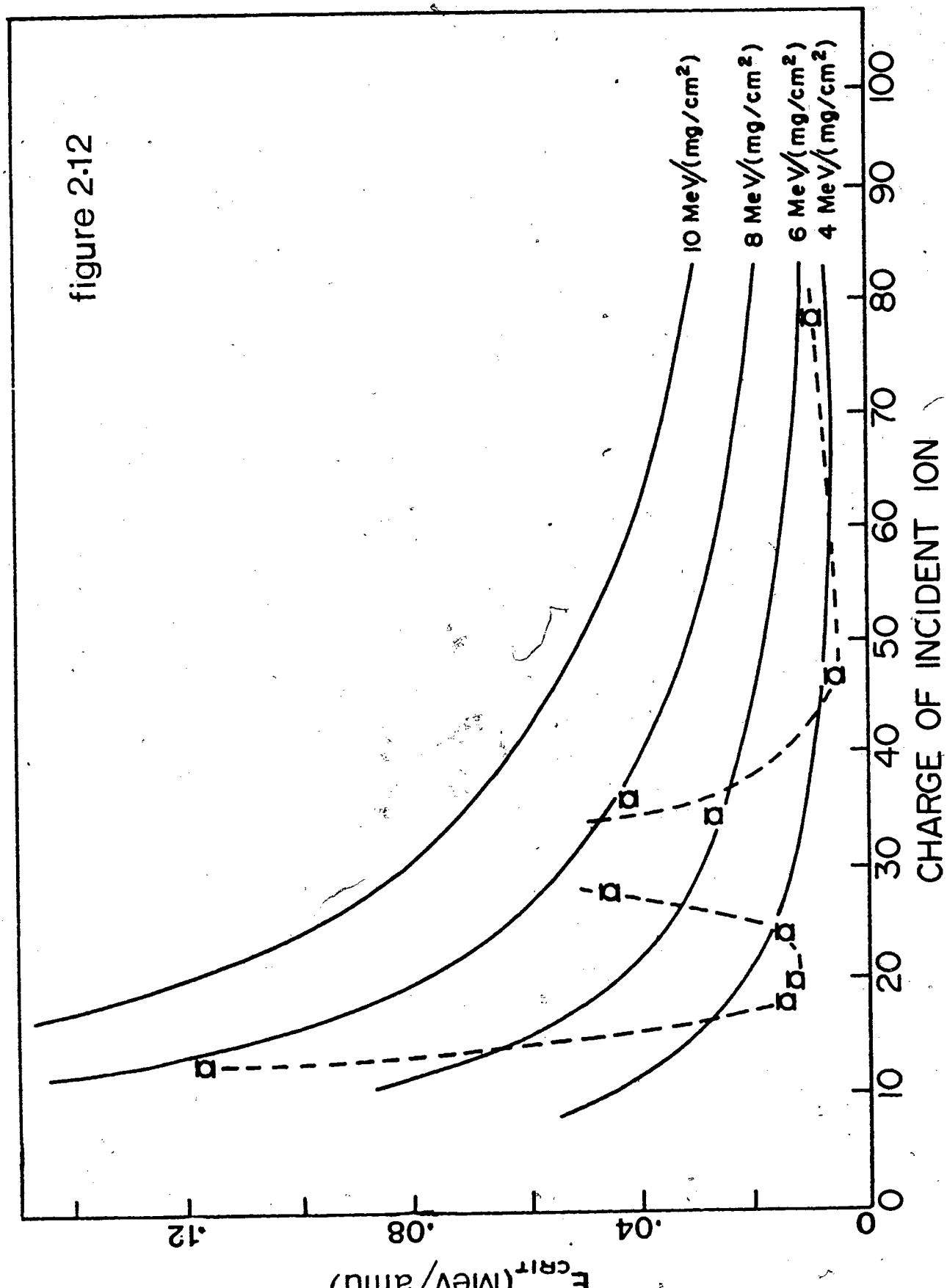
10 MeV/(mg/cm²)
8 MeV/(mg/cm²)
6 MeV/(mg/cm²)
4 MeV/(mg/cm²)
CHARGE OF INCIDENT ION
0
10
20
30
40
50
60
70
80
90
100
E'crit (MeV/amu)
0
.04
.08
.12

figure 2.12

using the LSS theory. The data do not show the monotonic variation with the charge of the incident ion which would have been expected if two assumptions were correct: 1) that there is indeed a unique critical amount of energy loss required to produce an etchable track and 2) that the LSS theory predicts the correct variation of the energy loss as a function of the mass, charge and energy of the incident ion. Since the ΔL values represent the residual range of the incident ions at very low energies, the second assumption is probably not valid. Ormrod and Duckworth (Orm 63) as well as other investigators (Fas 66, Dar 65, Tep 62) have shown that at such low velocities the electronic stopping cross section, measured for a series of ions, oscillates around the values predicted by the LSS theory. The data as given in Figure 2.12 are consistent with this. Since the electronic stopping cross section is directly proportional to dE/dX, the velocities at which a constant value of dE/dX is suffered should also oscillate around the calculated values, but with maxima in the place of minima and vice versa. This would then suggest a low stopping power for ions near $Z = 13$ and a high stopping power for ions near $Z = 20$ which is in excellent agreement with the results of Ormrod and Duckworth (Orm 63). However, it should be pointed out that by fixing the shape parameters b and c, we have artificially removed the uncertainty in the ΔL values, so that no absolute conclusions can be drawn from the above.

This point is further exposed in figure 2.8 where the solid lines represent the fitted curves with the shape parameters b and c fixed, while the dotted line represents the initial fits with all parameters treated as independent variables. By fixing the shape parameters, we have nevertheless created an easily used tool for the interpolation of track length-mass-energy data to mass values for other incident ions. Using equations 2.10 and 2.11, the track length L of any incident ion of mass A and charge Z can be expressed to a good approximation as

$$L(Z,A,E') = - \Delta L(Z) + 0.0434 \frac{A}{Z^{7/6}} (Z^{2/3} + 4.64)^{3/2} E'^{0.64} \quad (2.12)$$

where L is in mg/cm^2 and E' is the energy of the incident ion in MeV/amu. The $\Delta L(Z)$ values are obtained from figure 2.11, where the dotted line represents a graphical interpolation of the available data.

Chapter 3 Track length of fission fragments in mica.

3.1 Experimental techniques.

Fission was induced by alpha particles with energies ranging from 80 to 167 MeV, interacting with Mo, Ag, In, Te and Au nuclei. The targets were prepared with their purity being a major concern. Fission cross-sections of the lighter nuclei are in the microbarn region, whereas possible heavier nuclei contaminants may have fission cross-sections in the range of one to two barns.

Target preparation was accomplished by fractional distillation starting with material of 99.999% to 99.9999% purity. Sources for these materials have been given elsewhere (Pat 71). In the case of Ag and Au targets, the metal layer was deposited on a clean glass surface, and floated off on distilled water. From there the targets were transferred to copper mounting rings with a nominal diameter of one inch. All other target materials were evaporated onto thin films on VYNS (Pat 55), which were then transferred together with the target material to the copper mounting rings. Some of the Au targets as well as the Mo and In targets were prepared by L. Lecerf and J. Péter at Orsay, France. Table III.1 lists all targets by their thickness and origin and gives the energy of the alpha particles used in the subsequent irradiations, as well as the integrated beam intensities, measured using a Faraday cup.

Table III.1 Targets used in the fission experiments.

target material	thickness (including VYNS if present) ($\mu g/cm^2$)	origin of target	energy of α-particles used (MeV)	integrated beam intensity (coulomb)
Au	140	ORSAY	167[a]	3.5×10^{-6}
	349	SFU	120[b]	2.25×10^{-4}
	355	SFU	100[b]	4.26×10^{-4}
	349	SFU	80[b]	1.08×10^{-3}
Te	442 + 70 VYNS	SFU	80[b]	3.83×10^{-3}
In	175 + 15 VYNS	ORSAY	167[a]	4.7×10^{-4}
Ag	513	SFU	80[b]	5.12×10^{-2}
Mo	360 + 70 VYNS	ORSAY	167[a]	4.4×10^{-4}

a ORSAY synchrocyclotron

b Texas A & M variable energy cyclotron

As indicated in the fourth column of Table III.1, the irradiations took place at two different institutions; the 167 MeV alpha bombardments with the synchrocyclotron at l'Institut de Physique Nucléaire, Orsay, France and all other bombardments were performed using the variable energy cyclotron of the Texas A & M University, College Station, Texas. A different scattering chamber was used at each locale. At Orsay the same chamber used for the calibration experiments described in Chapter 2, was employed, while at Texas A & M a chamber was used, courtesy of Dr. J.B. Natowitz, which had a diameter of 110mm, and in

which the mica surface was at 45° with respect to the beam direction from which the fission fragments were incident. Mica as well as glass detectors, were mounted for each irradiation. The glass detectors were either left at Orsay or, in the case of the TAMVEC (Texas A & M Variable Energy Cyclotron) bombardments, were sent to Orsay for development and scanning. The mica detectors were etched at Simon Fraser University and scanned for tracks similarly to the technique described in Chapter 2. In the case of the mica detectors from the TAMVEC experiments, not only was the projected length of each track recorded, but also the position of that track on the mica surface. The large detector areas scanned in these experiments, following from the low track density, no longer justified the use of an average angle of incidence for each of the fission fragments measured within a given angular interval, as had been the case in the calibration experiments described earlier.

3.2 Conversion of the raw experimental data to track length distributions.

As long as the detector surface, that is scanned for fission tracks, lies in the same horizontal plane as the beam of incident particles, the angle of emission of the fission fragments is simply determined by the angle at which that particular piece of mica surface is oriented with respect to the beam direction. If the detector surface extends well beyond the

plane of the beam, this angle can be determined from the relative position of the track with respect to a reference point. An added complication, however, is the fact that the conical mica surface from the scattering chamber is flattened out for scanning under the microscope. This necessitates the conversion of the coordinates from the two dimensional plane of the mica surface to the coordinate system of the scattering chamber. In appendix 2 the transformation operators to get from one to the other coordinate system are given.

To illustrate the importance of this procedure of angle determination, figure 3.1 shows a typical detector surface from the TAMVEC experiments. Superimposed are lines indicating a given angle of emission of the fission fragments in steps of ten degrees. The approximation that can be made if the height of the detector surface is much smaller than the diameter of the scattering chamber is indicated by the dotted lines in the same figure.

The raw experimental track length data were all treated with either this approximation (Orsay data) or the above calculations (TAMVEC data) and then grouped by angle of emission, so as to yield distributions of track length each for a known interval of emission angles.

Since the mica surface was slanted in the scattering chamber, unit areas in some locations on the mica surface represented

figure 3.1

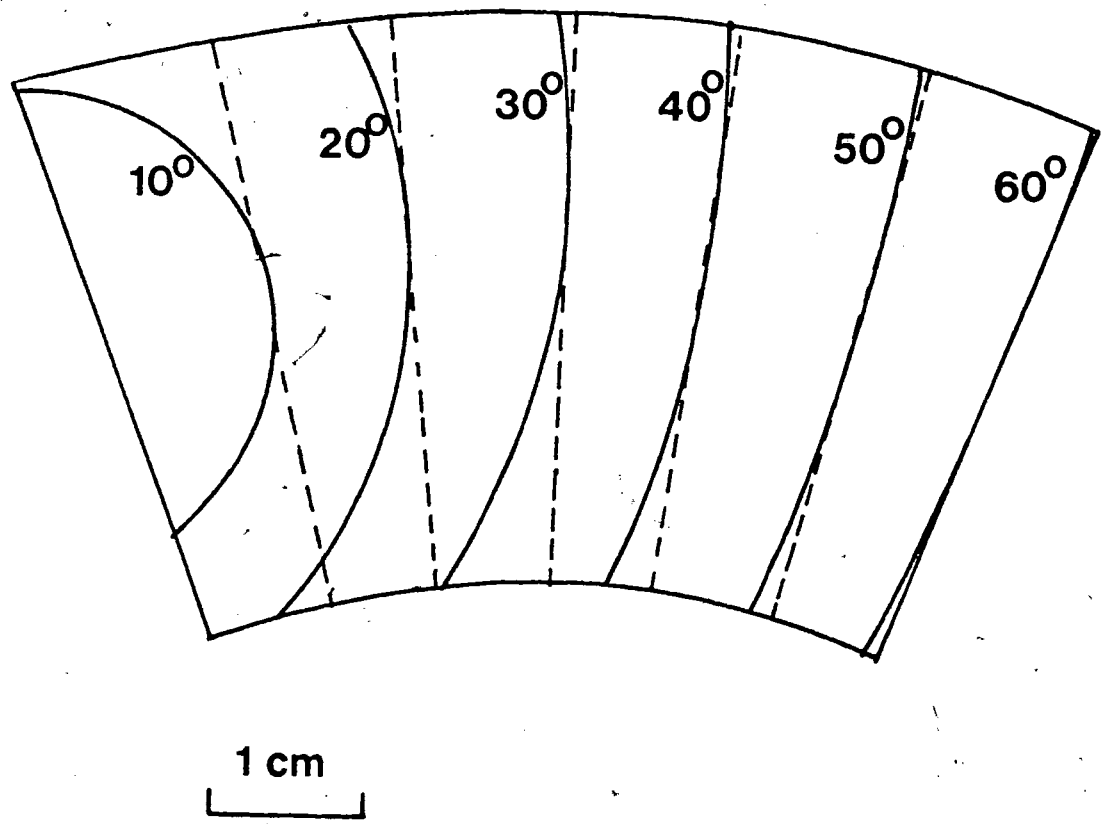

a different solid angle (into which the detected number of fragments had been emitted) than at other locations. This solid angle difference was corrected for (via the target mica distance) when converting track densities to differential cross-sections.

3.3 Data from the 167-MeV alpha particle induced fission of Mo, In and Au.

All 167-MeV alpha particle bombardments took place at the Orsay synchocyclotron, and were supervised by J. Péter and L. Lecerf.

3.3.1 167-MeV alpha particles on gold.

The distributions of track length, for five degree intervals of laboratory angle of observation, are shown in figure 3.2. In Table III.2 the data are summarized. For some angular intervals the average peak position is not shown. For these intervals only a count was made of the total number of tracks. Track densities were obtained by measuring the areas of the mica surface that was scanned for each angle of observation. Calibrated dial type stage micrometers were used for this purpose. Track densities were low ($\simeq$20 tracks/mm^2) from a scanner's point of view, but sufficient data could be collected so as to obtain a statistically significant track length distribution for each five degree interval. Total area scanned in this experiment was 212 mm^2, in which approximately 5000 tracks were counted,

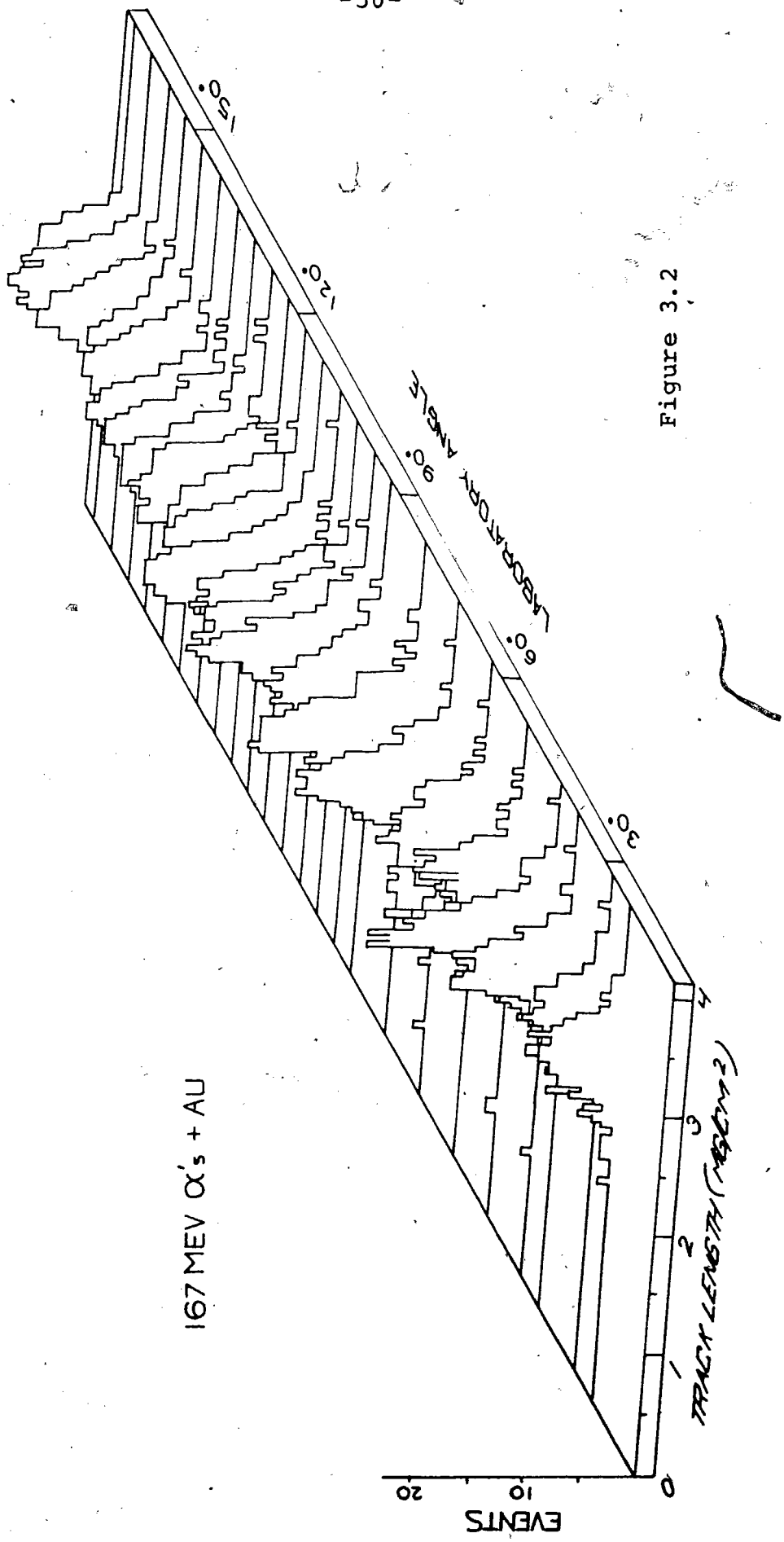
167 MEV α's + AU
EVENTS
0
10
20
TRACK LENGTH (MICRONS²)
0
1
2
3
4
LABORATORY ANGLE
30°
60°
90°
120°
150°

Figure 3.2

Table III.2 167-MeV alpha particles on gold.

Summary of experimental data.

laboratory angular interval scanned (degrees)	area scanned (mm^2)	number of tracks	average peak position (mg/cm^2)	normalized* track density (tr/mm^2)
15-20	6.00	279	n/a +	43.5 ± 2.6
20-25	2.37	101	2.87	40.5 ± 4.0
25-30	6.00	278	n/a +	41.1 ± 2.5
25-30	2.37	90	2.98	25.0 ± 3.7
30-35	6.00	233	n/a +	37.4 ± 2.4
35-40	3.56	125	2.79	33.3 ± 3.0
40-45	4.74	183	2.87	35.6 ± 2.6
45-50	6.00	172	n/a +	25.4 ± 1.9
50-55	4.74	116	2.84	21.8 ± 2.0
55-60	6.00	136	n/a +	20.5 ± 1.8
60-65	4.74	130	2.69	25.3 ± 2.2
65-70	6.00	123	n/a +	18.8 ± 1.7
70-75	9.63	169	2.59	16.4 ± 1.3
75-80	10.38	203	2.51	18.0 ± 1.3
80-85	10.85	197	2.51	16.7 ± 1.2
85-90	9.88	177	n/a +	16.4 ± 1.2
90-95	8.37	127	2.42	14.9 ± 1.3
95-100	9.73	170	2.49	15.6 ± 1.2
100-105	10.05	163	2.39	15.4 ± 1.2
105-110	9.64	141	2.37	13.8 ± 1.2
110-115	11.47	213	2.33	16.5 ± 1.1
115-120	10.69	177	2.29	15.0 ± 1.1
120-125	7.27	136	2.32	16.7 ± 1.4
125-130	8.53	162	2.30	16.9 ± 1.3
130-135	6.88	147	2.27	19.4 ± 1.6
135-140	7.13	148	2.26	18.8 ± 1.5
140-145	4.46	116	2.24	21.6 ± 2.0
145-150	4.70	128	2.25	25.7 ± 2.3
150-155	3.48	106	2.26	27.0 ± 2.6
155-160	3.65	138	2.23	33.3 ± 2.8
160-165	3.56	138	2.26	34.4 ± 2.9
165-170	2.96	104	2.22	31.4 ± 3.1

* normalized to a common track-target distance of 55 mm.

+ for these data only the number of tracks was counted

about 4000 of which were also measured for track length.

3.3.2 167-MeV alpha particles on indium.

The track density in this experiment was extremely poor (≈5 tracks/mm^2). Consequently, even scanning practically all of the available detector area (about 25 mm^2 per five degree interval) insufficient data are available to construct track length distributions with more than minimal statistical accuracy. In figure 3.3 track length distributions are shown for seven angles of observation. At angles less than 110 degrees a large number of small pits and tracks are present. These small tracks are presumably due to the scattering of target nuclei by the alpha particles, as well as to the scattering or interaction of the alpha particles with some of the heavier nuclei in the surface layer of the detector material.

In order to distinguish the tracks due to fission and the above scattering effects, quite arbitrarily only those tracks were counted with a track length greater than the value indicated by the dotted arrows in fig. 3.2. For laboratory angles of observation of more than 110^o, all tracks were taken into account. Table III.3 summarizes the data. When no average peak position is indicated, only the number of tracks were counted which satisfied the above mentioned fission track criteria. The concept of an average track length in this experiment has to be treated very cautiously in view of the poor statistical

figure 3.3

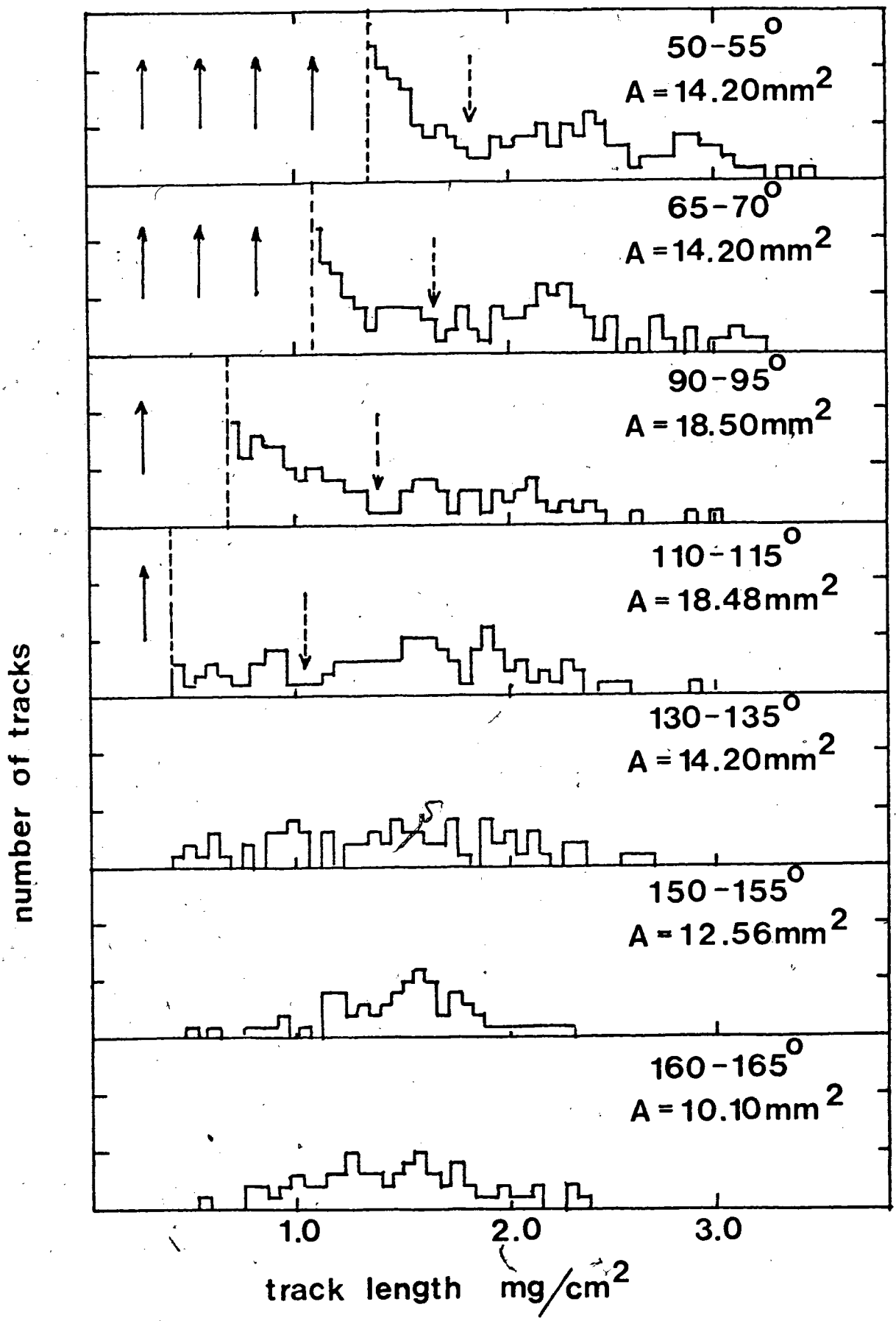
167 MeV alphas + In
50-55°
A = 14.20mm²
65-70°
A = 14.20mm²
90-95°
A = 18.50mm²
110-115°
A = 18.48mm²
130-135°
A = 14.20mm²
150-155°
A = 12.56mm²
160-165°
A = 10.10mm²
number of tracks
1.0
2.0
3.0
track length mg/cm²

Table III.3 167-MeV alpha particles on indium. Summary of experimental data.

laboratory angular interval scanned	area scanned (mm^2)	number of tracks	average peak position mg/cm^2	track density tr/mm^2
45°-50°	8.82	60	-	6.80±.88
50°-55°	14.20	81	2.5	5.70±.63
55°-60°	14.28	67	-	4.69±.57
60°-65°	16.92	74	-	4.37±.51
65°-70°	14.02	67	2.2	4.78±.58
80°-85°	24.00	73	-	3.04±.36
85°-90°	16.00	45	-	2.81±.42
90°-95°	18.50	48	1.9	2.60±.37
90°-95°	16.00	48	-	3.00±.43
95°-100°	12.00	36	-	3.00±.50
100°-105°	12.00	47	-	3.92±.57
105°-110°	16.00	66	-	4.13±.51
110°-115°	18.48	76	1.8	4.11±.47
110°-115°	16.00	72	-	4.50±.53
115°-120°	16.00	57	-	3.56±.47
120°-125°	12.00	40	-	3.33±.53
125°-130°	9.60	46	-	4.79±.71
130°-135°	14.20	75	1.6	5.28±.61
130°-135°	12.00	70	-	5.83±.70
135°-140°	12.00	59	-	4.92±.64
140°-145°	12.00	68	-	5.67±.69
145°-150°	9.00	55	-	6.11±.82
150°-155°	12.56	65	1.6	5.17±.64
150°-155°	7.70	50	-	6.49±.92
155°-160°	14.40	105	-	7.29±.71
160°-165°	10.10	68	1.5	6.73±.82
160°-165°	14.40	114	-	7.92±.74
165°-170°	12.00	87	-	7.35±.78

accuracy of the distribution in figure 3.2.

3.3.3. 167-MeV alpha particles on molybdenum.

As in the case of the indium experiment, the track density was very poor (≈2 tracks/mm^2). The lighter mass of molybdenum as compared to indium also worsened the problem of differentiating fission fragment tracks from small tracks at forward angles of observation. Track length distributions, as measured at eight angles of observation, are shown in figure 3.4. Determination of an average track length from these data is not feasible. A distinct 'hump' in the track length distributions occurs at extreme backward angles of observation. Since instinctively, one would assume that the average track length in the case of the molybdenum bombardments will be shorter than that of the indium bombardments, it is tempting to assume that this hump represents the fission fragments from the molybdenum plus alpha system, while the tracks with larger lengths could be due to impurities in the target material. Such an analysis, however, will be left to Chapter 4. Table III.4 summarizes the data of each distribution, as well as the data obtained for angular intervals other than those indicated in figure 3.4. Only those tracks were taken into account which had a length greater than that indicated by the dotted arrows (figure 3.4).

figure 3.4

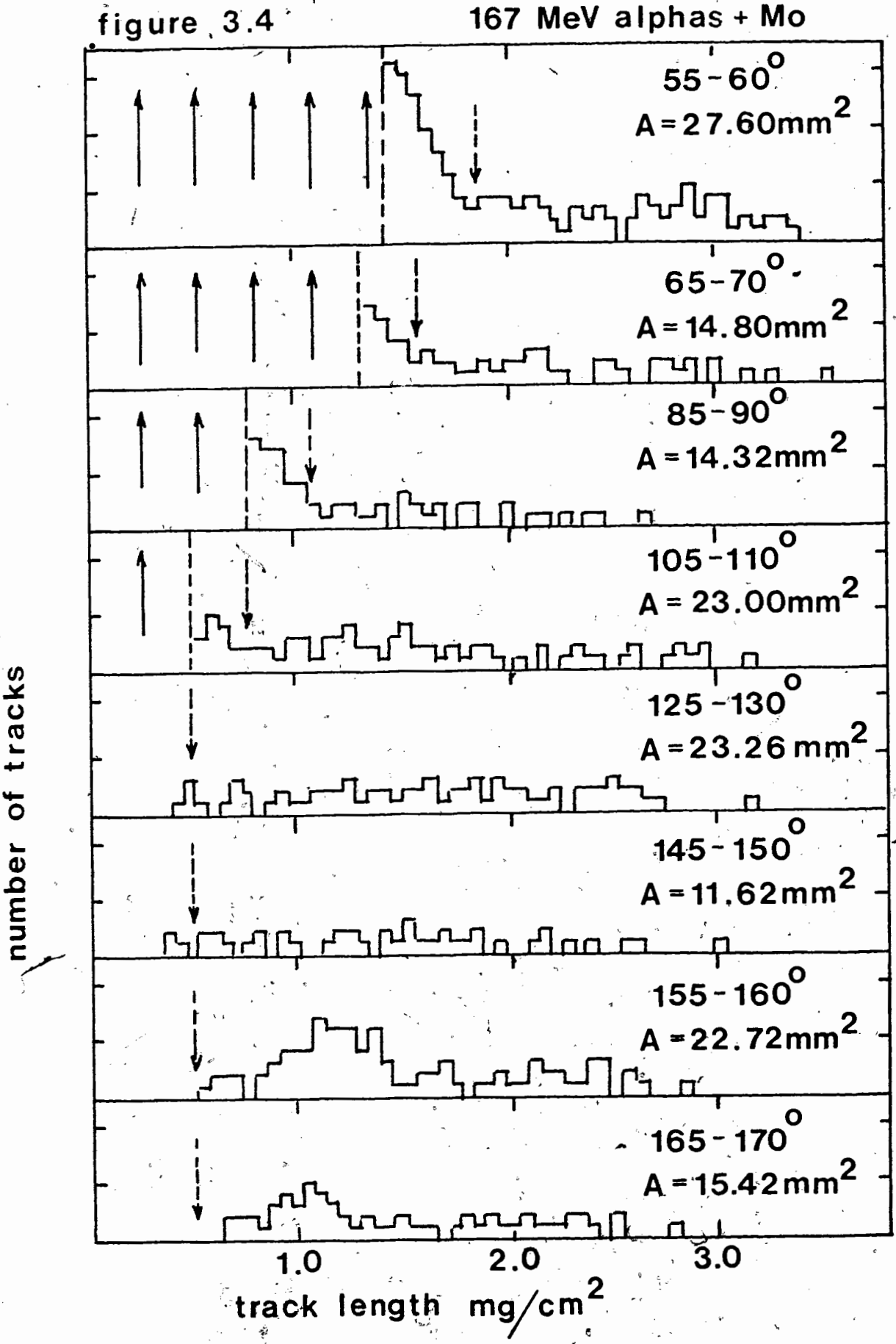
167 MeV alphas + Mo
55 - 60°
A = 27.60mm²
65 - 70°
A = 14.80mm²
85 - 90°
A = 14.32mm²
105 - 110°
A = 23.00mm²
125 - 130°
A = 23.26 mm²
145 - 150°
A = 11.62mm²
155 - 160°
A = 22.72mm²
165 - 170°
A = 15.42mm²
number of tracks
1.0
2.0
3.0
track length mg/cm²

Table III.4 167-MeV alpha particles on Molybdenum. Summary of experimental data.

laboratory angular interval scanned	area scanned (mm^2)	number of tracks	track density tr/mm^2
55°-60°	27.60	73	2.65±.31
60°-65°	18.22	44	2.41±.36
65°-70°	14.80	41	2.77±.43
75°-80°	20.00	36	1.80±.30
80°-85°	20.00	35	1.75±.30
85°-90°	14.32	31	2.17±.39
85°-90°	20.00	38	1.90±.31
90°-95°	12.00	20	1.67±.37
95°-100°	15.00	29	1.03±.36
100°-105°	20.00	36	1.80±.30
105°-110°	23.00	65	2.83±.35
105°-110°	20.00	52	2.60±.36
110°-115°	20.00	42	2.10±.32
115°-120°	15.00	32	2.13±.38
120°-125°	15.00	35	2.33±.39
125°-130°	23.26	69	2.97±.36
125°-130°	20.00	60	3.00±.39
130°-135°	20.00	53	2.65±.36
135°-140°	16.00	49	3.06±.44
140°-145°	15.00	43	2.87±.44
145°-150°	11.62	40	3.44±.54
145°-150°	12.00	40	3.33±.53
150°-155°	24.00	86	3.58±.39
155°-160°	22.72	97	4.27±.43
155°-160°	20.00	80	4.00±.45
160°-165°	24.00	103	4.29±.42
165°-170°	15.42	62	4.02±.51
165°-170°	15.00	54	3.60±.49

3.4 Data from the 80- to 120-MeV alpha-particle-induced fission of Ag, Te and Au.

The variable energy cyclotron of the Texas A & M University was used to obtain data on the alpha-particle-induced fission of gold at 80 , 100 and 120 MeV (120 MeV being the maximum attainable energy at this installation). Similar data would have been collected for the lighter target systems, but the poor counting rates obtained in the Orsay experiments with beam intensities in the order of 5×10^{-4} Coulomb indicated that excessive amounts of beam time would have been required. Instead an effort was made to obtain a larger number of fission events at one energy (80-MeV) by increasing the target thickness by a factor of $\simeq 3$ and the beam intensities by a factor of 10 to 100.

3.4.1 80-, 100- and 120-MeV alpha particles on Gold.

Track length distributions as a function of the laboratory angle of observation are shown in figures 3.5 and 3.6 for the fission fragments from the 80- and 100-MeV alpha particle bombardments. Track densities in all cases varied between 1000 and 7000 tracks per square millimeter. Consequentially the area scanned for each distribution was very small (0.02 to 0.08 mm^2), and the average angle of observation has a well defined value. For track densities greater than 3000 tracks/mm^2, a significant amount of overlapping of fragment tracks occurs. It becomes difficult, if not rather arbitrary, to assign track length values in such cases. Only for the 80 MeV alpha particle bombardment the track density was so high, that by omitting overlapping tracks, the track density was underestimated outside the statistical limits of the measurement. For this case a separate determination of the angular distribution was made by only counting the total number of tracks in a given area of the mica surface. Table III.5 lists the results of this procedure and summarizes the data derived from the track length distributions. Table III.6 gives the results of the 100-MeV alpha-particle-bombardments, while Table III.7 lists the angular distribution data obtained from the 120-MeV alpha-particle-bombardment. No track length distributions were measured in this case.

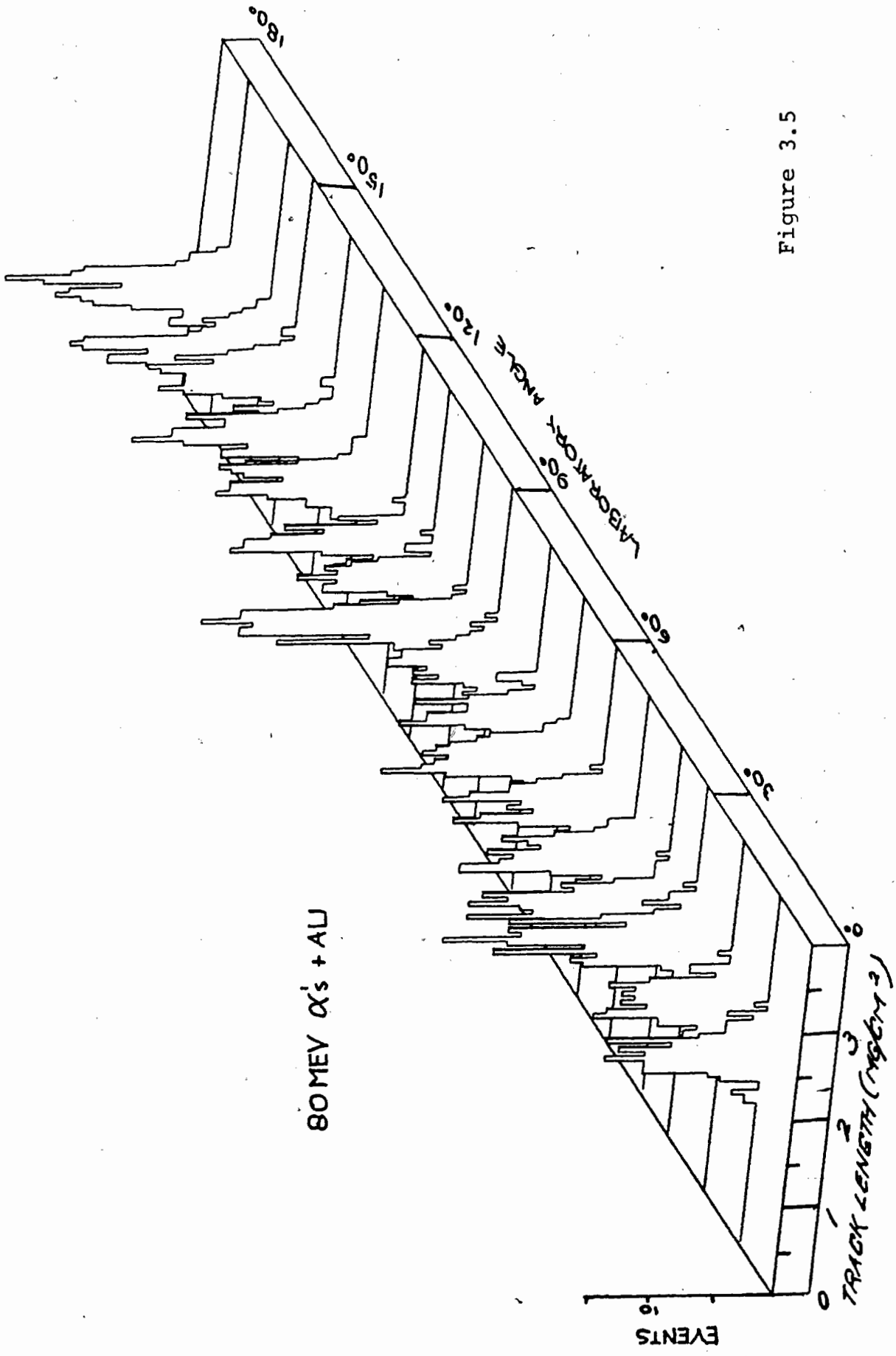
80 MEV α's + ALU
LABORATORY ANGLE
30°
60°
90°
120°
150°
180°
EVENTS
10
0
1
2
3
TRACK LENGTH (MG/CM²)

Figure 3.5

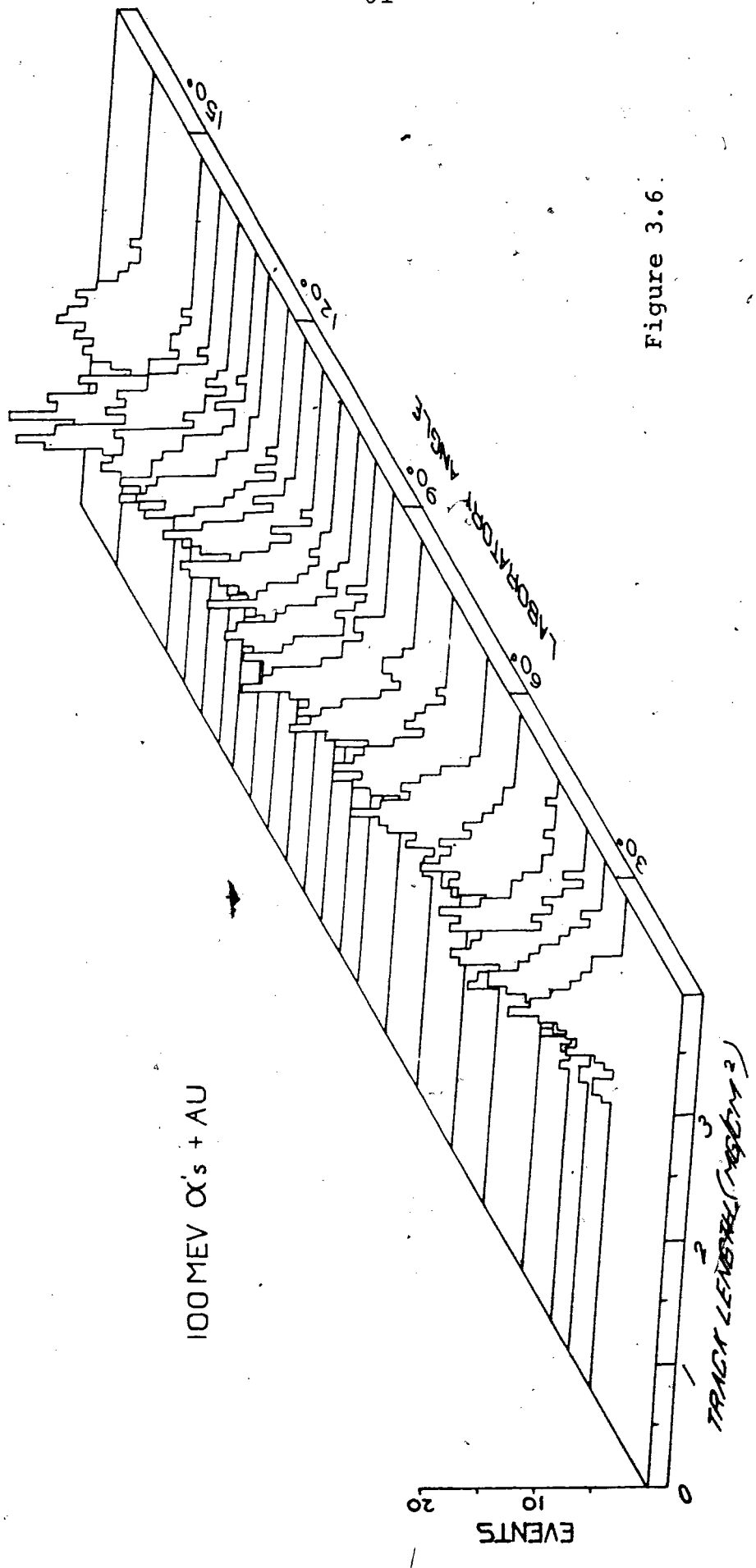

Figure 3.6

Table III.5 80-MeV alpha particles on Gold; summary of experimental data.

laboratory angle (degrees)	scanned area (mm^2)	# of tracks	average peak position (mg/cm^2)	normalized* track density (tr/mm^2)	laboratory angle (degrees)	# of + tracks	normalized* track density (tr/mm^2)
9.6	0.020	108	2.91	5974 ± 575	9.2	1247	6730 ± 191
20.6	0.020	96	2.90	5154 ± 526	14.1	1150	6089 ± 180
31.6	0.040	153	2.98	4210 ± 340	20.2	999	5294 ± 167
39.5	0.040	129	2.91	3467 ± 305	28.2	800	4317 ± 153
49.6	0.040	110	2.88	2953 ± 282	31.8	731	3970 ± 147
59.3	0.040	99	2.83	2801 ± 282	39.8	616	3270 ± 132
69.4	0.055	116	2.84	2264 ± 210	49.9	566	3002 ± 126
79.5	0.040	76	2.73	2094 ± 240	59.2	501	2798 ± 125
91.2	0.040	76	2.67	2040 ± 234	69.7	475	2524 ± 116
100.2	0.079	157	2.59	2065 ± 165	79.7	393	2140 ± 108
110.4	0.040	81	2.46	2115 ± 235	90.9	418	2220 ± 109
118.5	0.040	92	2.39	2456 ± 256	100.0	419	2218 ± 108
130.7	0.040	101	2.37	2707 ± 269	110.2	448	2368 ± 112
140.7	0.040	119	2.33	3186 ± 292	118.2	404	2181 ± 109
152.3	0.040	105	2.22	3136 ± 306	130.4	486	2574 ± 117
159.7	0.040	126	2.20	3431 ± 306	140.5	530	2802 ± 122
171.8	0.040	142	2.20	3800 ± 319	152.3	553	3183 ± 135
					160.0	716	3850 ± 144
					166.0	769	4130 ± 149
					172.0	830	4500 ± 156

* normalized to a common track-target distance of 55mm

\+ for all angles an area of 0.200 mm^2 was scanned

Table III.6 100-MeV alpha particles of Gold; summary of experimental data.

laboratory angle (degrees)	scanned area (mm^2)	# of tracks	average peak position (mg/cm^2)	normalized* track density (tr/mm^2)
26	0.031	75	2.99	2644 ± 305
32	0.046	94	2.97	2233 ± 230
37	0.063	118	2.94	2012 ± 185
45	0.046	81	2.78	1891 ± 210
56	0.063	68	2.78	1180 ± 143
65	0.079	104	2.63	1438 ± 141
75	0.079	89	2.57	1210 ± 128
84	0.079	83	2.47	1148 ± 126
92	0.079	102	2.39	1411 ± 140
97	0.079	98	2.27	1332 ± 135
102	0.079	94	2.29	1278 ± 132
107	0.079	86	2.23	1169 ± 126
112	0.079	101	2.22	1373 ± 137
117	0.079	97	2.23	1342 ± 136
122	0.079	97	2.12	1342 ± 136
127	0.079	95	2.18	1292 ± 133
131	0.079	111	2.16	1509 ± 143
136	0.079	111	2.06	1509 ± 143
141	0.079	141	2.06	1917 ± 161
146	0.079	121	1.98	1674 ± 152
160	0.031	62	1.99	2148 ± 273

* normalized to a common track-target distance of 55mm.

Table III.7 120-MeV alpha particles on Gold; summary of experimental data.

laboratory angle (degrees)	area scanned (mm^2)	number of tracks	track density (tr/mm^2)	laboratory angle (degrees)	area scanned (mm^2)	number of tracks	track density (tr/mm^2)
8.5	0.020	126	6300±561	85.6	0.080	119	1488±136
10.8	0.020	103	5150±507	91.4	0.080	133	1663±144
12.6	0.020	113	5650±532	93.4	0.080	132	1650±144
14.7	0.020	123	6150±555	95.4	0.080	124	1550±139
16.8	0.020	120	6000±548	97.4	0.080	139	1738±147
18.9	0.020	118	5900±543	99.4	0.080	110	1375±131
21.0	0.020	92	4600±480	101.4	0.080	110	1375±131
23.1	0.020	107	5350±517	103.4	0.080	138	1725±147
25.2	0.040	189	4725±344	105.4	0.080	154	1925±155
27.3	0.040	158	3950±314	107.4	0.080	154	1925±155
29.4	0.040	136	3400±292	109.4	0.080	127	1588±141
32.4	0.040	127	3175±282	111.4	0.080	141	1763±148
34.3	0.040	140	3500±296	113.4	0.080	119	1488±136
36.3	0.040	123	3075±277	115.4	0.080	122	1525±138
38.2	0.040	95	2375±244	117.4	0.080	118	1475±136
40.2	0.040	111	2775±263	122.3	0.080	131	1638±143
42.2	0.040	105	2625±256	124.3	0.080	125	1563±140
44.2	0.040	106	2650±257	126.2	0.080	151	1888±154
46.2	0.040	92	2300±240	128.2	0.080	151	1888±154
48.2	0.040	99	2475±249	130.1	0.080	144	1800±150
50.1	0.080	175	2188±165	132.1	0.080	174	2175±165
52.1	0.080	170	2125±163	134.0	0.080	172	2150±164
54.1	0.080	165	2063±161	136.0	0.080	165	2063±161
56.1	0.080	161	2013±159	137.9	0.080	179	2238±167
58.0	0.080	171	2138±163	139.9	0.080	154	1925±155
59.6	0.044	97	2205±224	141.8	0.040	98	2450±247
62.7	0.080	161	2013±159	143.8	0.040	93	2325±241
64.6	0.080	152	1900±154	145.7	0.040	97	2425±246
66.5	0.080	153	1913±155	147.7	0.040	98	2450±247
68.4	0.080	136	1700±146	153.5	0.040	107	2675±259
70.3	0.080	150	1875±153	155.4	0.040	114	2850±267
72.2	0.080	164	2050±160	157.2	0.040	105	2625±256
74.1	0.080	129	1613±147	159.1	0.040	131	3275±286
76.0	0.080	145	1813±151	161.0	0.040	127	3175±282
78.0	0.080	133	1663±144	162.8	0.040	123	3075±277
80.0	0.080	142	1775±149	164.7	0.040	133	3325±288
81.8	0.080	119	1488±136	166.5	0.040	150	3750±306
83.7	0.080	109	1363±131	168.4	0.040	137	3425±293

3.4.2 80-MeV alpha particles on tellurium.

The tellurium target was nearly three times thicker than the indium target, and approximately nine times more alpha particles were incident on the tellurium target than on the indium target (see Table III.1), but because of the decreased energy of the alpha particles, the track density in this experiment was only twice that of the 167-MeV alpha particles on indium experiment.

By scanning a relatively large area of around 10 mm^2 for each five degree interval, sufficient data were obtained to determine the distribution in track length of the fission fragments as a finction of the laboratory angle of observation. No data could be obtained for angles less than 40 degrees, due to the very large concentration of small pits in the mica surface. For angles of around 30 degrees, fission tracks can sometimes be seen embedded in the background of pits; but measurement of the length of these tracks becomes arbitrary. At an angle of observation of 20 degrees, these tracks can no longer be resolved from the general background. The interaction of scattered alpha particles with heavier nuclei in the mica are thought to be the most likely explanation of these small pits as was discussed in section 3.3.2.

Figure 3.7 shows the track length distributions as a function of the angle of observation, while Table III.8 summarizes the data. The mean laboratory angle was determined by calculating the arithmetical average of the laboratory angle of all tracks measured in each five degree interval.

3.4.3 80-MeV alpha-particles on silver.

The number of 80-MeV alpha-particles incident on the silver target was very large (see Table III.1), resulting in track densities of around 50 tracks/mm^2. Track length distributions were measured for laboratory angles of observation from 50 to 170 degrees. Measurements of tracks could not be made for smaller angles of observation for the same reasons as discussed in the previous section. Figure 3.8 and Table III.9 summarize the experimental data.

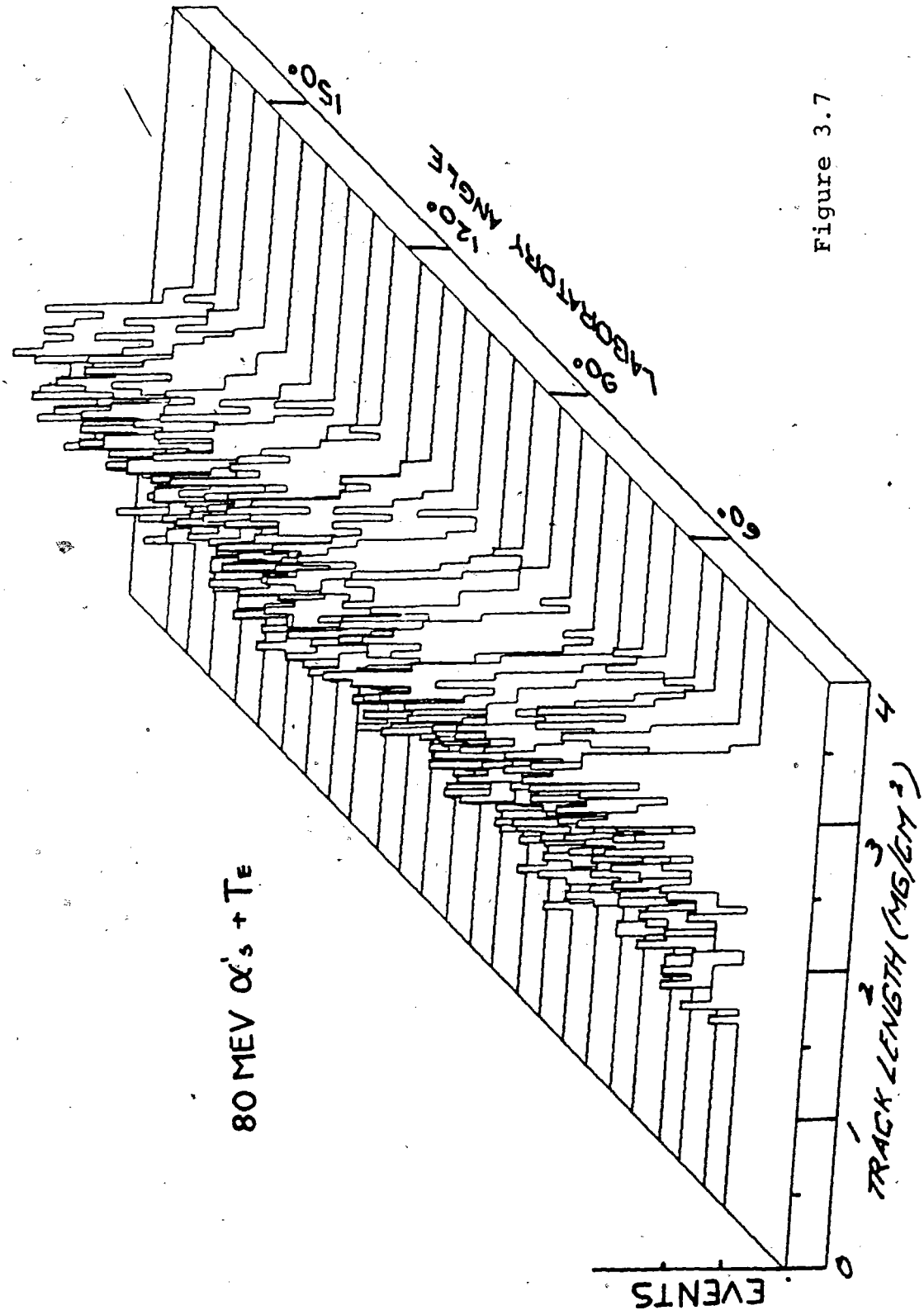
80 MEV α's + Te
LABORATORY ANGLE
150°
120°
90°
60°
EVENTS
0
TRACK LENGTH (MG/CM²)
2
3
4

Figure 3.7

Table III.8 80-MeV alpha particles on tellurium: Summary of experimental data.

angular interval scanned (degrees)	mean laboratory angle (degrees)	area scanned (mm^2)	number of tracks	average peak position (mg/cm^2)	normalized* track density (tr/mm^2)
40-45	43.1	10.942	98	2.58	8.73 ± o.88
45-50	47.4	10.951	104	2.55	9.43 ± 0.92
50-55	52.7	10.947	114	2.51	10.08 ± 0.94
55-60	56.9	10.944	108	2.51	10.08 ± 0.97
60-65	62.8	13.025	101	2.41	7.50 ± 0.75
65-70	67.5	13.126	127	2.30	9.29 ± 0.82
70-75	72.5	13.163	121	2.28	8.93 ± 0.81
75-80	77.5	13.167	110	2.20	8.26 ± 0.79
80-85	82.6	13.133	102	2.21	7.65 ± 0.76
85-90	87.3	13.070	115	2.18	8.67 ± 0.81
90-95	92.8	11.660	105	2.16	8.78 ± 0.86
95-100	97.4	11.822	96	2.12	7.92 ± 0.81
100-105	102.5	11.830	93	2.15	7.66 ± 0.79
105-110	107.7	11.830	88	2.10	7.25 ± 0.77
110-115	112.5	11.819	96	2.09	7.89 ± 0.81
115-120	117.2	11.798	74	1.99	6.25 ± 0.73
120-125	123.0	7.714	78	2.03	9.93 ± 1.12
125-130	127.5	7.682	70	1.94	8.98 ± 1.07
130-135	132.5	7.200	87	1.92	11.82 ± 1.27
135-140	137.5	7.216	81	1.87	11.02 ± 1.22
140-145	142.6	7.223	84	1.84	11.42 ± 1.25
145-150	147.5	7.231	99	1.88	13.49 ± 1.36
150-155	152.9	5.406	77	1.83	14.14 ± 1.61
155-160	157.6	5.400	77	1.80	14.16 ± 1.61
160-165	162.0	5.491	93	1.78	16.81 ± 1.74

* normalized to a common track-target distance of 55 mm.

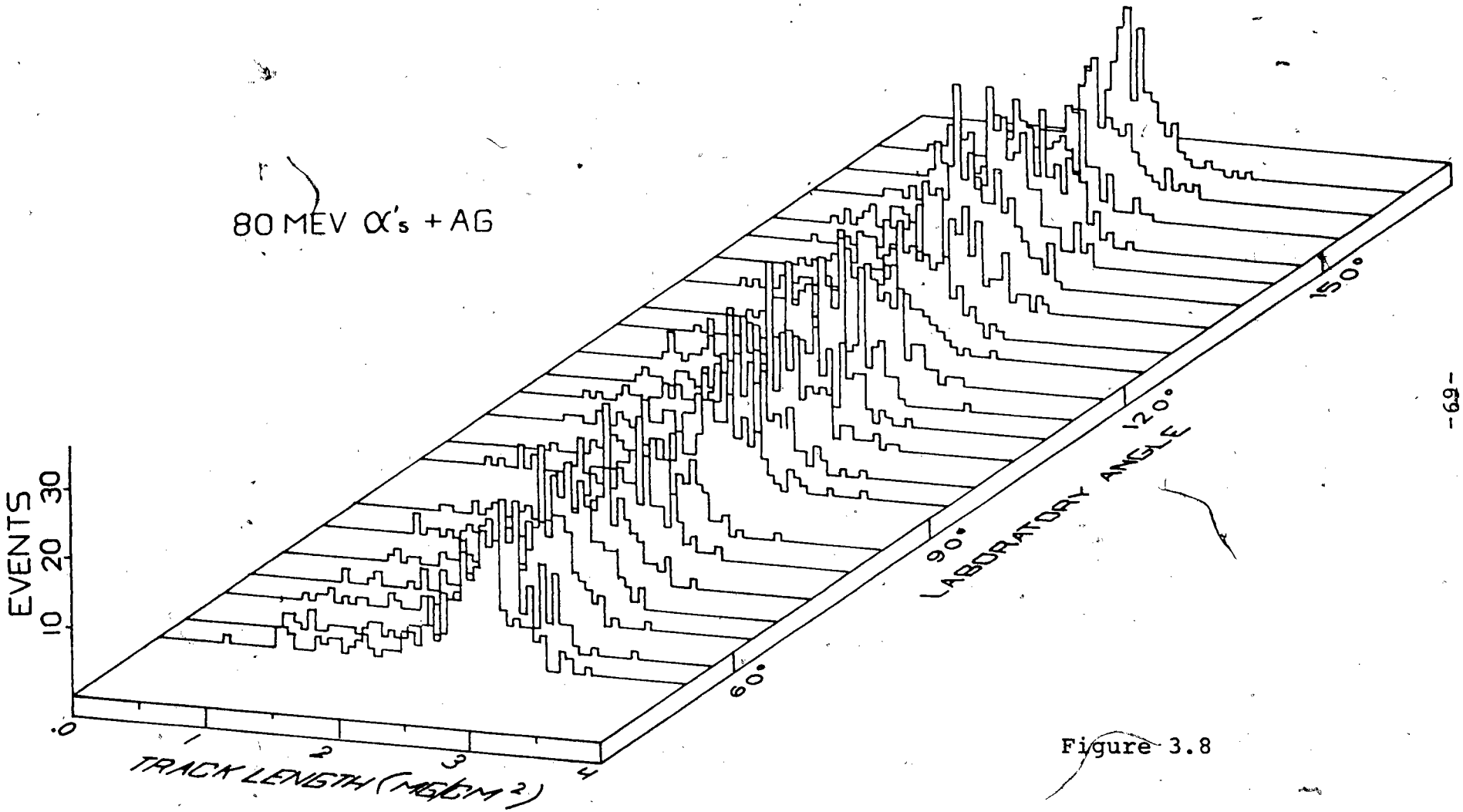
80 MEV α's + AG
EVENTS
10
20
30
0
1
2
3
4
TRACK LENGTH (MG/CM²)
60°
90°
120°
150°
LABORATORY ANGLE

Figure 3.8

Table III.9 80-MeV alpha particles on silver: Summary of experimental data.

angular interval scanned (degrees)	mean laboratory angle (degrees)	area scanned (mm^2)	number of tracks	average peak position (mg/cm^2)	normalized* track density (tr/mm^2)
50-55	53.1	4.882	214	2.35	45.4 ± 3.0
55-60	57.0	4.718	212	2.34	46.9 ± 3.2
60-65	62.8	4.389	187	2.33	42.9 ± 3.1
65-70	67.6	4.755	239	2.33	49.5 ± 3.2
70-75	72.3	4.735	193	2.29	39.9 ± 2.9
75-80	77.6	4.752	183	2.22	37.7 ± 2.8
80-85	82.5	4.805	173	2.18	35.3 ± 2.7
85-90	86.9	4.164	144	2.19	34.0 ± 2.9
90-95	93.1	3.810	163	2.16	42.6 ± 3.3
95-100	97.5	4.785	204	2.18	41.9 ± 3.0
100-105	102.5	4.744	238	2.11	48.8 ± 3.2
105-110	107.5	4.739	211	2.04	43.3 ± 3.0
110-115	112.4	4.771	250	2.11	51.4 ± 3.3
115-120	117.3	4.537	273	2.00	59.6 ± 3.6
120-125	123.0	3.202	132	2.00	41.5 ± 3.6
125-130	127.5	3.849	186	1.99	48.1 ± 3.5
130-135	132.6	3.821	214	1.90	55.3 ± 3.8
135-140	137.5	3.822	260	1.92	67.3 ± 4.2
140-145	142.5	3.853	234	1.91	60.6 ± 4.0
145-150	147.3	3.453	247	1.88	72.2 ± 4.6
150-155	153.1	2.277	161	1.80	70.8 ± 5.6
155-160	157.5	2.872	219	1.82	75.6 ± 5.1
160-165	162.6	2.872	256	1.75	88.5 ± 5.6
165-170	165.7	0.578	49	1.74	85.2 ±12.1

* normalized to a common track-target distance of 55 mm.

Chapter 4 Interpretation of fission fragment track length distributions.

In nearly all previous experimental studies of the fission process, using dielectric track detectors, the aim has been simply to register a fission event. Positive identification of a fission event could only be made in a "sandwich" experiment, where the target was sandwiched between two detectors, and the two coincident fission fragments could be observed (Hud 69, Bra 71, Kie 73). In a scattering chamber type of experiment the coincidence criterion is lost, and hence, the origin of the tracks can only be deduced from track length and angular distribution data. By choosing a detector which will discriminate against light ($Z < 10$) particles as well as low energy ($E < 1MeV$) particles, the tracks that are formed are those of energetic heavier fragments, including those from a fission process. Glass, Makrofol and mica have been used extensively towards this end (Met 71, Kon 65, Ral 73, Bra 67, Kas 72, Itk 72, Bur 64, Zeb 74).

Not until the work of Khodai-Joopari (Kho 66) was mention made of the possibility of distinguishing impurities by their shorter or longer average track length as compared to the tracks of interest. However, this was only an expectation since no data on the response of heavy ions in mica were available. Pate and Péter (Pat 71) did a rough calibration of the track length of aluminum, argon and krypton ions in

mica and used these results to distinguish the tracks of impurities with a heavier mass from targets with lighter masses. They also traced the variation of track length distributions with the mass of the fissioning system and, under the assumption that the track length distribution was directly proportional to the mass distribution, concluded that no significant broadening effect of the mass distribution with decreasing mass of the fissioning system was indicated. By assuming that the average track length represented the track length of the most probable fission fragment, which was known to be one half of the mass of the fissioning system (assuming a symmetric mass distribution), the approximate energy of this most probable fragment was also extracted in this experiment. However, all these assumptions rely on the mass and energy distribution being relatively narrow. Liquid drop theory (Nix 69) predicts a substantial broadening of the mass distribution with decreasing mass of the fissioning system. The above mentioned approximations are then no longer valid and a more rigorous approach must be taken.

4.1 Calculation of fission fragment track length distributions.

In the following a description is given of how one can calculate track length distributions using a reasonable model for the fission process of medium mass nuclei and the known response of heavy ions in mica. The calculated track length distri-

butions can then be compared with measured distributions, and some aspects of the calculations modified to obtain better agreement with the experimental data. The model which will result in an optimum "fit" to the experimental data is assumed to be the closest representation of the real fission process under consideration. This approach was chosen because the high degree of complexity of both the fission process and the stopping process of heavy ions in mica, plus the fact that a track length only represents a whole set of possible mass and energy combinations, renders direct extraction of fission parameters from track length distributions impossible.

A computer program RADICS (for RAnge DIstribution CalculationS) was written, which simulates the fission process of medium mass ($50 < A < 200$) nuclei, induced by any kind of particle, and the subsequent stopping process of the fission fragments in either mica or glass detectors. Glass detectors were included because some extensive calibration data on the response of heavy ions in glass are now available (Lec 72). The aim of the method was to be able to reproduce experimental fission fragment track length or diameter distributions by varying as small a number of parameters as possible. Hence, it was necessary to make a number of simplifications and assumptions about some of the parameters as well as to enter accepted experimental values for some other parameters that were not varied in the calculations. Quantities that were

left free to vary were: a) the shape of the mass distribution of the fission fragments; b) the total kinetic energy release in the case of symmetric fission and c) the center-of-mass motion of the fissioning system.

Appendix 1 gives a complete description of the mathematical procedure as well as the use of this program. Basically the track length or diameter distribution at a given laboratory angle of observation in considered to be a summation over all the individual track length or diameter distributions of each possible fragment mass, each weighted by the probability of emitting that particular fragment mass at that angle of observation. The problem is then reduced to finding the energy distribution associated with each possible fragment mass and the conversion of this to a track length or diameter distribution. If the energy distributions are relatively narrow, a linear transformation from energy to track length or diameter can be performed under the assumption of local linearity of the track length or diameter versus energy curves.

In the calculations it is assumed that the energy distribution of the fragments of a given mass is of a gaussian nature. Dispersion effects due to such effects as target thickness and angular resolution can then be more easily included (see appendix 1).

The code can be used as a tool to investigate the sensitivity

of fission parameters to the shape of the track length or diameter distributions of fission fragments. One of the interesting questions is how the track length or diameter distributions will vary with the mass of the fissioning system. In a sample calculation, fission was assumed induced by 80-MeV alpha-particles in target nuclei with mass values ranging from 100 to 200 amu. The mass distribution of the fission fragments was assumed to be gaussian with a full width at half maximum of 50 amu. (Later it will be shown that the width of the mass distribution is relatively insensitive to the outcome of the calculations.) Fission barrier values were taken from the work of Myers and Swiatecki (Mye 66), while the total kinetic energy release was taken from the calculations of Nix (Nix 69).

The track length distributions, as they would be observed in mica detectors at laboratory angles of observation of 30 and 150 degrees, are shown in figures 4.1 and 4.2. Using glass detectors, the diameter distributions that would be observed at these same angles of observation, are shown in figures 4.3 and 4.4. The most interesting feature, in the case of mica detectors, is that the width of the track length distribution is not a constant value, or even a monotonic function of the mass of the fissioning system.

In figure 4.5 the full width at half maximum of the track length or diameter distribution is given as a function of the

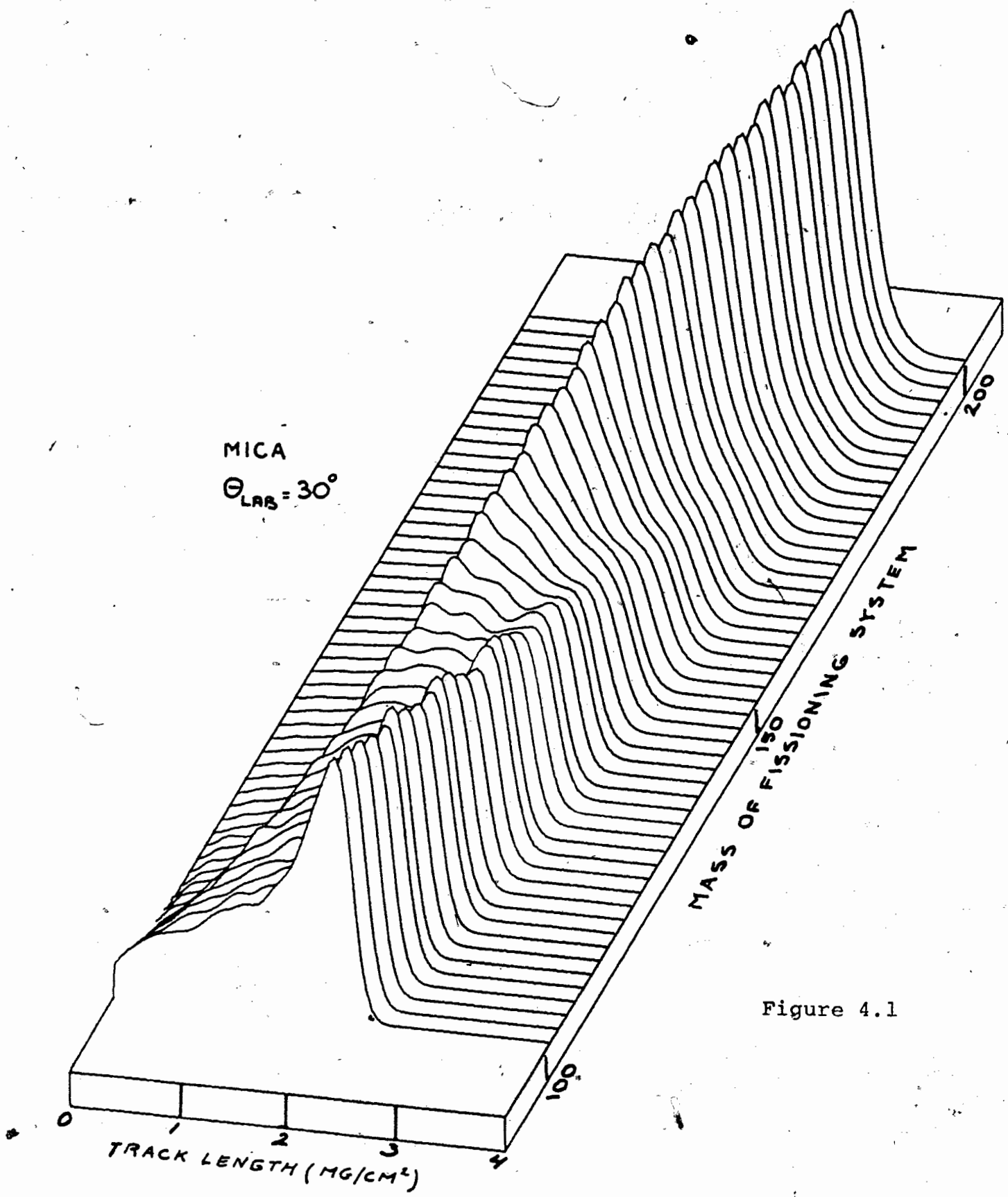
MICA
$\Theta_{LAB} = 30°$
MASS OF FISSIONING SYSTEM
100
150
200
0
1
2
3
4
TRACK LENGTH (MG/CM²)

Figure 4.1

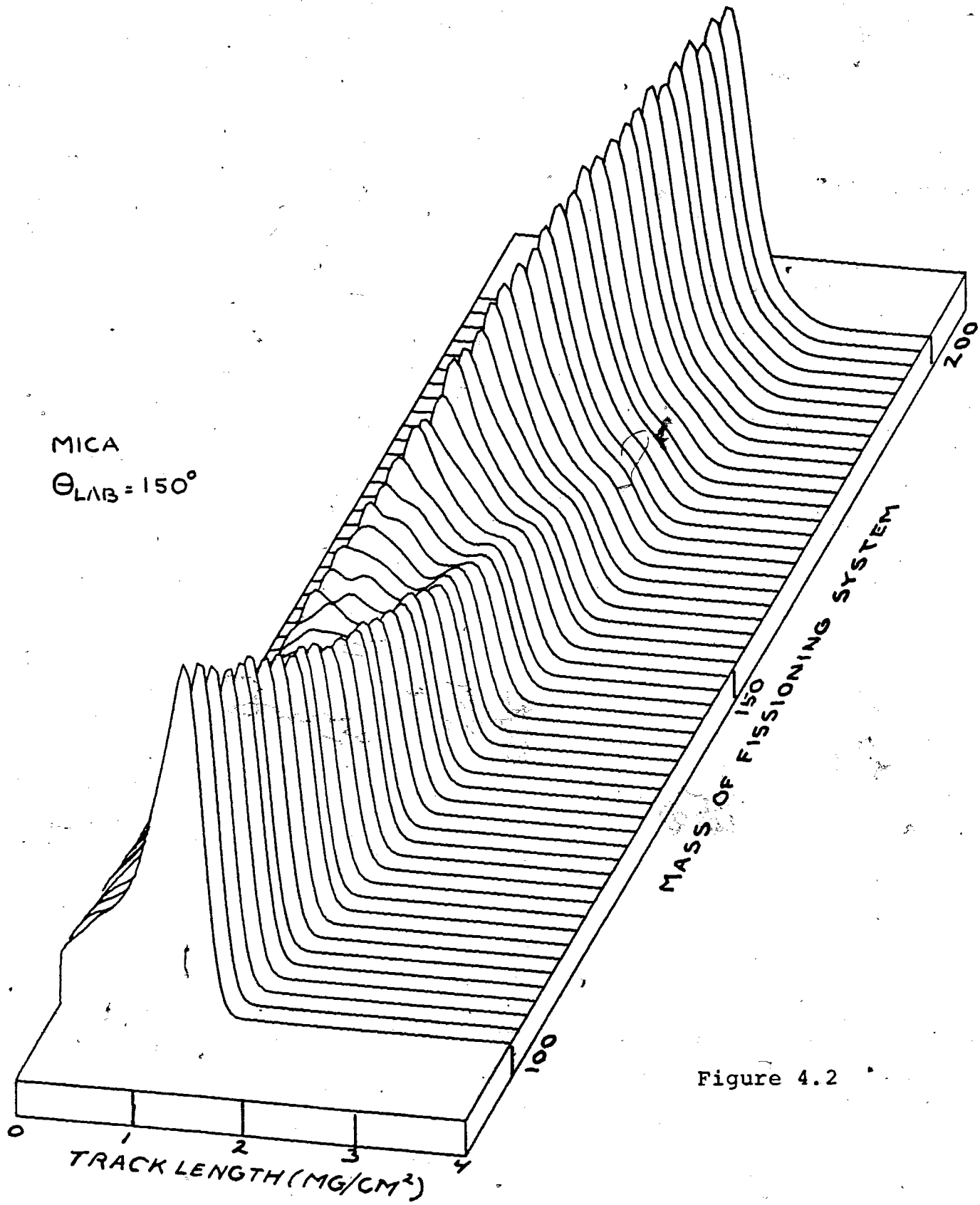
MICA
$\theta_{LAB} = 150°$
MASS OF FISSIONING SYSTEM
100
150
200
0
1
2
3
4
TRACK LENGTH (MG/CM²)

Figure 4.2

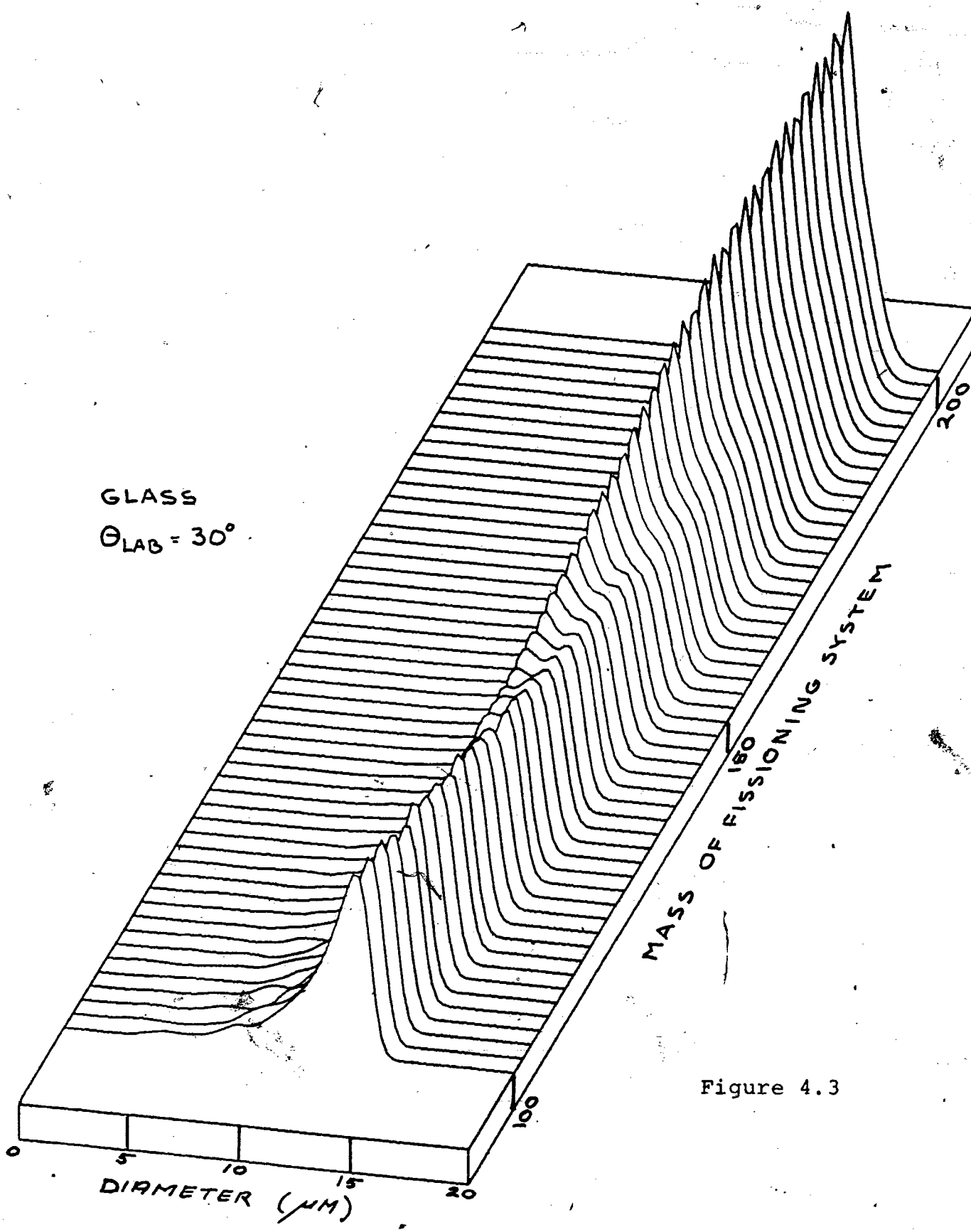
GLASS
$\theta_{LAB} = 30°$
0
5
10
15
20
DIAMETER (μM)
100
180
200
MASS OF FISSIONING SYSTEM

Figure 4.3

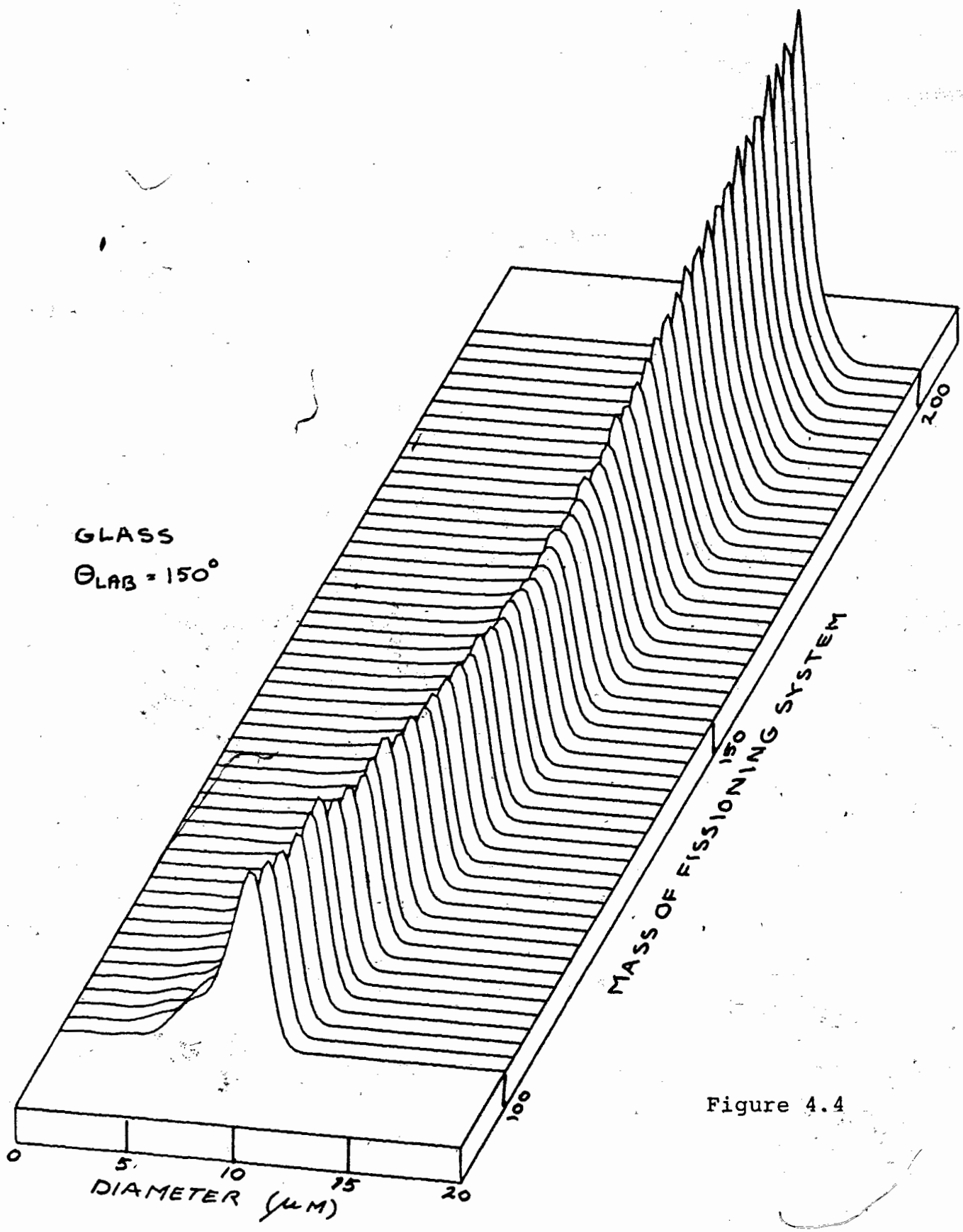
GLASS
$\theta_{LAB} = 150°$
0
5
10
15
20
DIAMETER (μM)
100
150
200
MASS OF FISSIONING SYSTEM

Figure 4.4

figure 4.5A

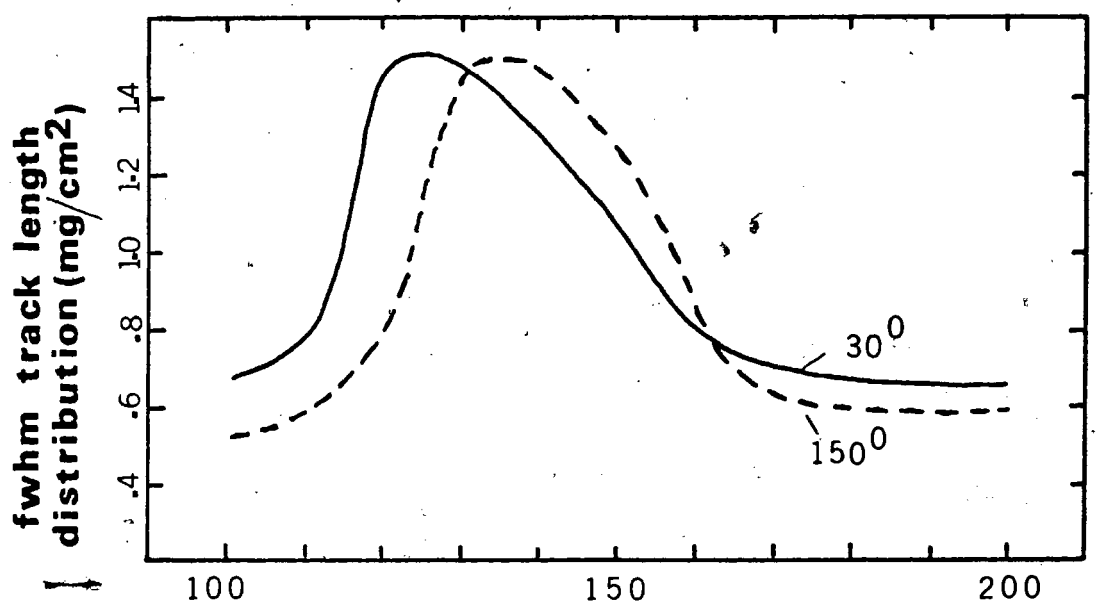

figure 4.5B

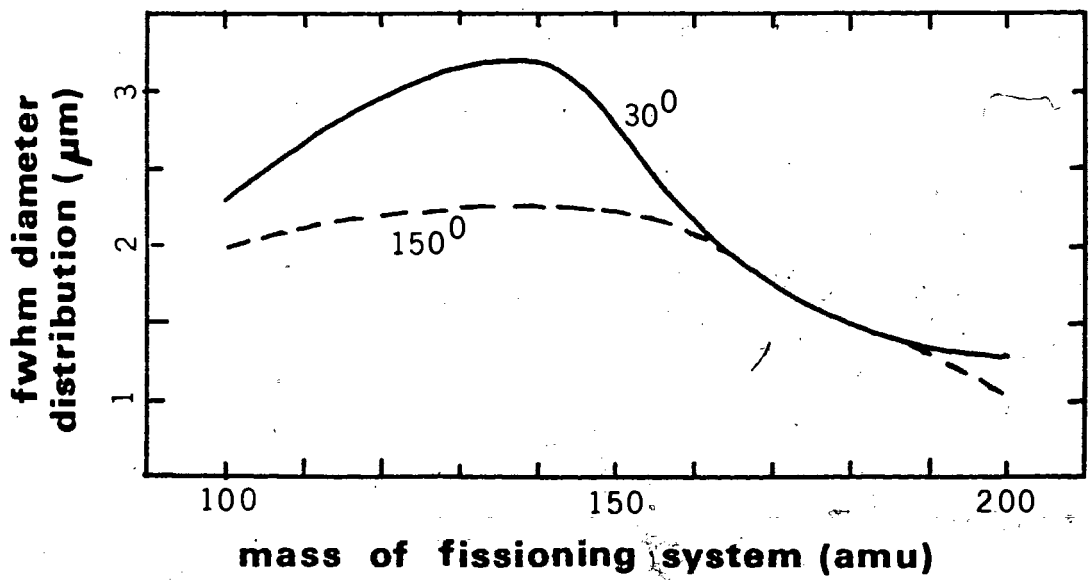

mass of the fissioning system for the two angles of observation; 30^{o} (solid line) and 150^{o} (broken line). The effective broadening of the distributions around a fissioning mass of 130 amu is many times stronger in the case of mica than in the case of glass detectors. Defining the effective broadening as FWHM/Xprob, where Xprob is the most probable track length or diameter value of the distribution, this variable will range from 0.3 to 1.0 in the case of mica and from 0.07 to 0.18 in the case of glass. The comparable effective optical resolution in measuring track length and diameter is in the order of 0.03 and 0.05 respectively. The broadening of the track length distribution around a fissioning system mass of 130 amu should therefore, be quite noticeable, whereas the broadening of the diameter distribution is only just outside the experimental accuracy.

In figure 4.6 the calculated most probable track length and diameter (solid lines) is compared with the track length and diameter of the fragments from a symmetric fission event (broken lines). Again, whereas in the case of glass detectors, especially at backward angles, the difference between these two quantities is less than 5%, in the case of mica detectors large discrepancies exist. This effect is mainly due to a "bunching" of the track length-energy curves in regions around a fragment mass of 45 amu and 80 amu. For a fissioning system mass of around 130 amu, these two regions of fragment mass are present simultaneously, resulting in a quasi "double humped"

figure 4.6A

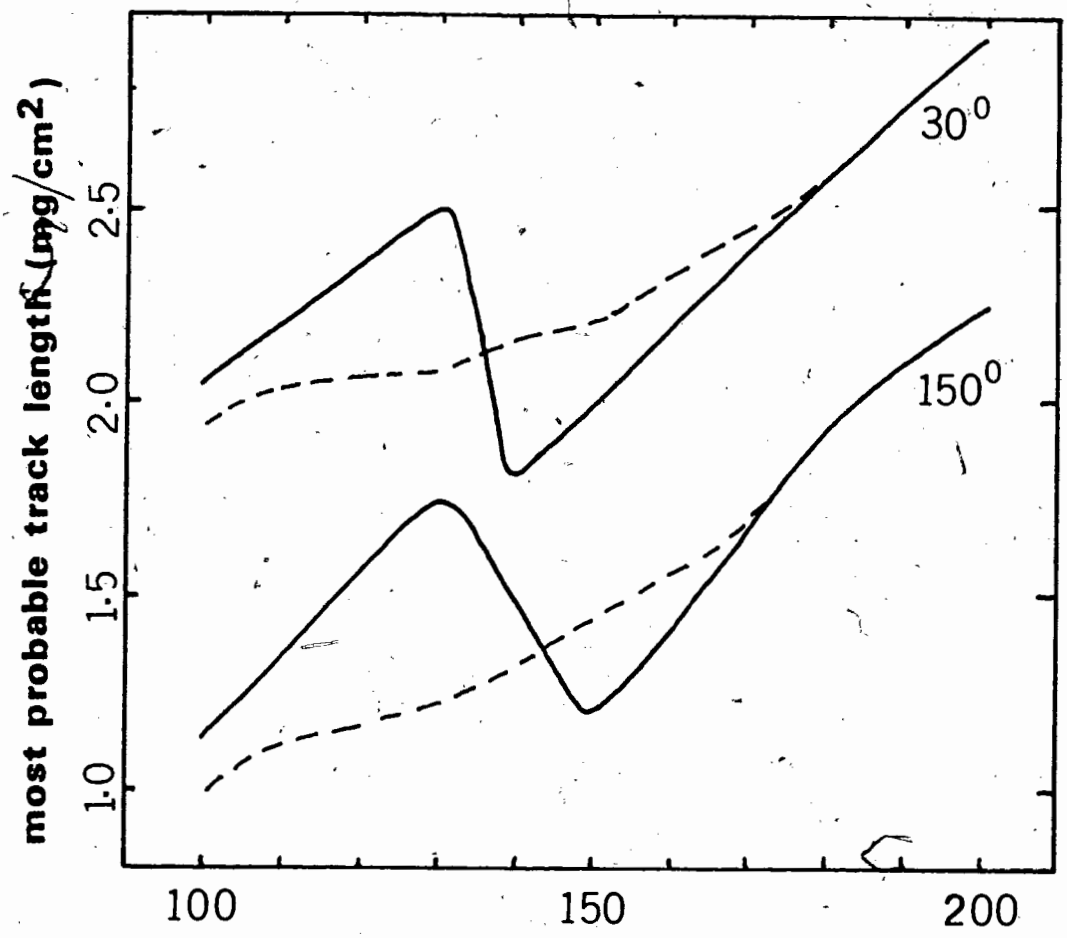

figure 4.6B

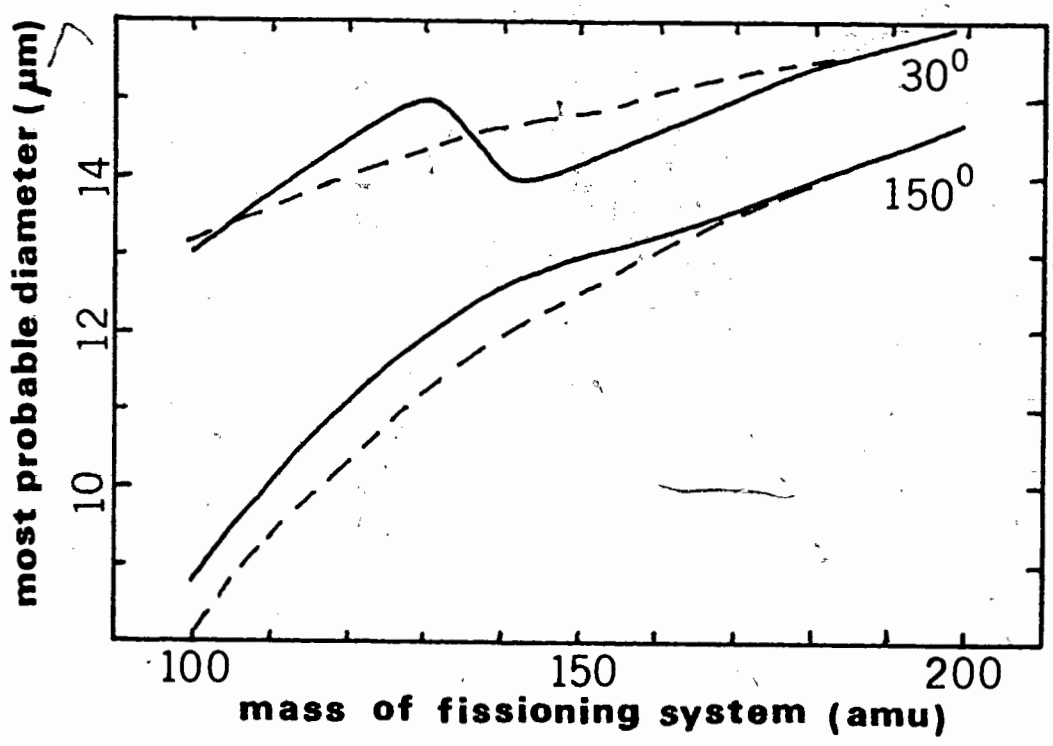

track length distribution (see figures 4.1 and 4.2). The slight shift towards higher more probable diameter values at backward angles of observation is the direct result of the fact that the mass distribution as seen at such laboratory angles of observation contains relatively more light fragments than heavy fragments (see appendix 1, section 1.6). Since the light fragments have higher energy and diameter values associated with them, the most probable diameter value will also shift towards higher values.

The variation of the track length and diameter distributions with the shape of the mass distribution of the fission fragments in examined in figures 4.7, 4.8 and 4.9 for fissioning systems with a mass of 104, 154 and 204 amu respectively. In each calculation it was assumed that the fission fragment mass distribution was of a single gaussian type with a full width at half maximum of 30, 45, 60, 100 and 1000 amu. Fission was again induced by 80 MeV alpha particles and compound nucleus formation was taken to precede the fission step. The resulting track length and diameter distributions were calculated for three angles of observation; 30, 90 and 150° with respect to the beam direction. From figures 4.7 to 4.9 some general characteristics are immediately obvious; a) mica detectors are more sensitive to the shape of the fission fragment mass distribution than glass detectors and b) the track length and diameter distributions at forward angles of observation as well as from heavier masses of the

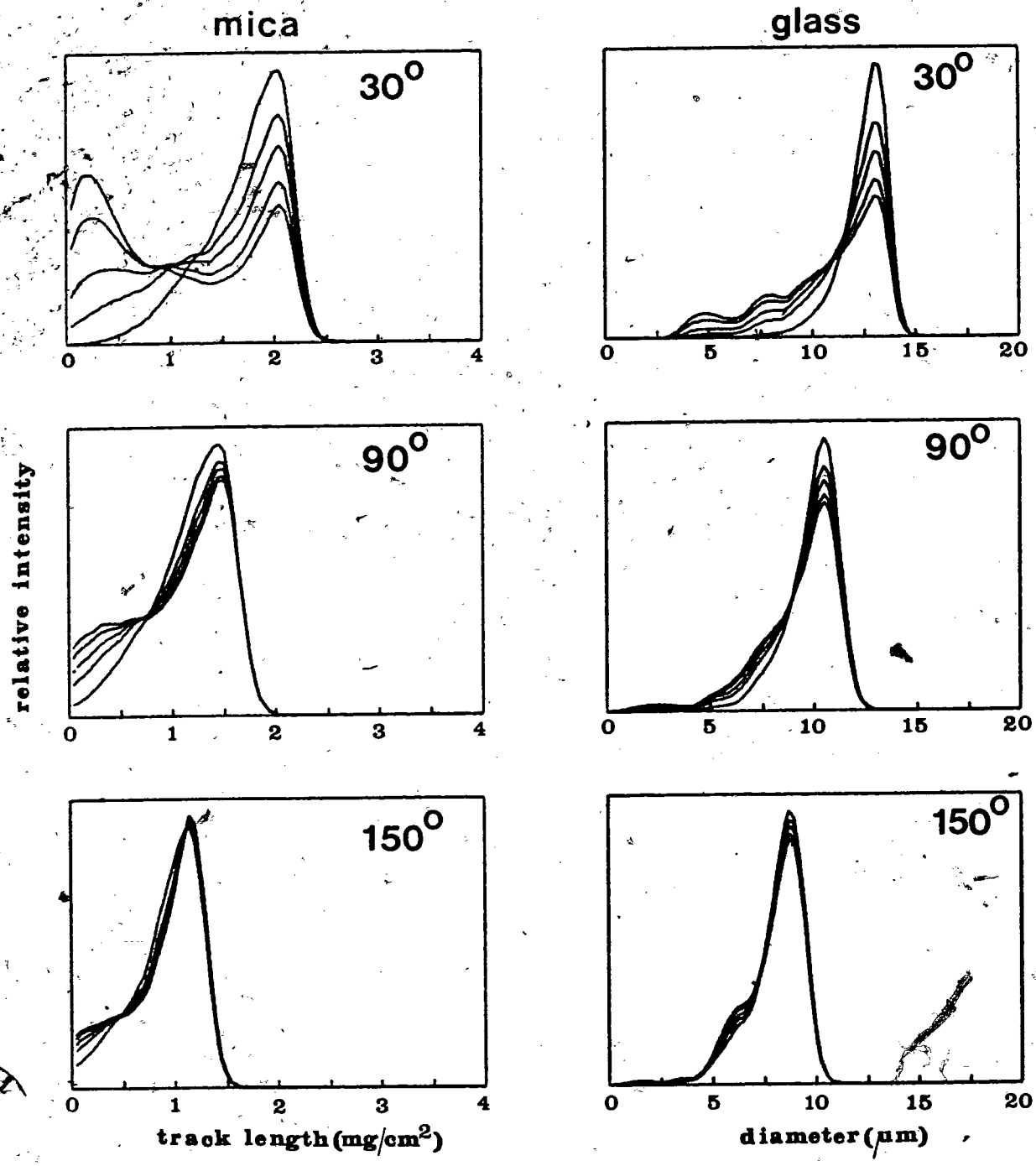

figure 4.7

mass = 104 amu

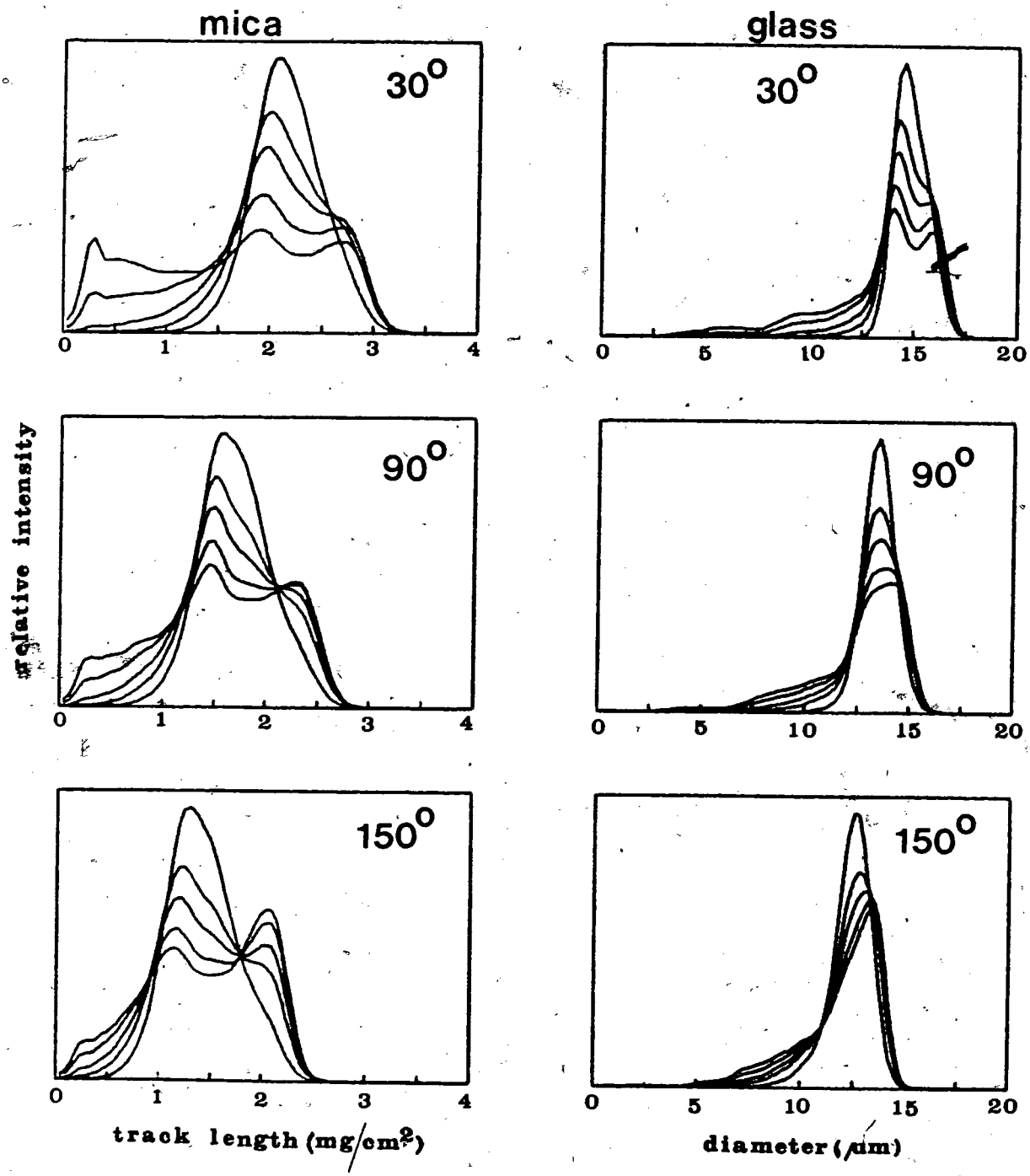

figure 4.8

mass=154 amu

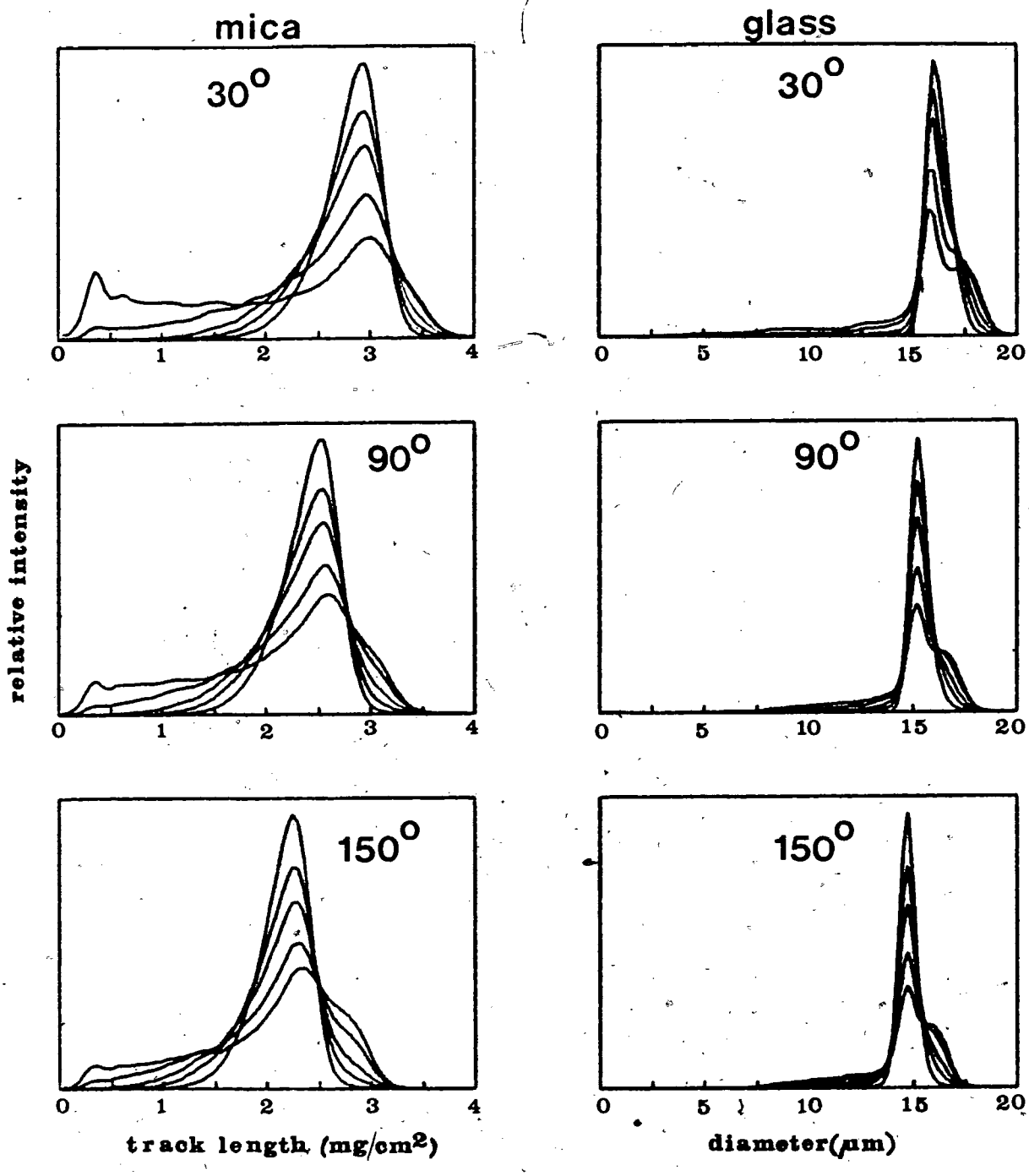

figure 4.9

mass= 204 amu

fissioning system are also more sensitive to the shape of the mass distribution. Since any significant broadening of the mass distribution is only expected (Nix 69) to occur for the lighter fissioning nuclei, such an effect will be very difficult to observe using mica or glass detectors.

From all of the above calculations it can be seen that the assumption of various authors (Kho 66, Pat 71) that impurities in their fissioning target nuclei could be distinguished by their average shorter or longer track length, have to be treated cautiously. Furthermore, the conclusion drawn by Pate and Péter (Pat 71), that the absence of any significant broadening of the track length distributions with decreasing mass of the fissioning system indicated no substantial broadening of the fission fragment mass distributions, is not at all substantiated by the results shown in figures 4.7 through 4.9.

4.2 Comparison with experimental data.

4.2.1 80-, 100- and 167-MeV alpha particles on gold.

The fission fragment track length distributions presented in Chapter 3 can be compared with calculated distributions. The data which are most easily interpreted are those track length distributions for which the most probable track length is provided by fragments with the most probable mass value. Of the available data only the track length distributions from the alpha plus gold systems contain this simplification (see Fig. 4.6). For these cases the analysis in terms of total kinetic energy release and center of mass motion can be made independently of the choice of the width of the mass distribution.

In figures 4.10, 4.11 and 4.12 the experimentally determined average track length, as a function of the laboratory angle of observation, is compared with the calculated average track length for the 80-, 100- and 167-MeV alpha particles on gold bombardments. Various combinations of total kinetic energy release and center-of-mass motion were used in the calculations. The optimum values for these two parameters were obtained by an interative procedure in which the total kinetic energy release value was first adjusted from the theoretical value (Nix 69) to give agreement between the calculated and experimental average track length at 90^{o} (laboratory angle).

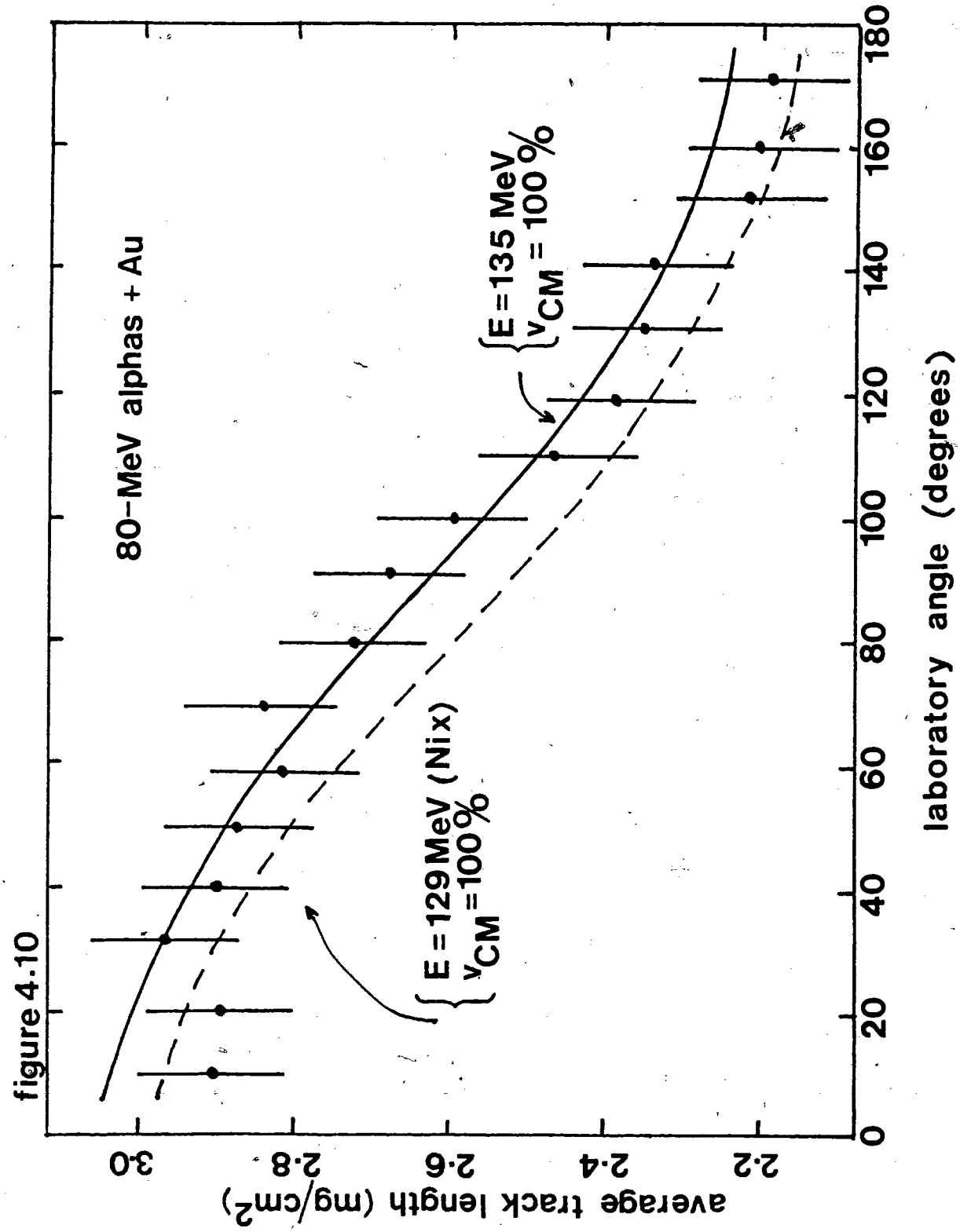
80-MeV alphas + Au
E = 135 MeV
v_{CM} = 100 %
E = 129 MeV (Nix)
v_{CM} = 100 %
average track length (mg/cm^2)
2·2
2·4
2·6
2·8
3·0
laboratory angle (degrees)
0
20
40
60
80
100
120
140
160
180

figure 4.10

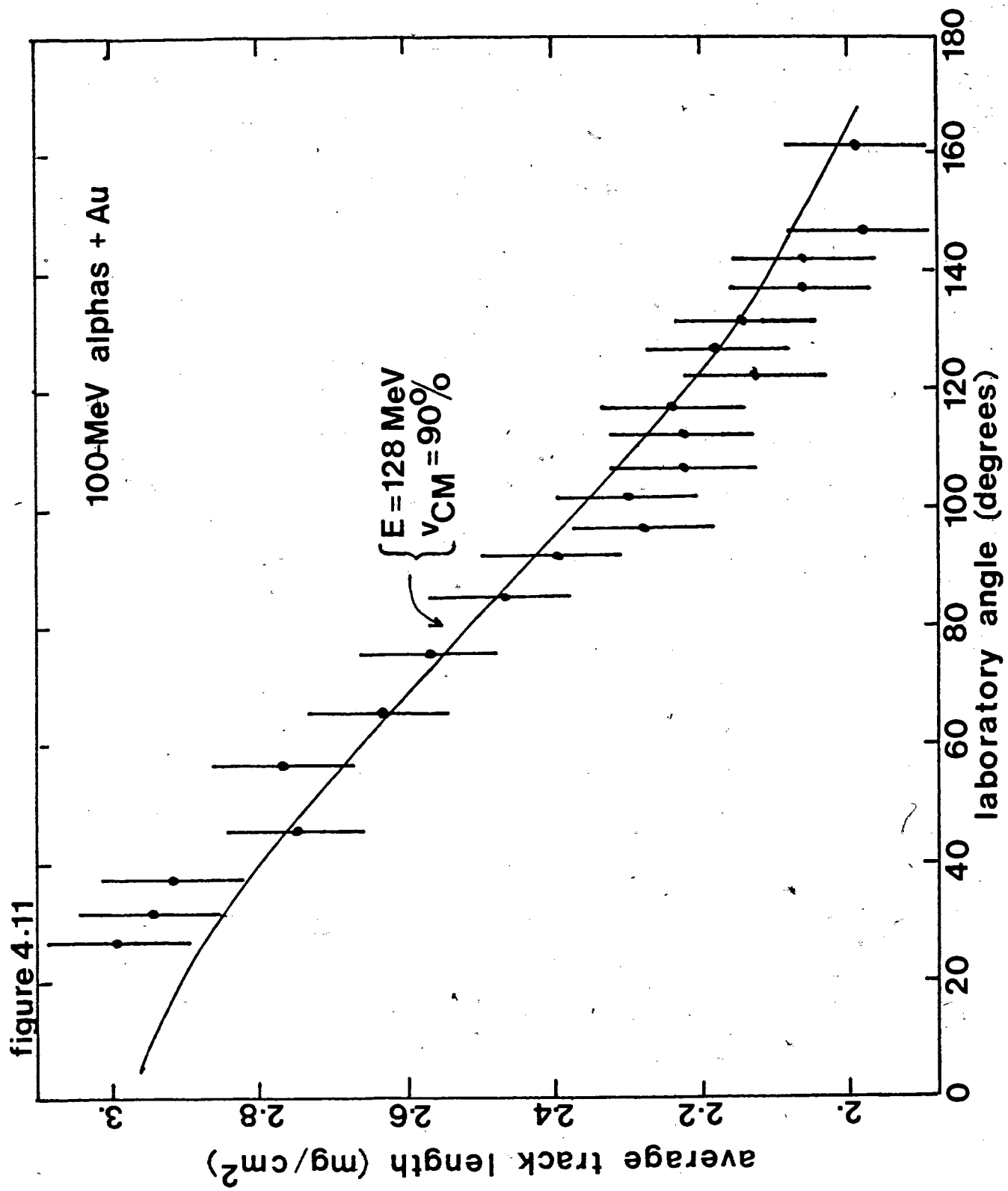
100-MeV alphas + Au
E=128 MeV
v_{CM}=90°
average track length (mg/cm^2)
laboratory angle (degrees)
2.
2·2
2·4
2·6
2·8
3·
0
20
40
60
80
100
120
140
160
180

figure 4.11

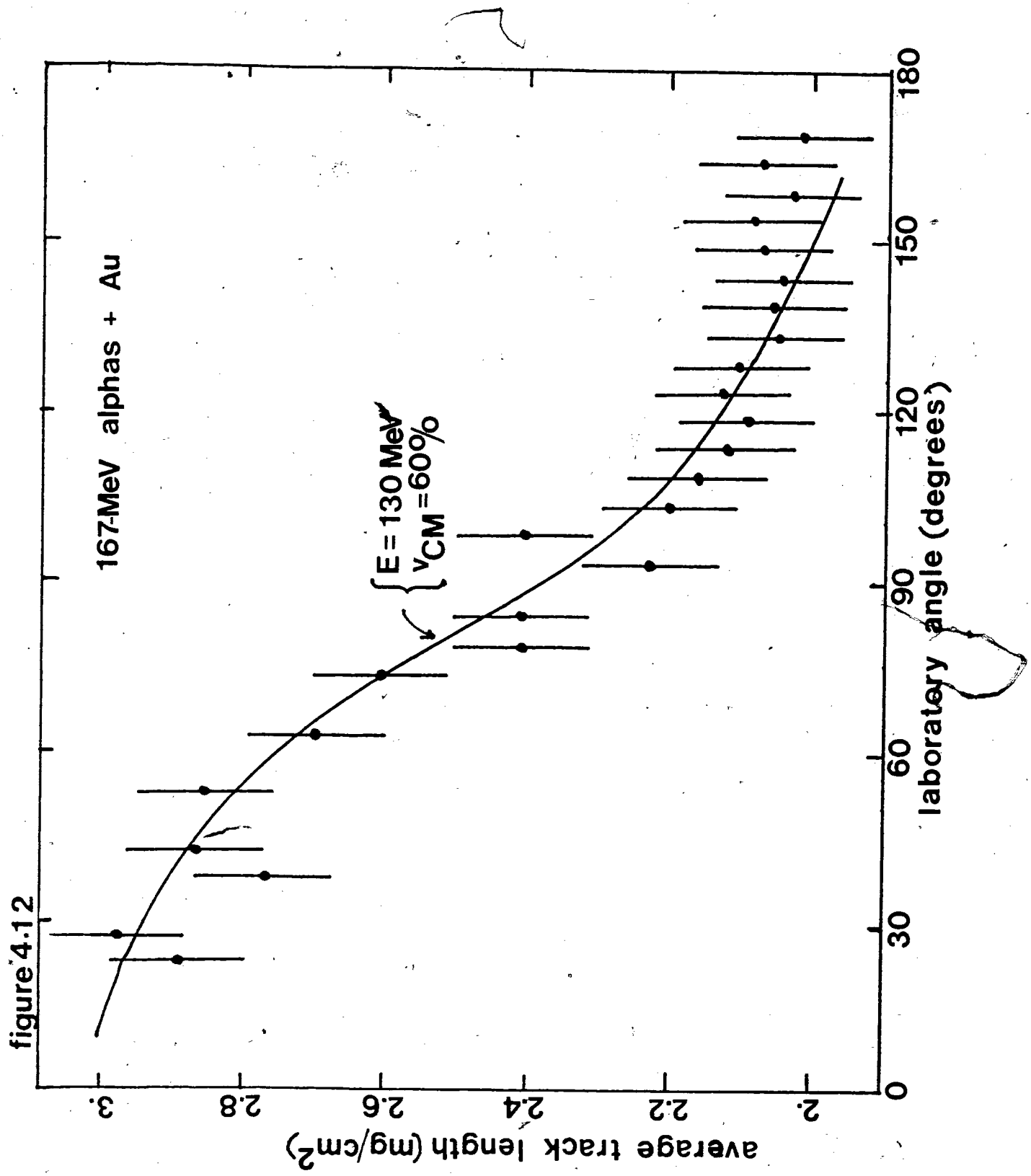
167-MeV alphas + Au
E = 130 MeV
v_{CM} = 60%
average track length (mg/cm^2)
laboratory angle (degrees)
2.
2.2
2.4
2.6
2.8
3.
0
30
60
90
120
150
180

figure 4.12

Next the amount of center-of-mass motion was adjusted from the compound nucleus value to a value which more accurately reflected the trend of the experimental data. If necessary the whole procedure was repeated to obtain a better "fit" to the experimental data.

Using these "fitted" values of total kinetic energy release and center of motion the track length distributions are compared with calculated distributions assuming a range of values for the width of the mass distribution of the fission fragments. Figure 4.13 shows some of the results from these comparisons. It is only possible to assign an upper and lower limit on the width of the mass distribution in each case, and even these values are limited by the assumption of a known distribution in kinetic energy of the fragments (taken to be the theoretical (Nix 69) value). Table IV.1 summarizes parameter values derived from the experimental data on the gold bombardments using the RADICS code. The errors indicate only the accuracy of the fitting procedure.

Total kinetic energy release values are in agreement with the value obtained by other methods (Pla 66). With increasing excitation energy one would expect the compound nucleus to emit more particles, thereby decreasing the average mass of the fissioning nuclei (see Chapter 5). Consequently the total kinetic energy release of the system is expected to show a decrease with increasing excitation energy. For the 167-MeV

figure 4-13

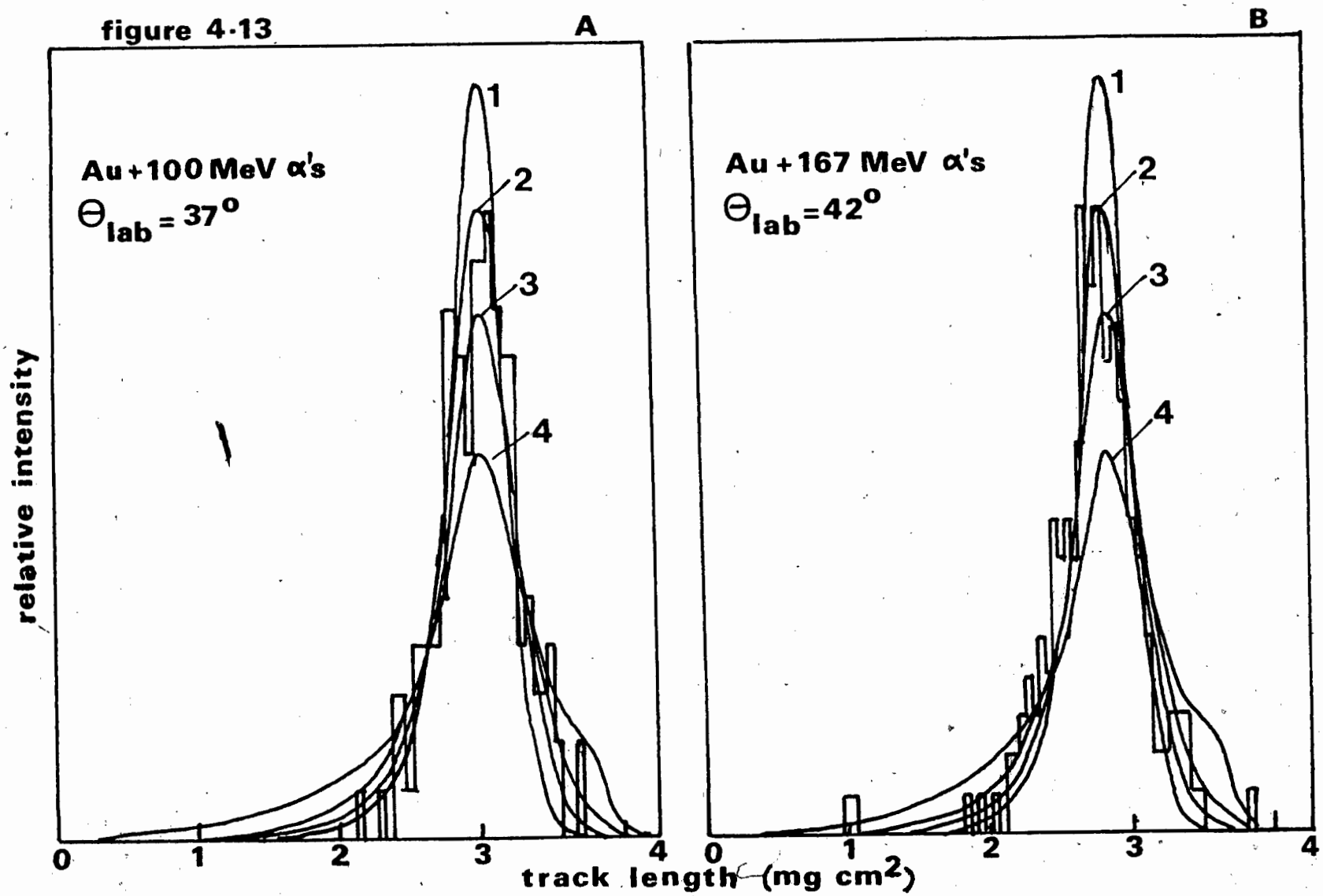
A
B
Au + 100 MeV α's
$\Theta_{lab} = 37^o$
Au + 167 MeV α's
$\Theta_{lab} = 42^o$
1
2
3
4
relative intensity
0
1
2
3
4
track length (mg cm^2)

Table IV.1 Total kinetic energy release, center-of-mass motion and the width of the fission fragment mass distribution as derived from the track length distribution of the fission fragments from the 80-,100- and 167-MeV alpha bombardments of gold.

incident alpha particle energy (MeV)	average total kinetic energy release (MeV)	center-of-mass motion (% of compound nucleus value)	full width at half maximum of the mass distribution (amu)	
			lower limit	upper limit
80	135 ± 3	100 ± 10	30	45
100	128 ± 3	90 ± 10	30	45
167	130 ± 3	60 ± 10	40	60

alpha bombardment a deviation from compound nucleus center-of-mass motion is observed. This can be due to either a contribution from fission following incomplete momentum transfer or to pre-equilibrium particle emission. The limits on the value for the width of the mass distribution agree with previous measurements (Pla 66). Due to the insensitivity of the track length distributions from gold fission fragments to the width of their mass distribution, any broadening of this width with increasing excitation energy lies outside the deduction capabilities of this analysis.

4.2.2 80-MeV alpha-particles on silver and tellurium.

In the case of the lighter silver and tellurium targets the shape of the mass distribution can no longer be treated as an independent variable. Although the overall shape of the track length distribution is relatively insensitive to the width of the fragment mass distribution, the average track length does show a small variation with this parameter. In principle then one would have to fit the set of track length distributions as a function of the angle of observation, to similar calculated set of distributions. In practice the track length distributions were first calculated for a forward and backward angle of observation and the total kinetic energy release and center-of-mass motion were adjusted and the width of the mass distribution varied so as to obtain the best possible agreement with the experimental data . In figure 4.14 the measured track length distributions from the 80-MeV alpha particle bombardment of silver at laboratory angles of observation of 67.5 and 162.5 degrees are compared with the calculated distributions assuming a total kinetic energy release value of 80 MeV and center-of-mass motion corresponding to compound nucleus formation. The calculated curves labelled 1, 2, 3 and 4 represent an assumed Gaussian mass distribution width of 15, 30, 60 and 500 amu. The calculated distributions show a pronounced peak at high track length values with a gradual "tailing off" towards lower values. The experimental

figure 4.14

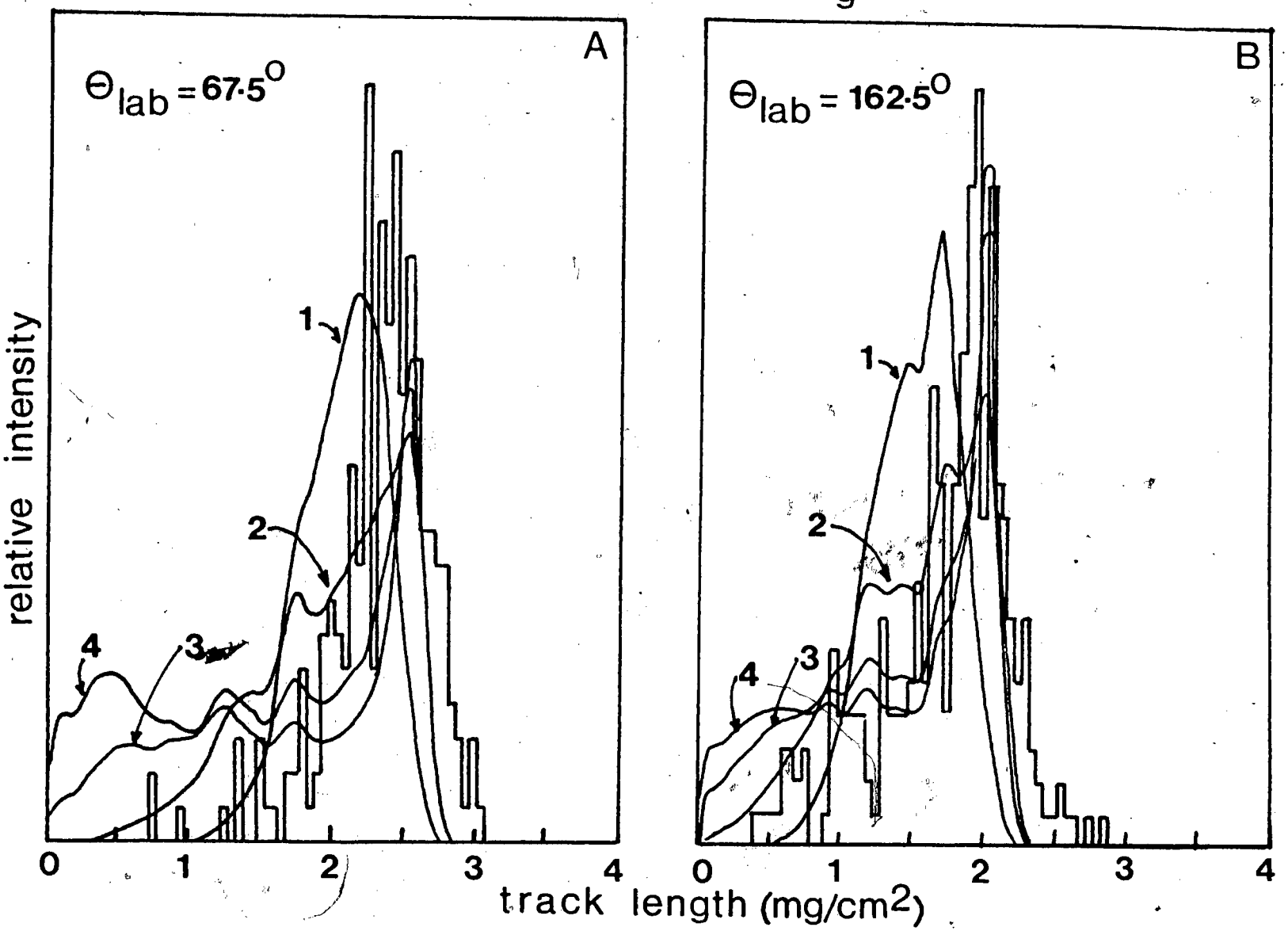
80 MeV α's + Ag
A
$\Theta_{lab} = 67.5^{O}$
B
$\Theta_{lab} = 162.5^{O}$
1
2
3
4
relative intensity
0
1
2
3
4
track length (mg/cm2)

data show a similar trend. By increasing the total kinetic energy release by another 10 MeV, a "fit" can be obtained with the calculated curve assuming the narrow mass distribution of 15 amu full width at half maximum. The pronounced tailing of the track length distributions towards lower values can not be explained, however, in that case. By examining all track length distributions, the lower limit of the full width at half maximum of the mass distribution was set at 30 amu, with an upper limit of 50 amu. To obtain a more precise estimate of the total kinetic energy release and center-of-mass motion, the measured most probable track length was compared with calculated values as is shown infigure 4.15. This quantity is insensitive to the width of the mass distribution for values greater than 30 amu. The best agreement is obtained for a total kinetic energy release of (81±3) MeV and a center-of-mass motion of 70% of the value which would be obtained in the case of compound nucleus formation, although center-of-mass values of 60 to 100% still give acceptable fits.

Figure 4.16 shows a comparison of measured and calculated track length distributions for the tellurium data, similar to the one for the silver data in figure 4.14. Because of the poor statistical accuracy of the tellurium fission fragment track length distributions, the data were combined over ten degree intervals. Shown are the distributions at mean laboratory angles of 60 and 120 degrees. The experimental data again

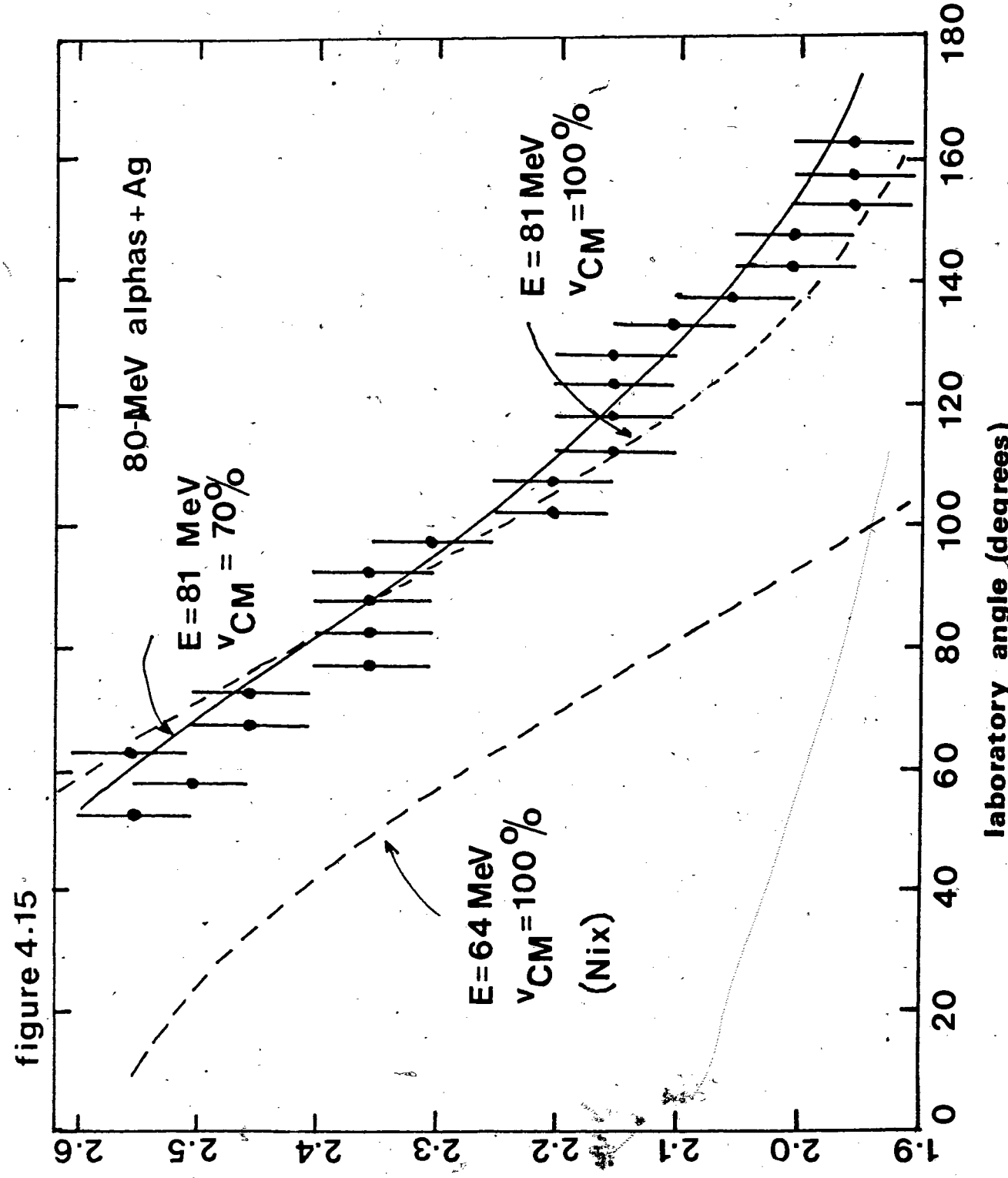
80-MeV alphas + Ag
E=81 MeV
v_{CM} = 70%
E=81 MeV
v_{CM}=100%
E=64 MeV
v_{CM}=100%
(Nix)
most probable track length mg/cm^2
laboratory angle (degrees)
1.9
2.0
2.1
2.2
2.3
2.4
2.5
2.6
0
20
40
60
80
100
120
140
160
180

figure 4.15

show a "tailing off" towards lower track length values, but there is no longer a well defined peak in the distributions. The calculated curves do not fit the experimental distributions as well as in the case of the silver data. Again it was found that very narrow distributions (such as the one shown with a full width at half maximum of 20 amu) do not agree with the general trend of the data. Broader mass distributions show more "tailing" towards lower track length values than is observed experimentally. In section 4.1 it was shown that it was just for this area of total fissioning system mass that a pronounced broadening of the track length distributions would occur (see figures 4.1, 4.2 and 4.6). This broadening effect was due to a "bunching up" of track length versus energy values around certain mass values. If this bunching effect is even a little less pronounced than expected from the interpolation of the calibration data, it would alter the shape of the calculated distributions enough to give a better agreement with the experimental data. Nevertheless a definite amount of broadening of the track length distributions with respect to those of the silver data is present and supports the general statements made in section 4.1 about the "abnormal" behaviour of fragment track length distributions from the fission of nuclei with a mass near 130-140 amu. From the data presented in figure 4.16 it is clear that only a lower limit can be set on the width of the mass distribution of the fission fragments. From an

figure 4.16

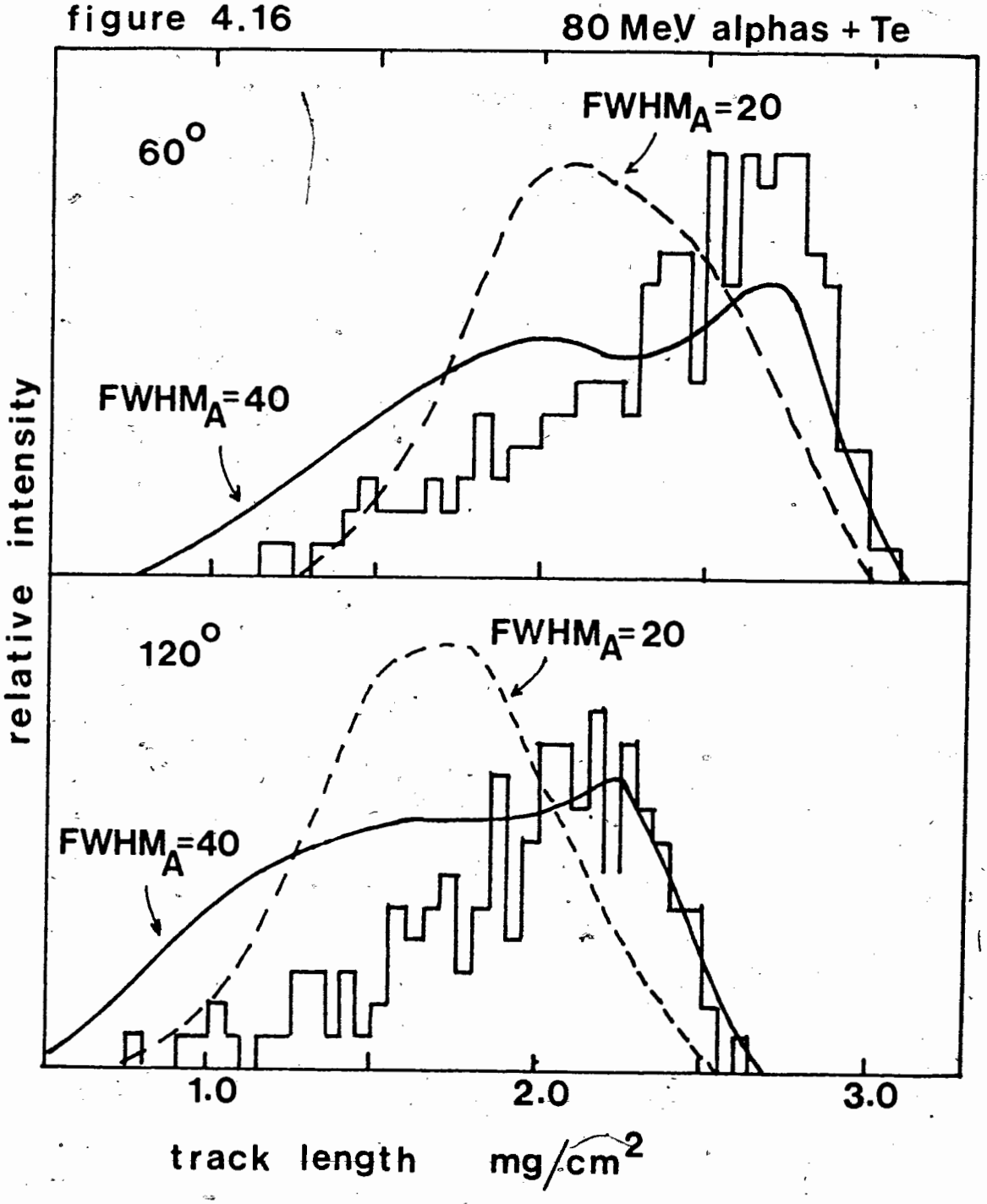
80 MeV alphas + Te
60°
FWHM$_A$=20
FWHM$_A$=40
120°
FWHM$_A$=20
FWHM$_A$=40
relative intensity
1.0
2.0
3.0
track length mg/cm^2

examination of all available track length distribution data, this limit was set at 30 amu.

An estimate of the total kinetic energy release as well as center-of-mass motion was obtained by "fitting" all track length distributions simultaneously to calculated distributions which assume a full width at half maximum of the fragment mass distribution of 40 amu. An experimental and calculated track length distribution were assumed to "fit" each other when good agreement was obtained at higher track values (of the quality of the solid lines shown in figure 4.16). This procedure yields values of (95±5) MeV and (90±10)% for the total kinetic energy release and center of mass motion respectively.

4.2.3 167-MeV alpha-particles on indium and molybdenum.

The data presented in figures 3.3 and 3.4 show that at forward angles of observation (with respect to the beam direction), the track length distributions are partly obscured by the very intense flux of scattered target nuclei. Hence, only the track length distributions at backward angles are compared in figures 4.17 and 4.18 with calculated track length distributions. In these calculations the width of the gaussian mass distribution was varied from 20 to 1,000 amu, while the total kinetic energy release was chosen as 85 and 70 MeV for the indium and molybdenum data respectively. In

figure 4.17 167 MeV alphas + In

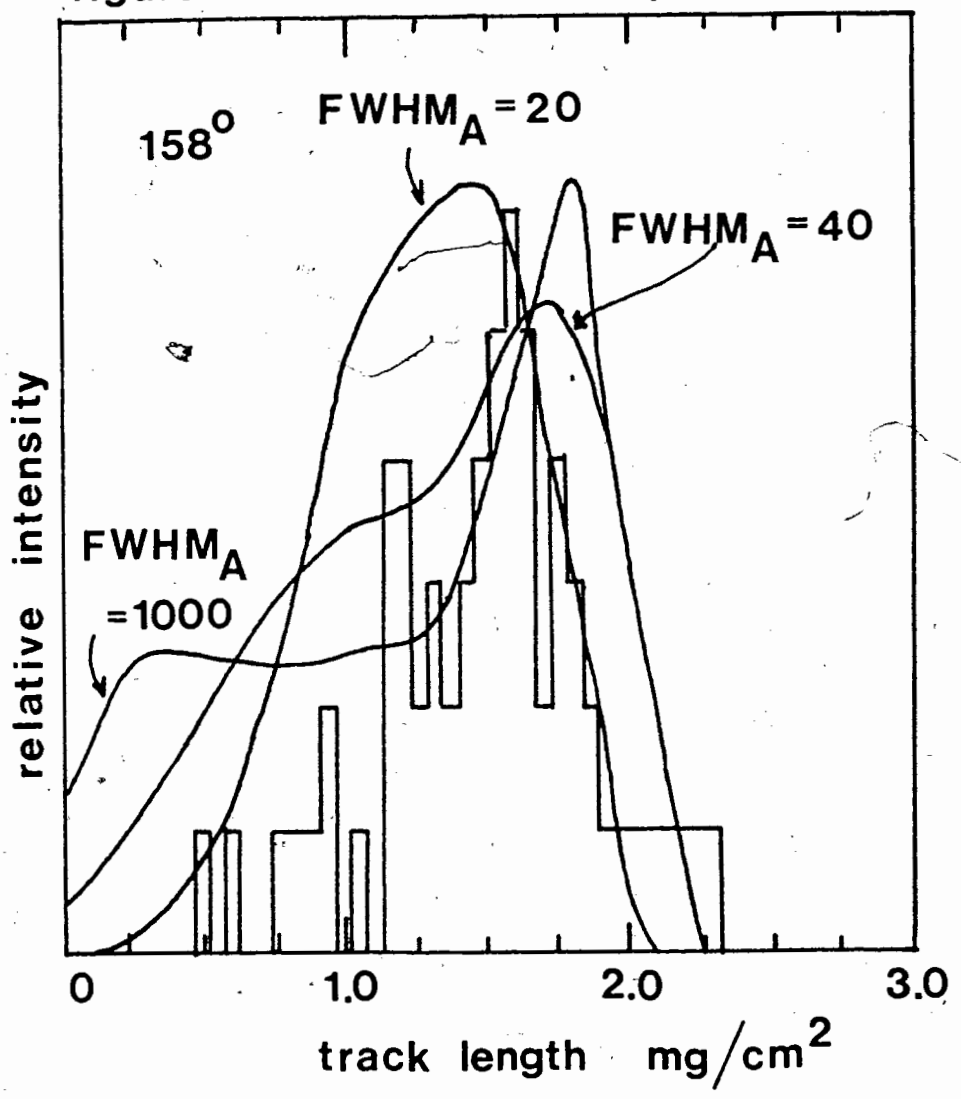

figure 4.18 167 MeV alphas + Mo

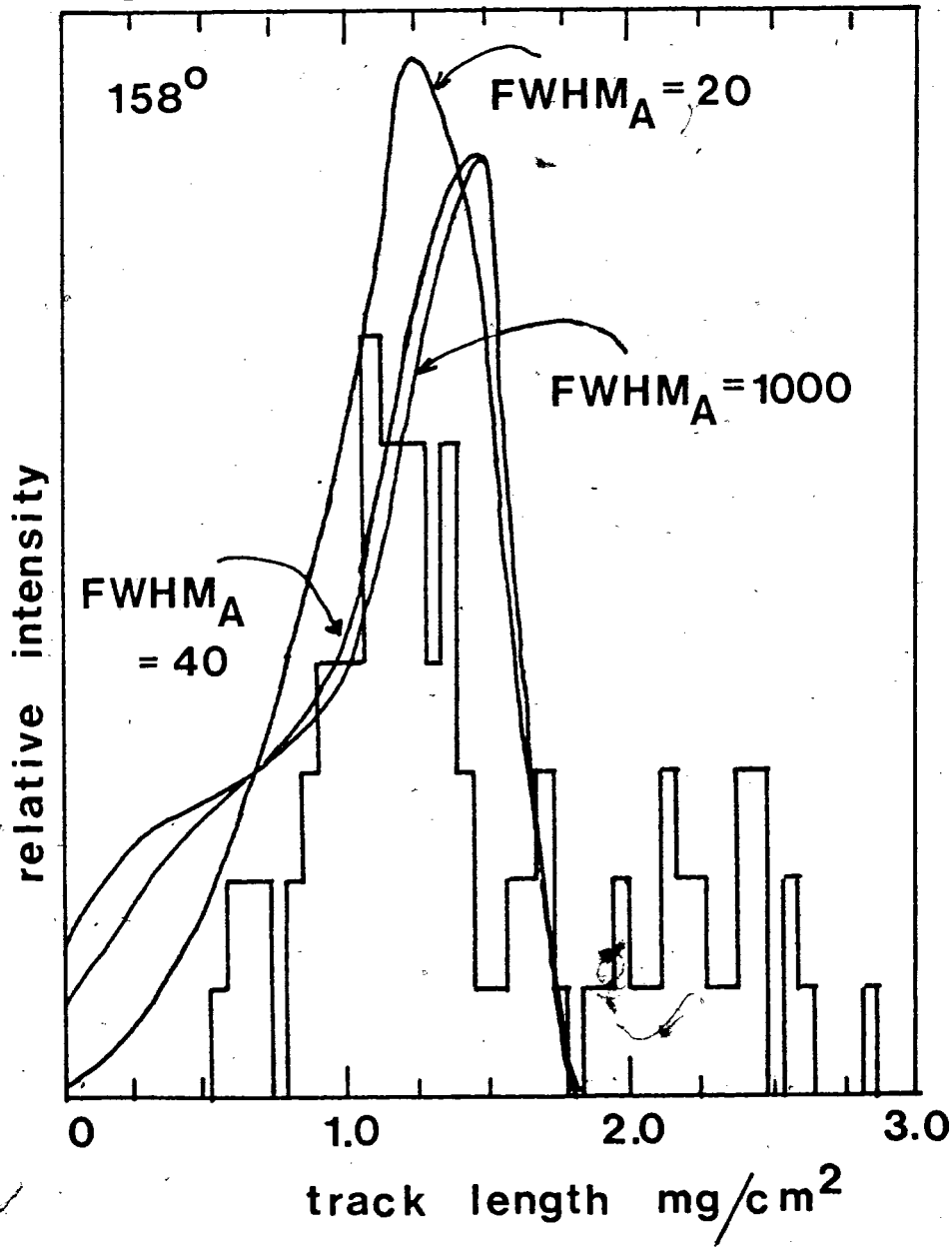

each case the center-of-mass motion was taken to be 60% of the value which would be obtained in the case of full momentum transfer (compound nucleus). These values of the total kinetic energy release were obtained under the assumption that one can extrapolate the results obtained from the silver and tellurium data, while the value for the center-of-mass motion was taken to be the same as for the 167-MeV alpha particle bombardment of gold.

The indium data (figure 4.17) show a moderate agreement with the calculated track length distributions, but the molybdenum data cannot be fitted to the calculated curves even if one takes into account the good possibility that the chosen values for the total kinetic energy release and center of mass motion could be wrong by as much as a factor of two. Contrary to all other results obtained in this work, the molybdenum data show a systematic tailing towards higher track length values. Such an effect cannot be obtained for the calculated track length distributions, no matter how the free parameters are varied. Since the calculated track length distributions agree fairly well with the main peak in the experimental distribution (see figure 4.18), it is reasonable to assume that the tracks with a much longer length originate from fission fragments from heavier nuclei in the target material.

Unfortumately the poor statistical accuracy of these data

does not allow such a separation at all but very backward angles of observation, hence a more precise determination of the total kinetic energy release and center-of-mass motion, along the lines described in the previous sections was not possible. It is only possible to say that the values chosen for the total kinetic energy release and center-of-mass motion from the extrapolation of the results obtained from the other bombardments, are consistent with the experimental results shown in figures 4.17 and 4.18. The poor statistical accuracy of the data also prevents one from establishing limits on the width of mass distribution of the fission fragments.

4.3 Total kinetic energy release in the fission process of medium mass nuclei.

In table IV.2 the values for the total kinetic energy release obtained from the analysis of the variation of the track length distributions with the angle of observation are summarized. Not included are the results for the 167-MeV alpha particle bombardments of indium and molybdenum for the reasons explained in section 4.2.3. For comparison the results from the calculations due to Nix (Nix 69) are given in column 3. Although the results for the gold bombardments agree well with the theoretical prediction, for the lighter nuclei the experimental values are about 20% higher than the theoretical estimates. It is possible that the theory under-estimates the total kinetic energy release of these

Table IV.2 Total kinetic energy release values.

system studied	total kinetic energy release (experimental)	total kinetic energy release (theoretical)
80-MeVα's+Au	135 ± 3	
100-MeVα's+Au	128 ± 3	129
167-MeVα's+Au	130 ± 3	
80-MeVα's+Te	95 ± 5	73
80-MeVα's+Ag	81 ± 3	64

lighter nuclei by such a large percentage but the discrepancy is more likely the result from the "touching sphere approximation" used in the analysis of the experimental data. In section 4.1 it was shown that for nuclei in the region of silver and tellurium, the most probable track length is no longer determined by the track length of the most probable fission fragments (i.e. the fragments from a symmetric fission event). Instead the most probable track length is built up by the contributions of many asymmetric fission events. In the fitting procedure described in sections 4.1 and 4.2, the value that is entered for the total kinetic energy will be higher in the case that the energy release decreases rapidly with increasing asymmetry of the fission fragments, (as is the case when the touching sphere approximation is used) than when the energy release varies more slowly with the mass of the fission fragments (as has been observed experimentally by

Plasil et al (Pla 66). Hence the values for the total kinetic energy release listed in table IV.2 can only be treated as upper limits.

Chapter 5 Analysis of angular distribution data.

As well as for the determination of differential and total cross sections, angular distributions of fission fragments can be used to extract information as to the shape of the fissioning nucleus at the moment of scission. Usually the angular distribution shows a certain amount of anisotropy (commonly expressed in terms of the ratio of the differential cross sections at 180° and 90°), and some reasonable assumptions have to be made about the functional form of an equation which can be used to fit the available experimental differential cross section data if extrapolation is necessary into inaccessible areas of differential cross-section measurement (i.e. at angles of observation of 0 and 180°).

Although Legendre polynomial expansions have often been used (Cof 58, Nic 62, Cha 62, Bat 63, Rei 66, Lec 71), such a functional form has no other meaning than to provide one with an acceptable representation of the shape of angular distributions. A more meaningful description can be obtained by linking the probability of emitting a fragment into a given angle to the distribution with respect to angular momentum of the energy levels of the nucleus at the saddle point.

5.1 Theory of fission fragment angular distributions.

For medium mass fissioning nuclei at moderate excitation energies, the statistical model can be used to describe the energy levels

in the transition nucleus (nucleus at the saddle point shape). The K distribution (where K is the projection of the total angular momentum I on the nuclear symmetry axis) of the levels in the transition nucleus for a given temperature is predicted to be Gaussian (Hal 55, Hui 69),

$$F(K) \propto \exp(-K^2/2K_0^2) \qquad 5.1$$

and the variance of the K distribution (designated as K_0^2) is:

$$K_0^2 = \tau_{eff} t/\hbar^2 \qquad 5.2$$

Here t is the temperature of the nucleus at the saddle point and τ_{eff} is the effective moment of inertia equal to

$$\tau_{eff} = \tau_\perp \tau_\parallel / (\tau_\perp - \tau_\parallel) \qquad 5.3$$

where $\tau_\perp$ and $\tau_\parallel$ are nuclear moments of inertia with respect to axes perpendicular and parallel to the symmetry axis, respectively. Wheeler has shown that (under the assumption that the fission fragments separate along the nuclear symmetry axis) the fission-fragment angular distribution for a transition state with quantum numbers I, K and M (projection of I on a space fixed axis which is usually taken as the beam direction) is given by (Whe 63)

$$W_{M,K}^{I}(\theta) = \{(2I + 1)/4\pi\} |d_{M,K}^{I}(\theta)|^2 \qquad 5.4$$

where the $d_{M,K}^{I}(\theta)$ functions are defined by (Lam 62):

$$d_{M,K}^{I}(\theta) = \{(I+M)!\ (I-M)!\ (I+K)!\ (I-K)!\}^{\frac{1}{2}} \sum_{X} \frac{(-1)^{X}(\sin\frac{1}{2}\theta)^{K-M+2X}(\cos\frac{1}{2}\theta)^{2I-K+M-2X}}{(I-K-X)!\ (I+M-X)!\ (X+K-M)!\ X!} \qquad 5.5$$

where the sum is over X=0,1,2,3,--- and contains all terms in which no negative value appears in the denominator of the sum for any one of the quantities in parenthesis. Recently, tables of the rotational wave functions $d_{M,K}^{I}(\theta)$ have been published for a range of I,M, and K values (Beh 71).

An exact equation for the fission fragment angular distribution, including the effects of target and projectile spin and assuming a Gaussian K distribution has been derived by Griffin (Gri 63):

$$W(\theta) \propto \sum_{I=0}^{\infty} \sum_{M=-j_{max}}^{j_{max}} \left[\sum_{\ell=0}^{\infty} \sum_{j=|I_0-s|}^{I_0+s} \sum_{\mu=-I_0}^{I_0} \left\{ \frac{(2\ell+1)T_\ell\ |C_{M,0,M}^{j,L,I}|^2 |C_{\mu,M-\mu,M}^{I_0,s,j}|^2}{\sum_{l=0}^{\infty}(2\ell+1)\ T_\ell} \right\} \right] \qquad 5.6$$

$$x \sum_{K=-I}^{I} \left[(2I+1)\ |d_{M,K}^{I}(\theta)|^2 \exp\left(\frac{-K^2}{2K_0^2}\right) \Big/ \sum_{K=-I}^{I} \exp\left(\frac{-K^2}{2K_0^2}\right) \right]$$

Here I_0, s and j are the target spin, projectile spin and channel spin respectively. The channel spin j is defined by $\vec{j} = \vec{I}_0 + \vec{s}$. The total angular momentum I is given by the sum of the channel spin and the orbital angular momentum $\vec{I} = \vec{j} + \vec{\ell}$ The projection of I_0 on the space-fixed axis is given by μ, where the projection of j (and I) on the space-fixed axis is M. The $d_{M,K}^{I}(\theta)$ function was defined above and the quantities $C^{j,L,I}_{M,0,M}$ and $C^{I_0,s,j}_{\mu,M-\mu,M}$ are Clebsch-Gordan coefficients. This expression can be simplified in the case that the target and projectile spin are zero the overall distribution then becomes (Van 73, Hui 69)

$$W(\theta) \propto \sum_{I=0}^{\infty} (2I+1) T_I \sum_{K=-I}^{I} \frac{(2I+1) \left| d_{M=0,K}^{I}(\theta) \right|^2 \exp(-K^2/2K_0^2)}{\sum_{K=-I}^{I} \exp(-K^2/2K_0^2)} \qquad 5.7$$

where the transmission coefficients are written as T_I since $\ell=I$ when M=0. This equation is still an exact equation for the case in question but when the orbital angular momentum is large as compared to the target and/or projectile spin, the projection of the orbital momentum on the space fixed axis is usually small and the above equation can also be used as a good approximation. Also, for large values of I the $d_{M,K}^{I}(\theta)$ function may be approximated by (Whe 63)

$$d_{M,K}{}^{I}(\theta) \simeq \pi^{-1}\{(I+\tfrac{1}{2})^2\sin^{-2}\theta - M^2 - K^2 + 2MK\cos\theta\}^{-\frac{1}{2}}$$

which in the M=0 approximation simplifies to

$$d_{M=0,K}{}^{I}(\theta) \simeq \pi^{-1}\{(I+\tfrac{1}{2})^2\sin^2\theta - K^2\}^{-\frac{1}{2}} \qquad 5.8$$

Substituting this expression in the above equation for $W(\theta)$, and replacing the summation with integrals, Huizenga et al (Hui 69) derived an overall fission fragment angular distribution in the M=0 approximation

$$W(\theta) \propto \sum_{I=0}^{\infty} \frac{(2I+1)^2 T_I \exp\{-1(I+\tfrac{1}{2})^2\sin^2\theta/4K_0{}^2\} J_0\{i(I+\tfrac{1}{2})^2\sin^2\theta/4K_0{}^2\}}{\text{erf}\ \{(I+\tfrac{1}{2})/(2K_0{}^2)^{\frac{1}{2}}\}} \qquad 5.9$$

Where J_0 is the zero-order Bessel function with an imaginary argument and erf is the error function defined by

$$\text{erf}(x) = (2/\sqrt{\pi}) \int_0^x e^{-t^2} dt \qquad 5.10$$

In applying this angular distribution equation to the fitting of experimental data care has to be taken that the experimental conditions do not contradict any of the approximations used in the derivation of this equation. One of the most important approximations is that compound nucleus formation is assumed to precede any fission event. In that case the nuclear temperature is well defined and the proper weighting over the I distribution ($(2I+1)T_I$) can be carried out. Furthermore it is usually assumed that competition between particle emission and fission of the

compound nucleus with the subsequent contribution from second and higher chance fission (fission of nuclei that have already evaporated one or more particles) does not alter the distribution in angular momentum of all fissioning nuclei. In chapter 4 it was shown that the 80 and, with some reservation, the 100 and 120 MeV alpha particle bombardments give rise to complete momentum transfer for the targets considered in this work (i.e. compound nucleus formation did precede fission), but results of the 167 MeV alpha particle experiments showed a significant deviation from full momentum transfer. Application of this theory of angular distributions is, therefore, restricted to the lower energy data. Whether the distribution in angular momentum (and temperature) of those nuclei that fission is altered significantly by the prior emission of particles in the de-excitation of the compound nucleus is examined in the following section.

5.2 Competition between particle evaporation and fission in the de-excitation of the compound nucleus.

5.2.1 Particle evaporation.

The concept of rapid sharing of the energy of an incoming particle by the nucleons of the target nucleus to form a "compound" nucleus, and the subsequent decay of this nucleus by particle evaporation has been discussed as early as the mid thirties by Bohr (Boh 36) and Breit and Wigner (Bre 36). The statistical

model was used to describe the evaporation of particles from the nucleus in analogy with the evaporation of molecules from a liquid drop (Bet 37, Wei 37, Wei 40). Inclusion of angular momentum effects lead to the familiar equation describing the transition of a particle from one state to another (Tho 64, Rud 68):

$$P(E_F,I_F;E_cI_c)d\varepsilon = \frac{(2S_x+1)}{\pi^2h^3}\,\varepsilon\mu\sigma(\varepsilon,I_c,I_F)\,\frac{\omega(E_F,I_F)}{\omega(E_c,I_c)}\,d\varepsilon \qquad 5.11$$

Here E_F and I_F are the energy and angular momentum of the final state, E_c and I_c the energy and angular momentum of the initial state. ε is the energy carried away by particle x, s_x is the spin and μ is the reduced mass of particle x. $\sigma(\varepsilon,I_c,I_F)$ is the inverse reaction cross section, which, using an intermediate coupling approach to the angular momenta involved (Pre 63), can be expressed by

$$\sigma(\varepsilon,I_c,I_F) = \frac{\pi\lambda\!\!\!^{-2}(2I_c+1)}{(2s_x+1)(2I_F+1)} \sum_{S=|I_F-s_x|}^{I_F+s_x} \sum_{\ell=|I_c-S|}^{I_c+S} T_\ell(\varepsilon) \qquad 5.12$$

Where $\lambda\!\!\!^{-}$ is the reduced DeBroglie wave length of the system. In most cases the s-wave approximation is applied, which means that angular momentum effects are treated identically in compound and residual states (i.e. the angular momentum carried away by evaporating particles is neglected) reducing $\sigma(\varepsilon,I_c,I_F)$ to $\sigma(\varepsilon,I)$

(Bla 66, Bla 72, Bla 73). The $\omega(E,I)$ functions represent the level density of the nucleus for given energy E and angular momentum I. Neglecting the angular momentum dependence, the simplest expression for an energy dependent level density is the so-called Fermi gas equation

$$\omega(E) \propto \exp\{2(aE)^{\frac{1}{2}}\} \qquad 5.13$$

Inclusion of angular momentum effects has been attempted by many authors (Sar 67, Bod 62, Lan 63), but not until superconductor theory was applied to include the interaction between nucleons (Fermi gas model does not allow this) was a physically satisfactory expression obtained. For nuclear temperatures up to a certain critical value t_c at which all nucleon-nucleon pairs are broken, the moment of inertia of the nucleus is expected to increase with increasing energy, thereby changing the rotational energy of the nucleus (Bel 59, Mig 59, Lan 63b). Above the critical temperature the Fermi gas model is thought to be applicable. The angular momentum-dependent level density can be written as (Rud 68)

$$\omega(E,I) = \frac{\sqrt{2}}{48} a^{\frac{1}{2}} \left(\frac{\hbar}{\tau}\right)^{3/2} (E+3/2t)^{-2} (2I+1) \exp\{2(aE)^{\frac{1}{2}} - \frac{\hbar^2 I(I+1)}{2\tau t}\} \qquad 5.14$$

where the temperature t is given by the equation of state (Rud 68)

$$E = at^2 - 3t/2 \qquad 5.15$$

For the variation of the moment of inertia with energy up to the point (usually taken as 15 MeV) at which it assumes the rigid body value, various expressions have been derived. Ruddy et al (Rud 68) have used

$$\tau = \tau_{rigid} \{1-0.96 \exp\left[-0.693E/(3.0\ MeV)\right] \} \qquad 5.16$$

for the Ge^{68} compound nucleus, while Sarantites et al (Sar 71) studied the Ni^{68} nucleus and used

$$\tau = \tau_{rigid} \{1-0.7 \exp\left[-0.693E/(5.0\ MeV)\right] \} \qquad 5.17$$

The only parameter which has not yet been discussed in the above equations is the level density parameter a. The Fermi gas model predicts this parameter to be the following (Bod 62)

$$a = 2\left(\frac{\pi}{3}\right)^{4/3} \frac{m r_0^2}{h^2} A \qquad 5.18$$

where r_0 is the radius parameter and m and A are the mass of the particle and nucleus respectively. Experimental data indicate a value of $a = A/8.0\ MeV^{-1}$ (Lan 61), which corresponds to a radius parameter of $r_0 = 1.15$ f, although data exist indicating a reduced a-value for nuclei having nucleon numbers near those for closed neutron or proton shells (Bod 62). More recently concern has also been expressed about the possibility that the parameter a is energy dependent (Ram 70, Mor 70, Van 72, Wil 72).

5.2.2 Fission width

The average fission width for levels of all spins (neglecting barrier penetration) is given by (Gin 67)

$$\Gamma_f = \frac{1}{2\pi\omega(E)} \int_0^{E-B_f} \omega^*(\varepsilon)d\varepsilon \qquad 5.19$$

Where $\omega(E)$ is the level density in the compound nucleus at excitation energy E and the effective number of open states is given by the integral $\int\omega^*(\varepsilon)d\varepsilon$. The quantity $\omega^*(\varepsilon)$ is the level density in the transition state nucleus at excitation energy ε. The quantity B_f is the fission barrier calculated in the conventional way for a non-rotating nucleus using the liquid drop theory (Mye 66, Fra 47), and neglecting barrier penetration.

Angular momentum effects will not only alter the level density, but also the magnitude of the fission barrier. The energy and shape changes associated with the rotation of a uniformly charged liquid drop model have been explored by Pik-Pickak (Pic 58) and Hiskes (His 60), but only recently have quantitative calculations been described by Cohen et al (Coh 74). The model considers the potential energy for the various configurations of a rotating uniformly-charged drop given by $E=E_S+E_C+E_R$ (Coh 74), where E_S is the surface energy, E_C is the coulomb energy and E_R is the rotational energy. After parameterization of the surface in terms of Legendre polynomials, equilibrium configurations were obtained in terms of two dimensionless parameters x and y, where x is the

fissility parameter and y is a rotational parameter, given by the ratio of the rotational energy of a sphere to its surface energy. Cohen et al (Coh 74) calculated as a function of x and y the values for the energies E_{min} of the stable rotating configurations of equilibrium (lowest energy rotating states) as well as for the energies E_{sp} of the unstable configurations of equilibrium (saddle point shapes). Inclusion of angular momentum effects in equation 5.19 will yield

$$\Gamma_f(J) = \frac{1}{2\pi\omega(E,J)} \int_0^{E-E_{sp}(J)} \omega(E-E_{sp}(J)-\varepsilon)d\varepsilon \qquad 5.20$$

Where we assume that the level density parameter a is the same for both the stable and unstable equilibrium configurations

$\omega(E,J) = \omega^*(E,J)$

When barrier penetration is included in equation 5.20, one obtains (Van 73)

$$\Gamma_f(J) = \frac{1}{2\pi\omega(E,J)} \int_{-\infty}^{E-E_{sp}(J)} \left\{ \frac{\omega^*(E-E_{sp}(J)-\varepsilon)}{1+\exp(-2\pi\varepsilon/\hbar\omega)} \right\} d\varepsilon \qquad 5.21$$

where $\hbar\omega$ is the vibrational energy of the harmonic oscillator having a potential energy function given by the negative of the potential energy function describing the barrier.

5.2.3 Fission and evaporation competition

When sufficient excitation energy is available to the compound nucleus, fission will compete with particle evaporation in the decay of the nucleus. Using the formulation described in sections 5.2.1 and 5.2.2 a computer code was developed which traces the distribution in angular momentum and excitation energy of the compound nucleus while it decays. A similar code has been written by Blann and Plasil (Bla 73), but in their code "ALICE", the angular momentum which is carried away by the evaporating particle is assumed to be zero (due to the use of the s-wave approximation in calculating inverse reaction cross-sections (see section 5.2.1)) however, an option is built into their program which allows one to shift the distribution in angular momentum of the residual nuclei by an amount appropriate to the average angular momentum carried away by the evaporating particle. It is possible to include the effects of angular momentum explicitly by using equations 5.11 and 5.12. Such an approach is important because it is the distribution in angular momentum and excitation energy of all fissioning nuclei that is needed in order to interpret the angular distribution data (see section 5.1).

The computer program described here (and in more detail in Appendix 3) is a combination of the evaporation programs "SFUSMAP" (Rud 68) and "ALICE" (Bla 73) with a number of additional features. Among these latter features are provisions to enter the distri-

butions in angular momentum and excitation energy of any nucleus and follow the decay of this nucleus as far down the evaporation chain as 11 neutrons or 9 protons. Output consists mainly of the distribution in angular momentum and excitation energy of all possible evaporation products and of those nuclei that fission within this 9X12 matrix of nuclei. The initial distribution in angular momentum and excitation energy of the compound nucleus can also be calculated internally from the entrance channel conditions. A complete list of the options that can be used is given in Appendix 3.

The main interest in developing this program was to extract the distribution in angular momentum and the excitation energy of the entire spectrum of fissioning nuclei. As a test case, these distributions were calculated for 80-MeV alpha particles incident on silver. Table V.I shows the evaporation product yields as well well as the proportion of each intermediate product nucleus that underwent fission as a function of the excitation energy E and the angular momentum I. De-excitation via γ emission was not included. Consequently (for example) the residual yield corresponding in composition to the original compound nucleus is zero. The omission of γ-decay competition is not expected to alter the results for fission yields significantly, since γ-decay only becomes prominent when particle evaporation is no longer energetically possible (Rud 68). First chance fission is by far the largest contributor to the total fission cross-section (ratio of

Table V.1 Yield of the evaporation products and fissioning nuclei from the 80-MeV α's + Ag interaction. Z and N indicate the number of protons and neutrons of each nucleus.

Yields of evaporation products (mb):

	Z=49	Z=48	Z=47	Z=46	Z=45	Z=44	Z=43	Z=42
N=63	-	.99e-09	.12e-04	.44e-02	.27e-01	.35e-03	.19e-08	-
N=62	.29e-09	.11e-03	.18e 00	.56e 01	.43e 00	.60e-04	.66e-13	-
N=61	.84e-05	.47e 00	.71e 02	.94e 02	.12e 00	.19e-01	.12e-04	.16e-10
N=60	.13e-01	.80e 02	.88e 03	.18e 03	.39e 01	.14e 00	.24e-05	.60e-16
N=59	.34e 00	.24e 03	.78e 02	.43e 02	.33e 02	.11e 00	.17e-04	.26e-05
N=58	.56e-01	.56e 01	.27e 02	.27e 03	.28e 02	.14e 01	.80e-03	.54e-07
N=57	.44e-04	-	.33e 02	.11e 02	.76e 01	.14e 02	.37e 00	.21e-05
N=56	-	-	.38e-01	.68e-04	.85e 01	.93e 00	.91e-04	.39e-03
N=55	-	-	-	-	.47e-01	.65e-04	.13e-01	.49e-04
N=54	-	-	-	-	-		.76e-03	.14e-08

Fission yields (mb):

	Z=49	Z=48	Z=47	Z=46	Z=45	Z=44	Z=43	Z=42
N=63	.78e-03	.41e-05	.12e-09	-	-	-	-	-
N=62	.11e-04	.52e-07	.12e-15	-	-	-	-	-
N=61	.96e-08	.23e-13	.29e-06	.24e-11	-	-	-	-
N=60	-	-	.15e-08	-	-	-	-	-
N=59	-	-	-	-	.26e-13	-	-	-
N=58	-	-	-	-	-	-	-	-
N=57	-	-	-	-	-	-	-	-
N=56	-	-	-	-	-	-	-	-
N=55	-	-	-	-	-	-	-	-
n=54	-	-	-	-	-	-	-	-

first chance fission to the total cross-section (R_1 = 0.956), which is expected because of the magnitude of the fission barrier (≈50 MeV) with respect to the excitation energy (≈80 MeV) and the consequently rapid decrease of the fission width as this energy is reduced by evaporation. The distribution in angular momentum and excitation energy is, therefore, governed by the first chance fission distribution. Results for 80-MeV alpha particles incident of Te are expected to be similar.

When this calculation is repeated for the 80-MeV alpha particle bombardment of gold, the results are quite different. Table V.2 shows the total number of nuclei that fission from each intermediate evaporation product. The de-excitation of the system was only followed until two protons were evaporated, because the

Table V.2 Calculated yield of fissioning nuclei (in mb) from the 80-MeV α's + Au interaction. Z and N indicate the number of protons and neutrons of each fissioning nucleus.

	Z=81	Z=80
N=120	0.20×10^{-1}	0.14×10^{-4}
N=119	0.42×10^{-1}	0.27×10^{-4}
N=118	0.86×10^{-1}	0.43×10^{-4}
N=117	0.16×10^{0}	0.18×10^{-4}
N=116	0.21×10^{0}	0.94×10^{-6}
N=115	0.14×10^{1}	0.20×10^{-8}
N=114	0.82×10^{-1}	-
N=113	0.45×10^{-5}	-

fission cross section drops off very sharply as Z^2/A is reduced, and thus is a sharp function of the nuclear proton number. For this system the ratio $R_1 = 0.010$, which means that first chance fission only contributes 1% to the total fission cross-section. The increase of the fission cross-section with increasing number of evaporated neutrons is similar to the result obtained by Lecerf (Lec 71) using a different and rather crude model for the de-excitation of the compound nucleus. The distribution in angular momentum of these fissioning nuclei is shown in figure 5.1. Here the distribution for nuclei undergoing first chance fission is compared with that for all fissioning nuclei. (Note that the scales for the curves are not the same.) The widely used assumption that the shape of the distribution does not change when multiple chance fission is included is not substantiated by these results. Figure 5.2 gives the excitation energy distribution of the fissioning nuclei. The shaded area is the contribution from first chance fission, while the overall excitation energy distribution shows a mean value of around 28 MeV. Indeed the system is so sharply peaked that the assumption that all the nuclei fissioning in this system did so at an excitation energy corresponding to this value is a good one. The absolute magnitude of this value, depends on the value of the fission barrier used. In the above calculations, the liquid drop values were used without shell corrections. In the case of gold, the shell correction is important and inclusion of this effect in the

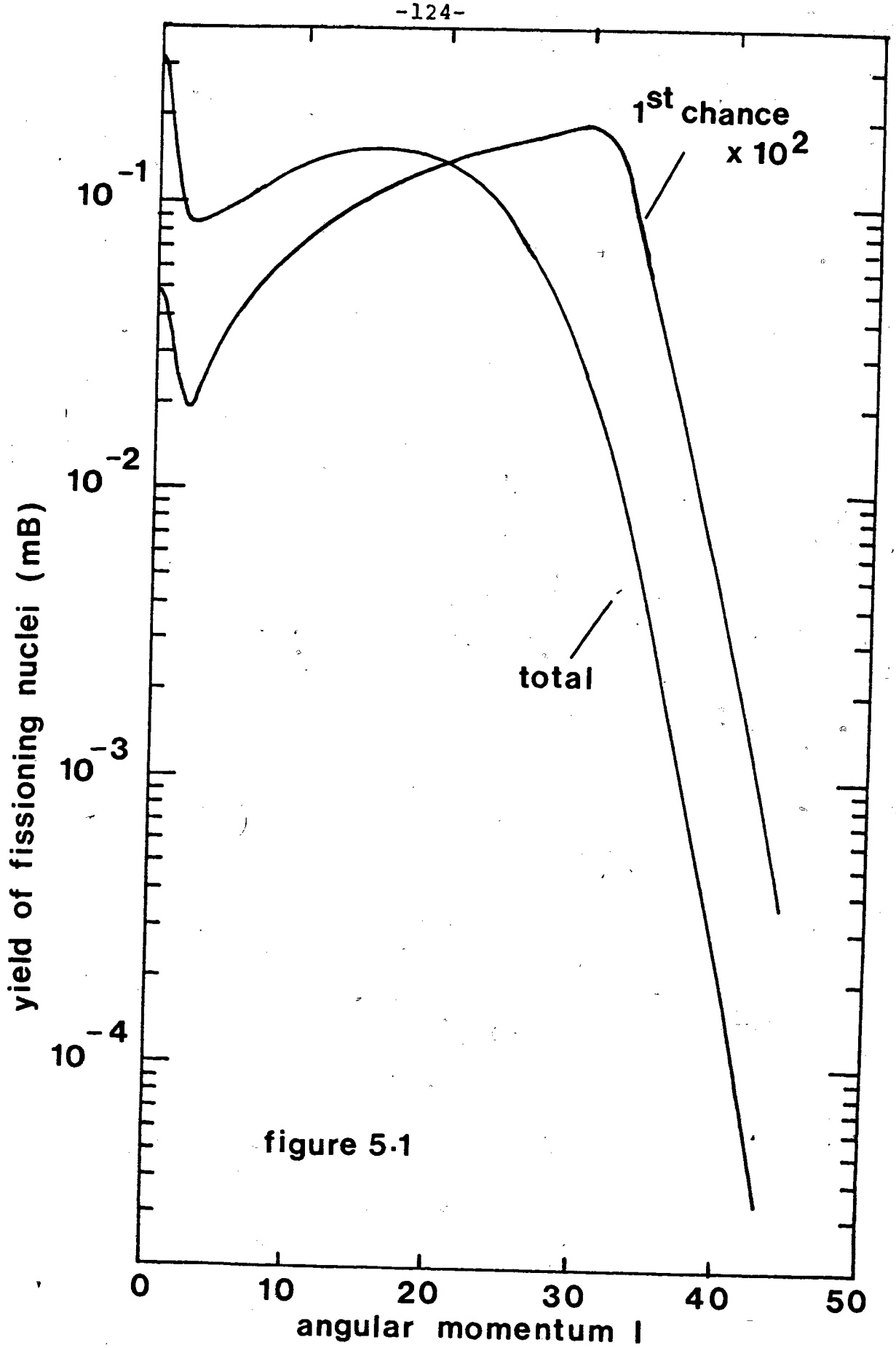
1st chance
x 10^2
total
yield of fissioning nuclei (mB)
10^-1
10^-2
10^-3
10^-4
0
10
20
30
40
50
angular momentum l

figure 5.1

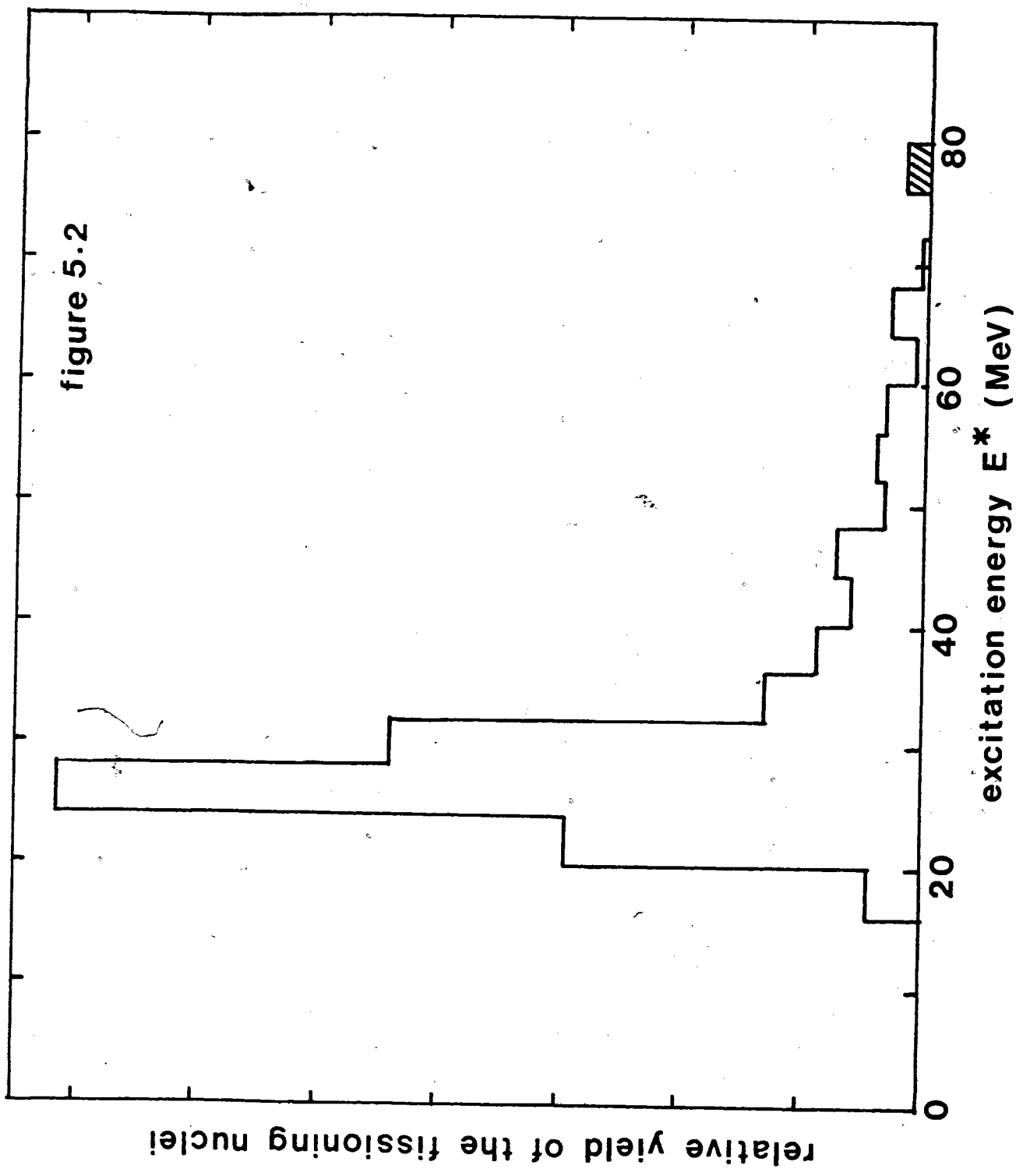
relative yield of the fissioning nuclei
0
20
40
60
80
excitation energy E* (MeV)

figure 5.2

calculations would shift the mean excitation energy by about 5 MeV to approximately 33 MeV.

5.3 Application to the analysis of angular distributions

Equation 5.9 (see section 5.1) can only be applied when the fission fragments originate from compound nucleus (first chance fission), since in the derivation of this equation the I distribution is weighted by a $(2I+1)T_I$ factor characteristic of the compound nucleus angular momentum distribution. Of the experimental data available in this work, only the 80-MeV alpha particle bombardments of silver and tellurium satisfy this requirement. Using a computer program "KNOTTY", obtained through Dr. J.B. Natowitz (TAMVEC), the angular distributions from these two experiments were fitted to equation 5.9. T_I values were calculated using the optical model code "DWUCK" (courtesy of Dr. J. Grabowski, S.F.U.), using standard optical model parameters for alpha particles (Igo 59). Figures 5.3 and 5.4 show the quality of these fits. K_0^2 values deduced from these fits are 34.6 ± 3.8 and 37.4 ± 8.3 for Ag and Te respectively, calculated under the assumption of compound nucleus formation in all entrance channels.

For reactions of heavy ions (such as ^{16}O for example) occurring at energies well above that corresponding to the coulomb barrier, the possible existence of a centrifugal limitation to complete fusion of target and projectile has recently been discussed by

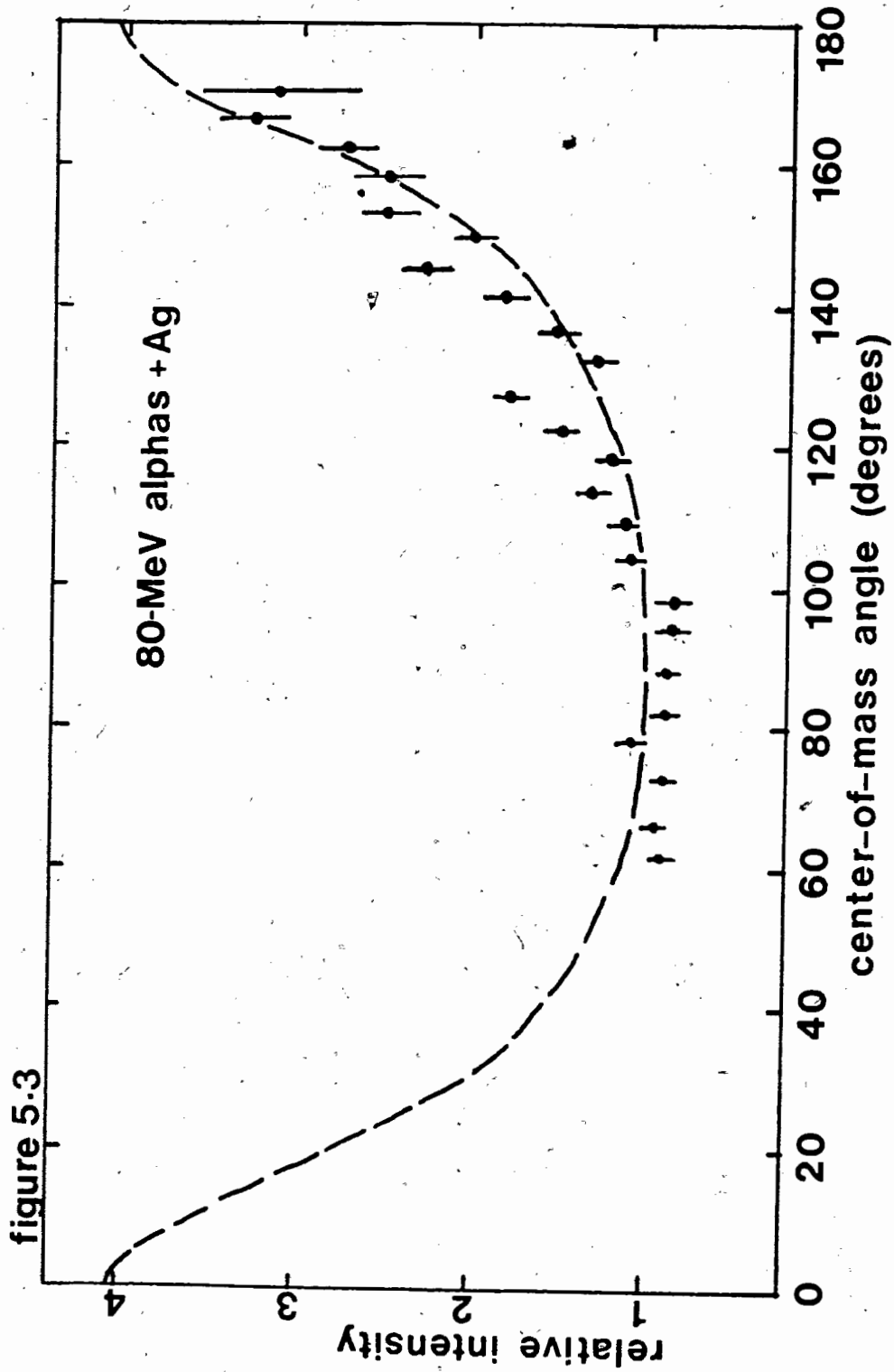
80-MeV alphas + Ag
relative intensity
center-of-mass angle (degrees)
0
20
40
60
80
100
120
140
160
180
1
2
3
4

figure 5.3

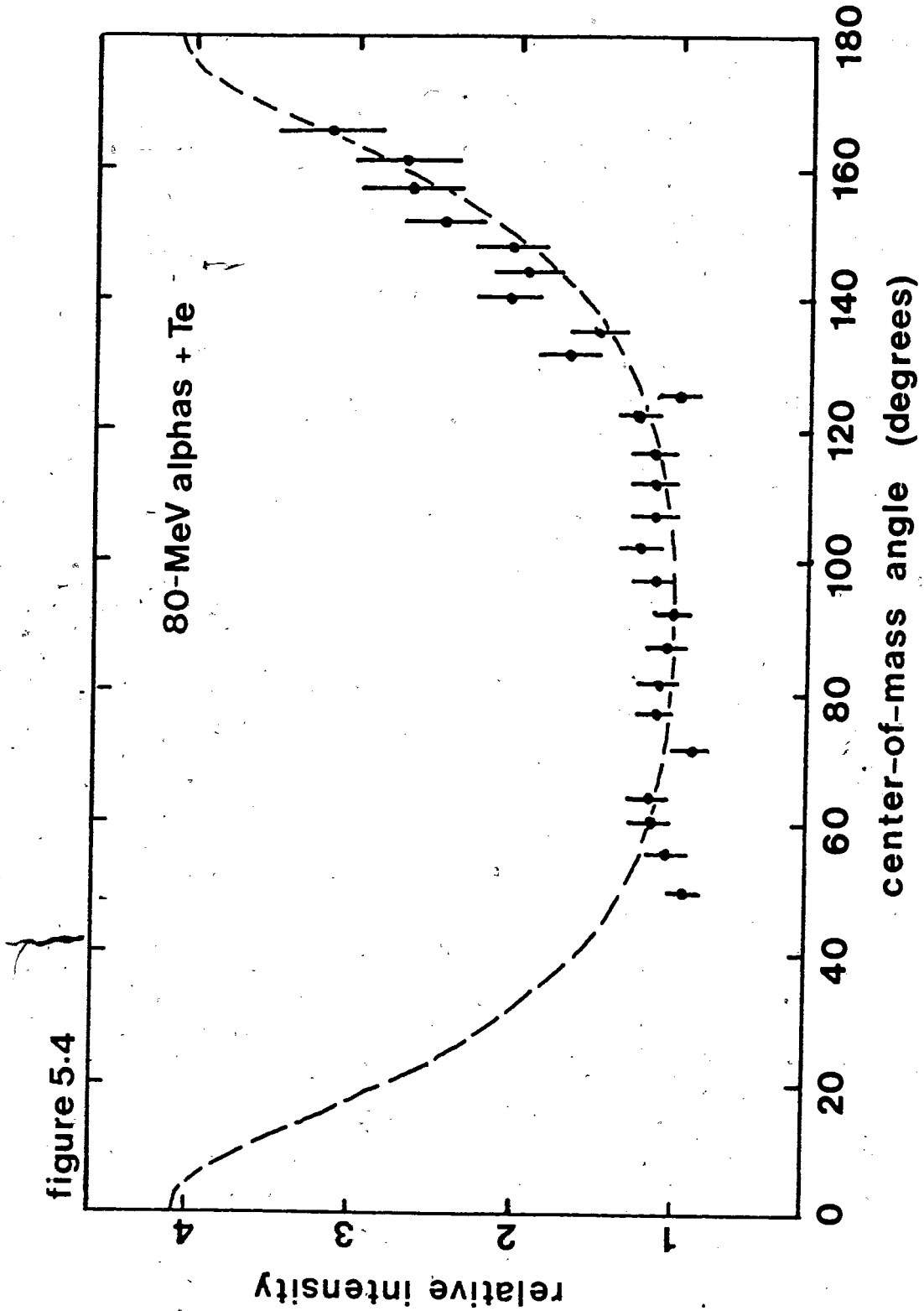
80-MeV alphas + Te
relative intensity
center-of-mass angle (degrees)
0
20
40
60
80
100
120
140
160
180
1
2
3
4

figure 5.4

a number of authors (Wil 73, Bas 73, Nat 72, Nat 70, Zeb 74). Wilczynski (Wil 73) has proposed a model which applies to dynamic force equilibrium between two touching spherical liquid drops in the entrance channel to determine critical maximum angular momenta and hence complete fusion cross sections. This particular model has been shown to apply to some alpha particle induced reactions (Vio 74), and thus was given some consideration here.

In the Wilczynski model the attractive nuclear force between two spherical, charged liquid drops in contact is approximated by the surface energy of the two drops. The critical angular momentum is thus determined at the point where the surface tension force is just balanced by Coulomb and centrifugal repulsion. (Wil 73, Vio 74). Thus l_c can be evaluated from the expression (Wil 73)

$$2\pi(\gamma_1 + \gamma_2)\, R_1R_2 = \frac{Z_1Z_2e^2}{(R_1+R_2)} + \frac{\hbar^2 l_c(l_c+1)}{\mu(R_1+R_2)^2} \qquad 5.22$$

where the nuclear radii are given by $R_i=r_0A_i^{1/3}$, Z_i represents the nuclear charge and μ represents the reduced mass of the system and the other terms are as defined earlier except γ_i which represents the liquid drop surface tension coefficient:

$$\gamma_i = \frac{a_s\left\langle 1-\kappa((N-Z)/A)^2\right\rangle}{4\pi r_o^2} \qquad 5.23$$

where a_s and κ are the surface energy and surface asymmetry terms from the semi-empirical mass equation. Values of a_s = 17.9439 MeV and κ = 1.7826 are used in most calculations (Vio 74). Using a value of r_o=1.10 f and an alpha particle radius of R_α = 2.08 f (Hof 56) the critical angular momenta were calculated for the Ag, Te and Au target plus alpha systems Table V.3 summarizes these results.

Table V.3 Critical angular momenta calculated using the Wilczynski model (Wil 73) using a r_0 value of 1.10f

interaction	critical l
α + Ag	26
α + Te	28
α + Au	33

If one adopts the simplest - but most severe - procedure and treats these critical l values as a sharp cut off, beyond which compound nucleus is impossible, then the angular distributions can be refitted to equation 5.9, but with the (worst) condition that $T_I = 0$ for $I > l_c$, while for $I \leq l_c$ the T_I values are taken from the optical model calculations. Figure 5.5 illustrates the serious influence of such a critical l value if it exists for the case of the silver bombardment. The fitted value of K_0^2 is given as a function of the maximum number of partial waves (I values) used in the fitting procedure. Also indicated are the T_I values calculated using an optical model code and standard

figure 5·5

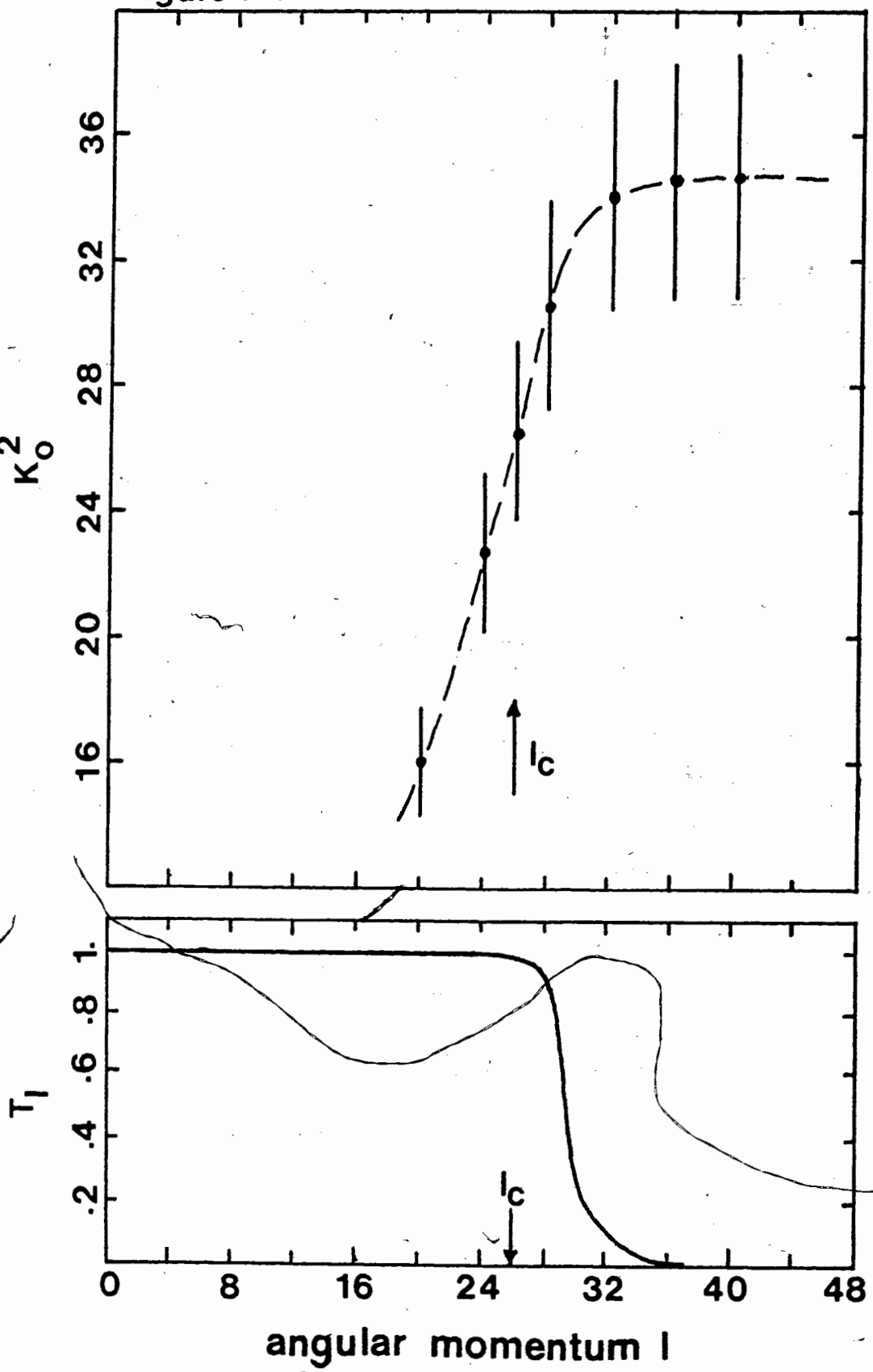
K_o^2
36
32
28
24
20
16
l_c
T_l
1.
.8
.6
.4
.2
l_c
0
8
16
24
32
40
48
angular momentum l

(Igo 59) values for the potential. The K_0^2 value obtained under the assumption that the critical l value can be calculated using the Wilczynski model is 26.5 ± 2.9. The value of K_0^2 for both silver and tellurium are further discussed in section 5.4.

In the case of the gold data, one cannot apply equation 5.9 to fit the experimentally determined angular distributions, without taking the effects of multiple chance fission into account. Figure 5.1 showed that to assume that the distribution in angular momentum of the fissioning nuclei is not altered by the inclusion of second and higher-chance fission is a very poor approximation indeed.

In principle, angular distributions for the fission fragments of each of the fissioning nuclei in Table V.2 - and in each case, each relevant E and I combination - could have been calcutated and summed to give an overall distribution for comparison with experiment. This would have been a very large task, particularly when parameter variation would be needed to secure agreement with the data. Such a task was considered beyond present capabilities and resources.

Instead multiple chance fission was taken into account by employing the average energy from the distribution of figure 5.2 for all fissioning nuclei, and reproducing the effects of the "total" angular momentum distribibition in figure 5.1 by defining a new

quantity, the "effective fission coefficient" ($T_{fiss}(I)$), to be used instead of T_I in equation 5.9. The $T_{fiss}(I)$ coefficients are calculated from the T(I) values characteristic of the compound nucleus via:

$$T_{fiss}(I) = \frac{Y_{total}(I)}{Y_{first}(I)} \times \frac{Y_{first}(I=0)}{Y_{total}(I=0)} \times T_I \qquad 5.24$$

where $Y_{total}(I)$ and $Y_{first}(I)$ are the fission yield values for the overall and first chance fission respectively taken from figure 5.1. In applying these effective fission transmission coefficients to equation 5.9, however, the approximation that M=0 (see section 5.1) becomes less valid, since M is expected to increase with higher chance fission (Van 73).

Figure 5.6 shows the effective fission transmission coefficients for the 80-, 100- and 120-MeV alpha-particle bombardments of gold. Also shown are the T_I values for the entrance channels (i.e. for compound nucleus formation).

In fitting the angular distributions from the alpha particle bombardments of gold both sets of T_I values were used so that the effects of multiple chance fission on the values of K_o^2 could be determined. Figures 5.7, 5.8 and 5.9 show the quality of these fits. Although the overall fit, expressed in terms of a chi-square value, improves slightly by using the $T_{fiss}(I)$ values for the fission exit channels compared to using the T_I

figure 5.6

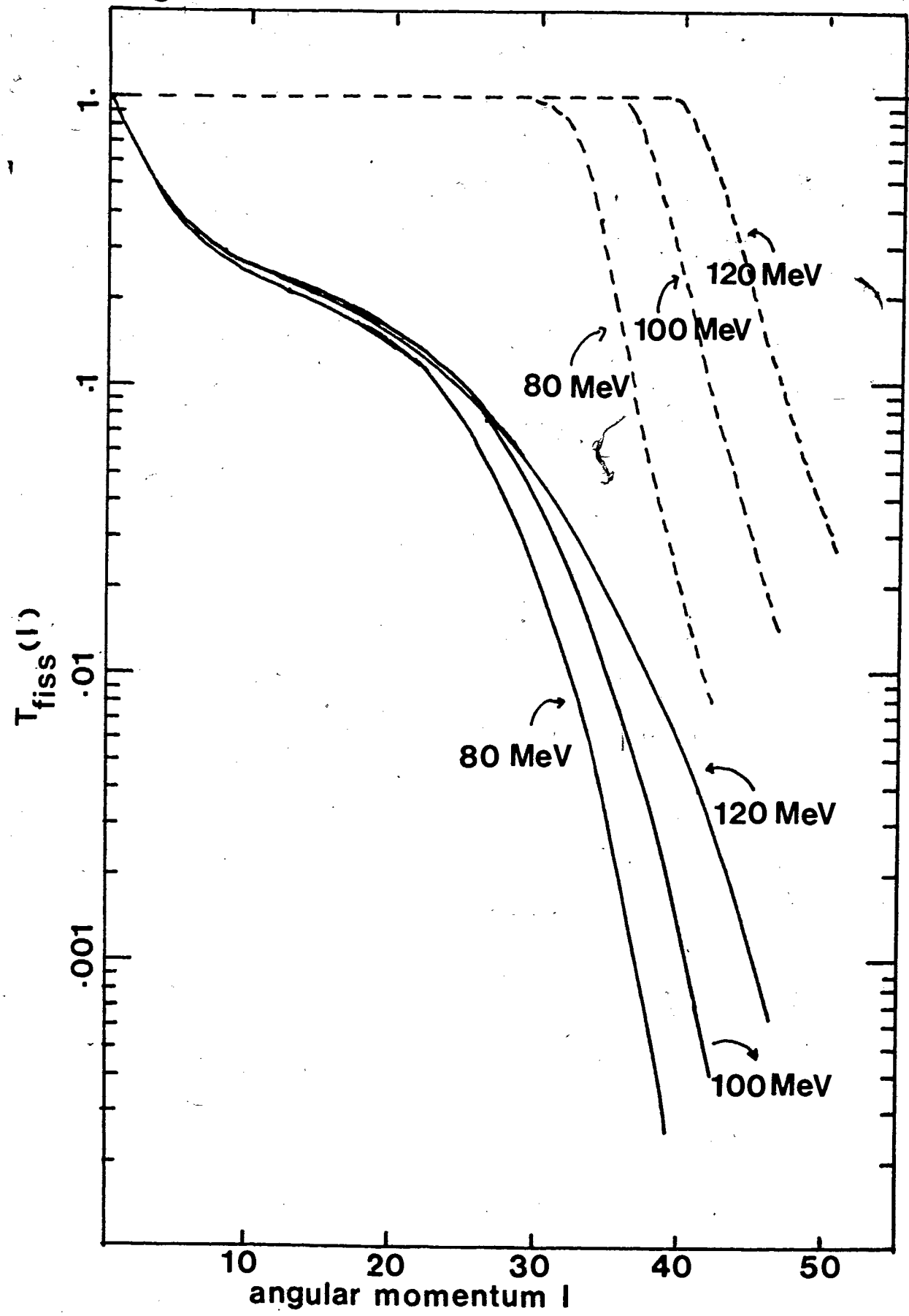
1.
.1
.01
.001
$T_{fiss}(l)$
120 MeV
100 MeV
80 MeV
80 MeV
120 MeV
100 MeV
10
20
30
40
50
angular momentum l

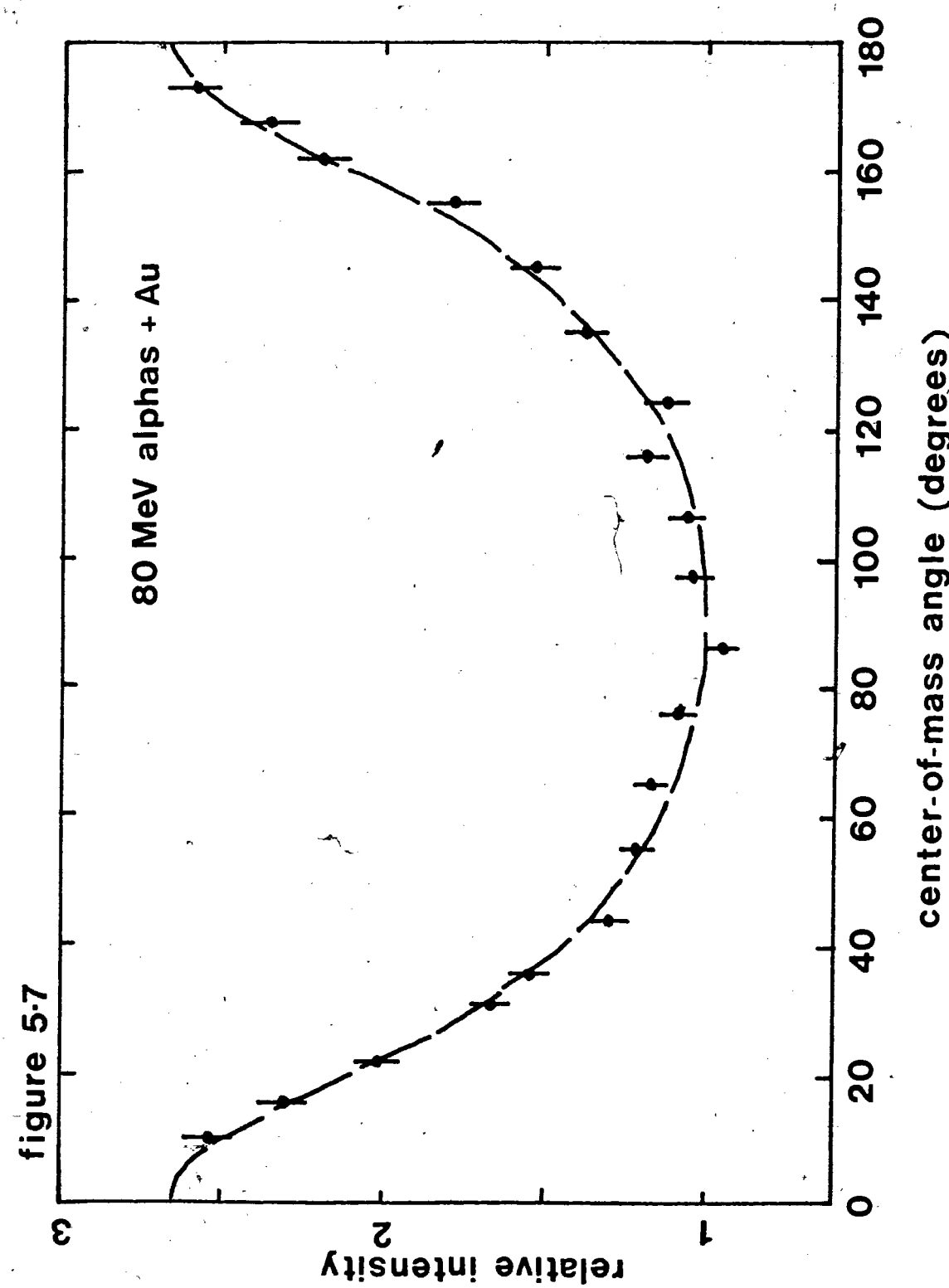
80 MeV alphas + Au
relative intensity
center-of-mass angle (degrees)
0
20
40
60
80
100
120
140
160
180
1
2
3

figure 5·7

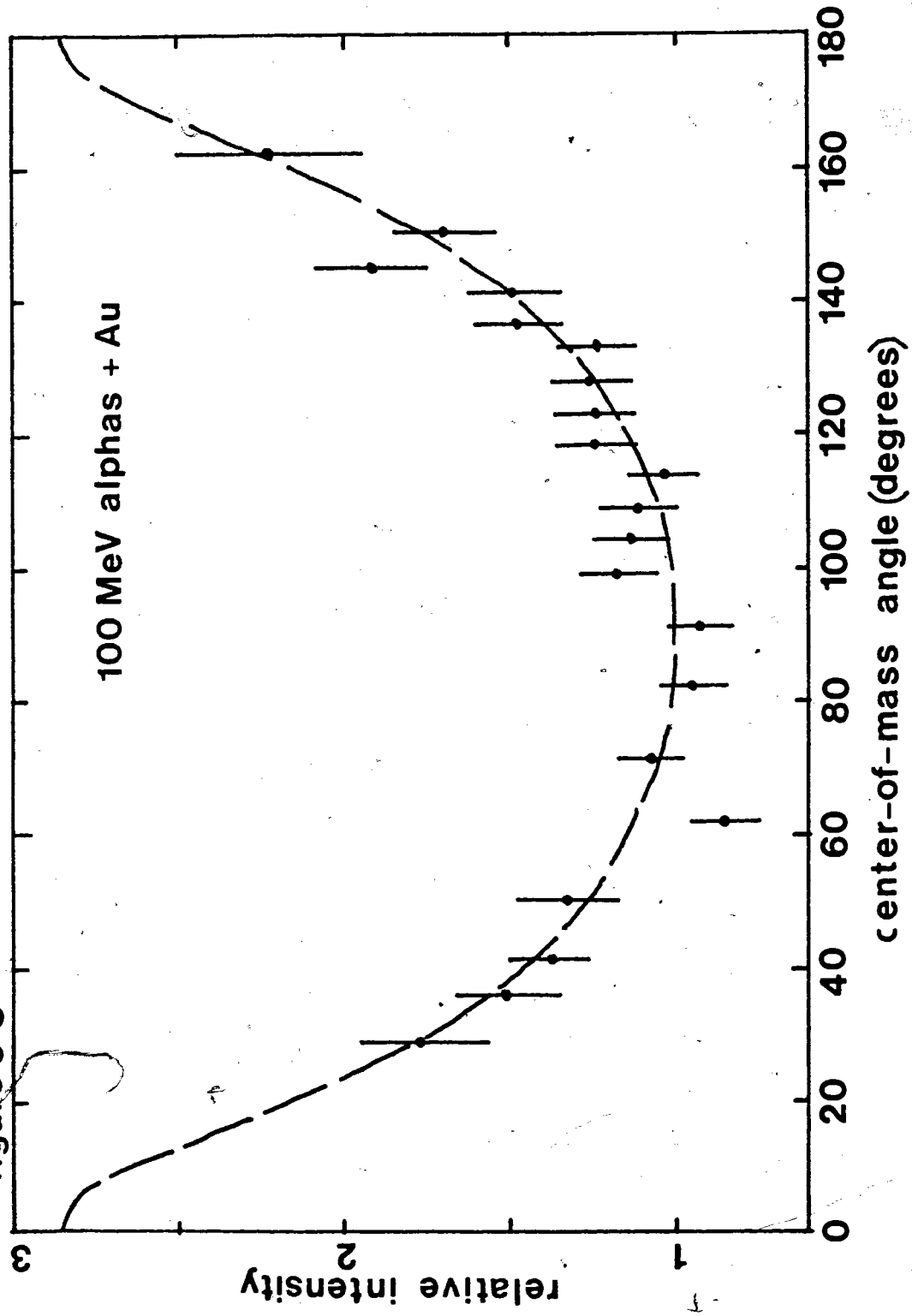
100 MeV alphas + Au
relative intensity
center-of-mass angle (degrees)
0
20
40
60
80
100
120
140
160
180
1
2
3

figure 5.8

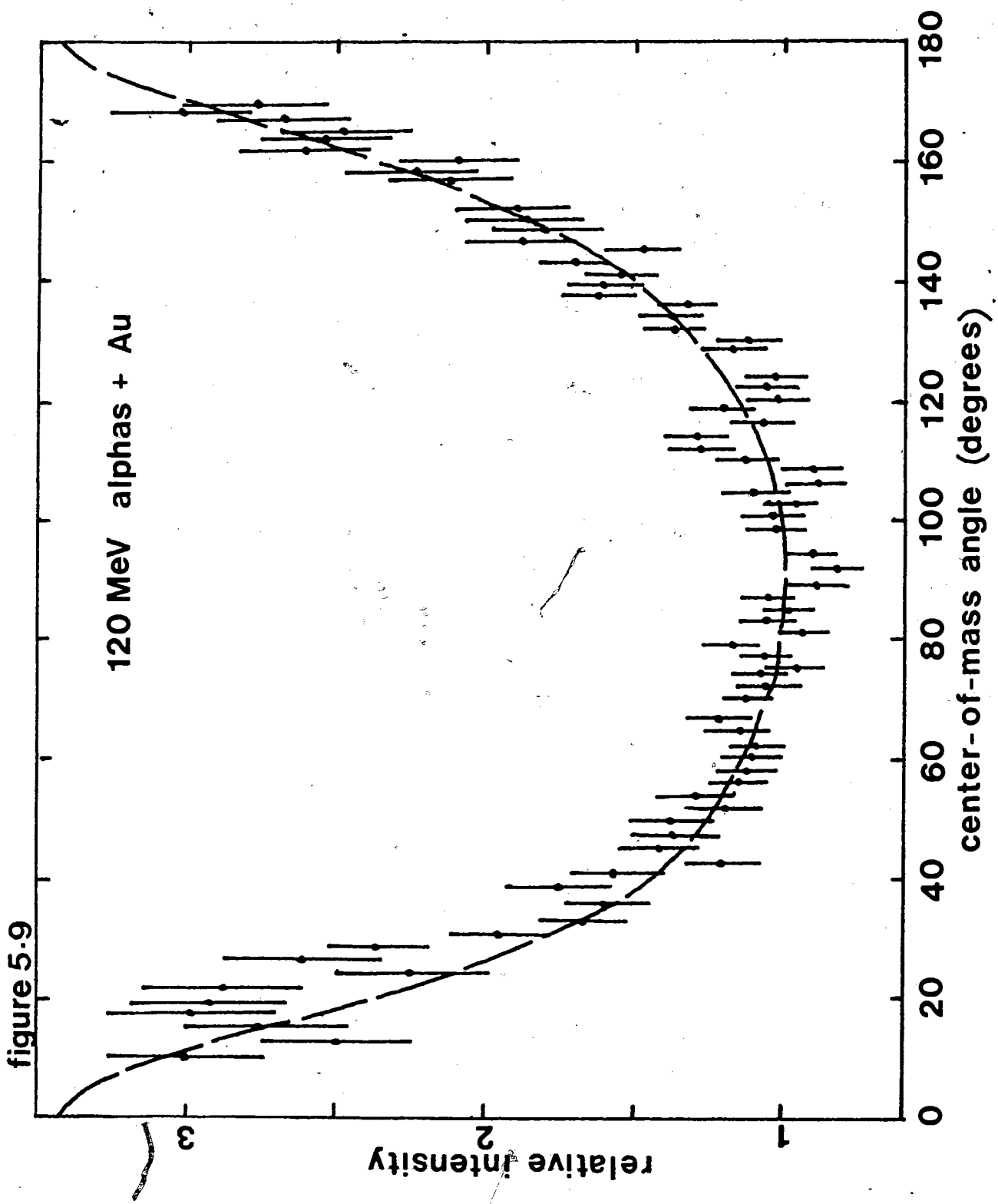
120 MeV alphas + Au
relative intensity
center-of-mass angle (degrees)
0
20
40
60
80
100
120
140
160
180
1
2
3

figure 5.9

values for the entrance channels, a much larger effect occurs in terms of the change in the deduced values of K_0^2, from around 100 to near 40. They are summarized and compared with theoretical expectations in section 5.4.

The data from the 167-MeV alpha particle bombardments of Mo, In and Au do not lend themselves to the above type of analysis. It has already been asserted that in none of these reactions was compound nuclear formation more than a small fraction of the entrance channel (see section 4.2.3). However, a calculation of the competition between fission and particle evaporation is impossible unless the initial population in angular momentum and excitation energy of the products of the initial interaction is know. Estimates of this could perhaps be obtained using an approximate version of the cascade calculation commonly used at higher energies (calculations in which one assumes two body interactions between the incoming particle and the nucleons in the nucleus). Such types of calculations are not yet available for alpha particle induced reactions.

Alternatively the pre-equilibrium decay model due to Blann (Bla 71) might at a later stage of development represent another route to the same information. At the present moment, however, angular momentum information is not produced by it.

Thus analysis of the angular distribution data for 167-MeV alpha bombardments, which arose out of this study, is not possible at

the present moment. The data are however included here for completeness, see figures 5.10, 5.11 and 5.12, transformed into a center-of-mass system via the average center-of-mass velocities determined in section 4.2.3, and plotted to even order Legendre polynomials in order to permit extrapolation to angular regions not covered by the measurements.

5.4 Effective moment of inertia of saddle point shapes.

If one assumes that the distribution in K is Gaussian in nature (Hal 55) (see also section 5.1), then K_0^2 is given by

$$K_0^2 = \frac{t}{\hbar^2}\left\{\frac{1}{\tau_{\parallel}} - \frac{1}{\tau_{\perp}}\right\} = \frac{t\tau_{eff}}{\hbar^2}$$

the effective moment of inertia τ_{eff} is in essence a shape parameter of the nuclear saddle point. Cohen and Swiatecki (Coh 63) as well as Strutinsky et al (Str 63) have calculated this shape parameter using the charged liquid drop model. Figure 5.13 shows their results, together with the available experimental data (solid points) (from Reising et al (Rei 66)). No experimental data are available for nuclei with fissility parameters less than 0.65 (that is lighter than Au). The K_0^2 values deduced from the 80-MeV alpha particle bombardments of Ag and Te (fissility parameters of 0.43 and 0.44 respectively) can hence be used to test the theory at lower fissility values. Table V.4 summarizes all K_0^2 determinations from the previous section. These values of K_0^2 can be converted into estimates

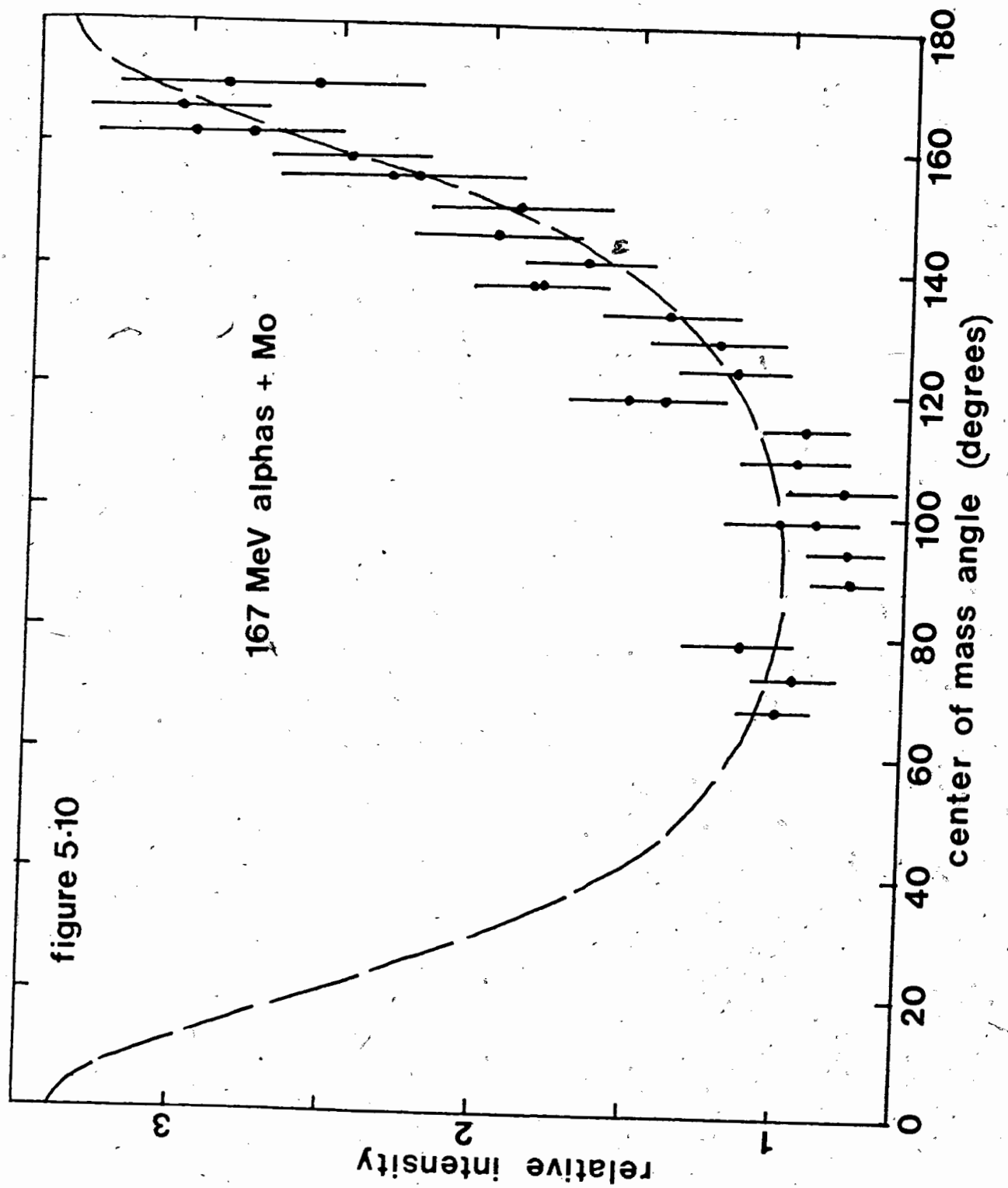
relative intensity
0
1
2
3
0
20
40
60
80
100
120
140
160
180
center of mass angle (degrees)
167 MeV alphas + Mo

figure 5.10

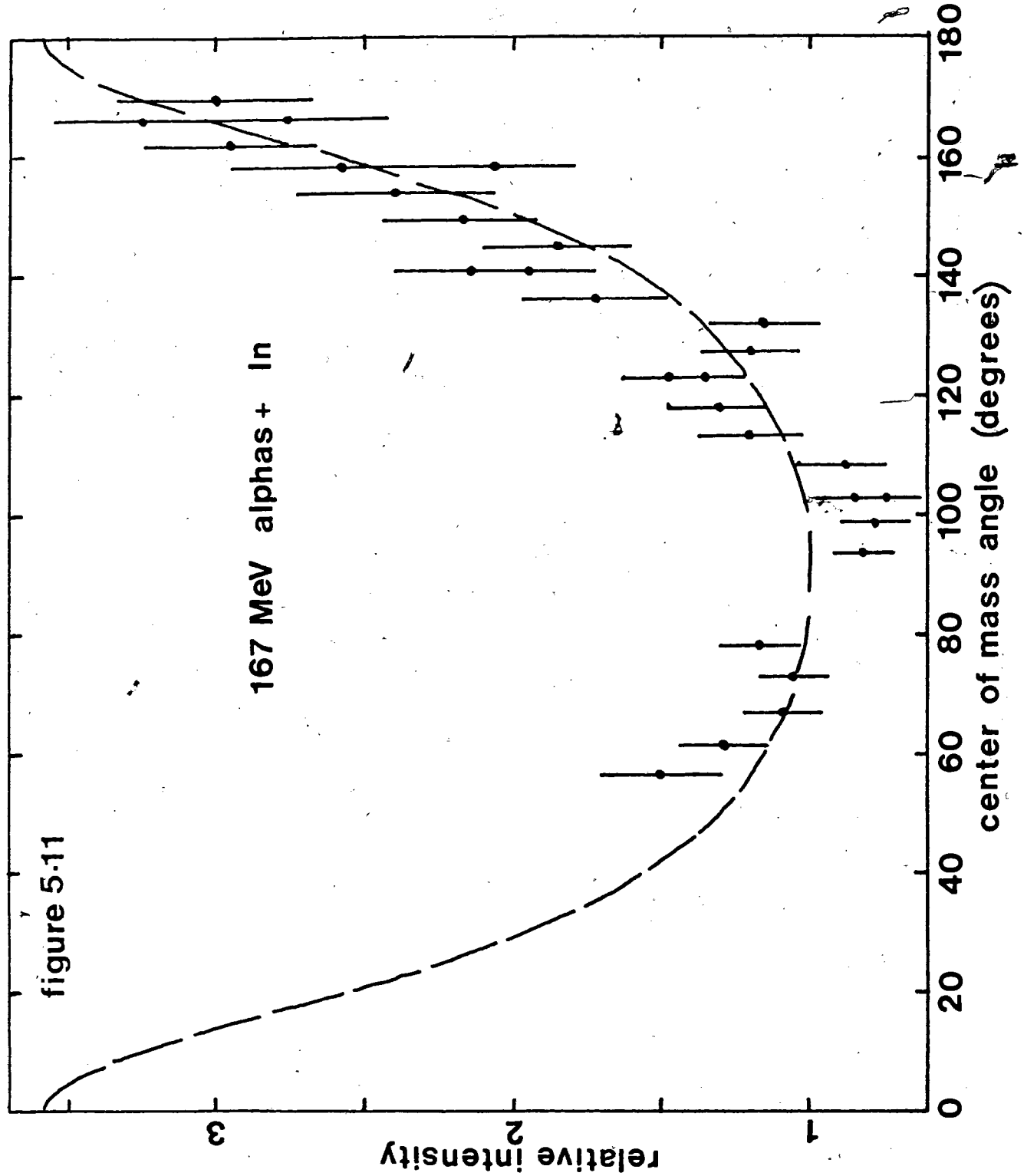
167 MeV alphas + In
relative intensity
center of mass angle (degrees)
0
20
40
60
80
100
120
140
160
180
1
2
3

figure 5.11

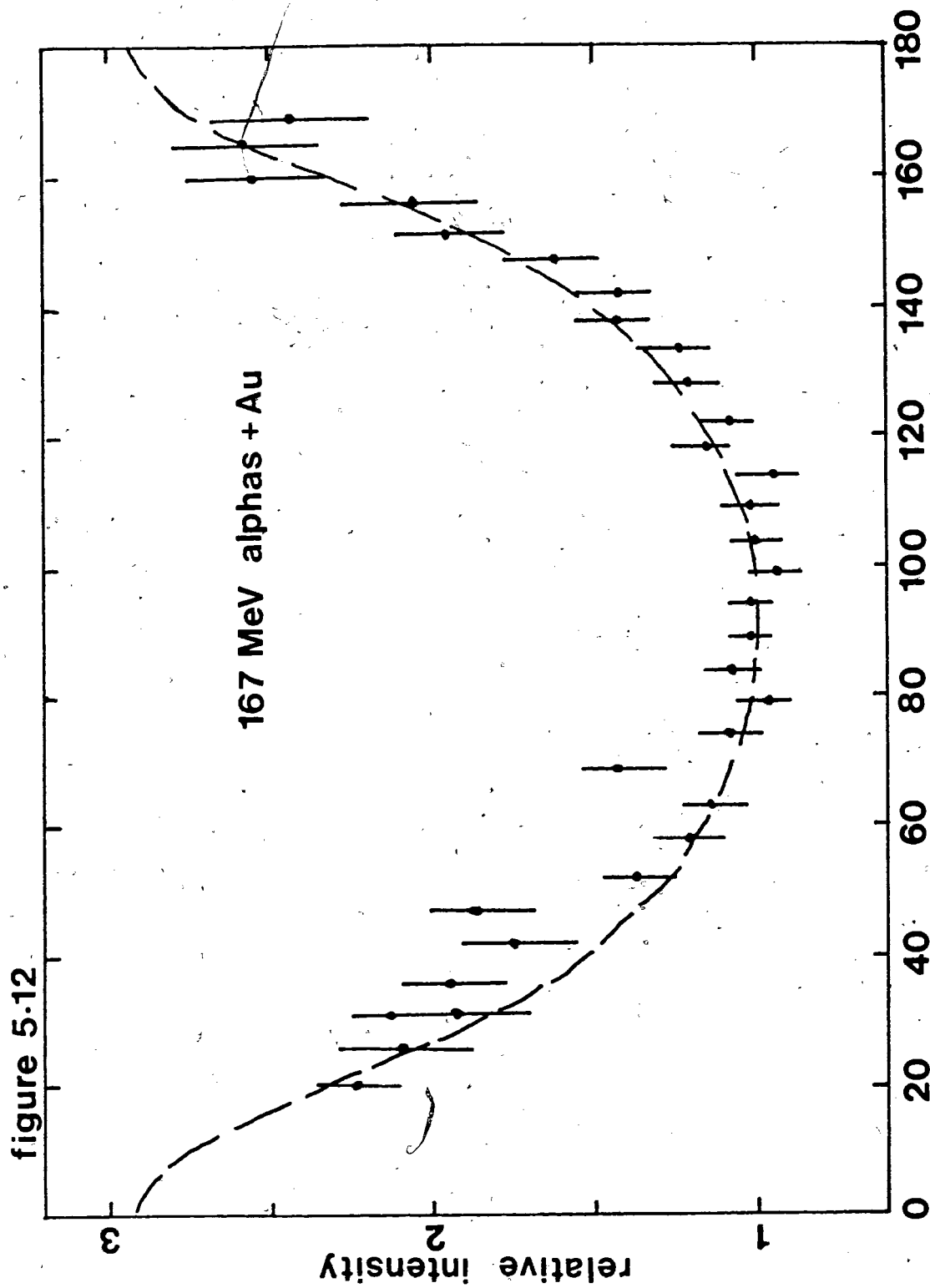
relative intensity
0
1
2
3
0
20
40
60
80
100
120
140
160
180
center of mass angle (degrees)
167 MeV alphas + Au

figure 5.12

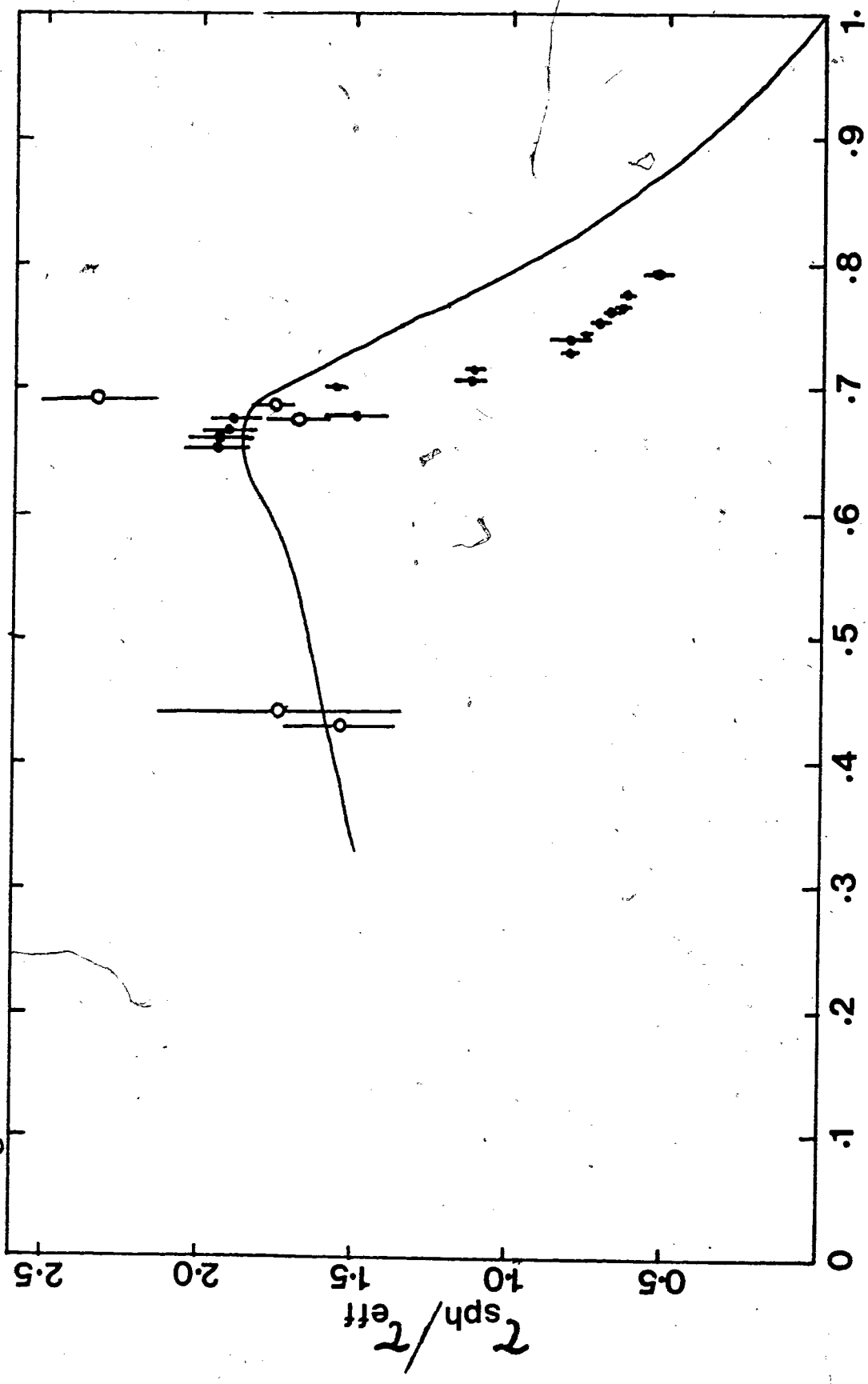

figure 5.13

Table V.4 K_0^2 values derived from the fitting of the angular distributions.

Interaction	fissility parameter of compound nucleus $x = (Z^2/A)/50.1$	K_0^2 using T_l's from entrance channel	K_0^2 with critical I (Wilczynski model)	K_0^2 using $T_{fiss}(I)$ exit channel
80MeVα's+Ag=In^{112}	0.43	34.6 ± 3.8	26.5 ± 2.9	-
80MeVα's+Te=Xe^{132}	0.44	36.4 ± 8.3	30.3 ± 6.6	-
80MeVα's+Au=Tl^{201}	0.65	93.7 ± 4.8	-	41.7 ± 2.3
100MeVα's+Au=Tl^{201}	0.65	124.8 ± 3.2	-	42.7 ± 1.3
120MeVα's+Au=Tl^{201}	0.65	100.7 ± 6.9	-	33.4 ± 2.6

of the effective moment of inertia of the saddle point shapes using equation 5.2. For the temperature of the transition (saddle point shape) nucleus one can use the equation of state $E^* - B_f = at^2 - t$, where E^* and B_f are the average excitation energy and fission barrier of the system and the level density parameter $a = A/8$. The average value of the excitation energy of nuclei was obtained from the calculations described in section 5.2.3, while the fission barrier values used were those due to Myers and Swiatecki (Mye 66). Table V.5 tabulates the τ_{sph}/τ_{eff} values. Here τ_{sph} denotes the rigid body moment of inertia which can be calculated from

$$\tau_0 = (2/5)AR^2 \qquad 5.25$$

For the silver and tellurium data the ratio of τ_{sph}/τ_{eff} is calculated with both sets of K_0^2 values from table V.5. Better agreement with the calculated values of τ_{sph}/τ_{eff} is obtained when no critical angular momentum effect is assumed. The results including this assumption, however, would still verify an important trend predicted by the theoretical calculations, namely that the τ_{sph}/τ_{eff} does not continue to increase with decreasing fissility parameter x below x = 0.65, as the trend of the experimental data for x > 0.65 would otherwise indicate. In the case of the gold data the shape parameters were first calculated using the K_0^2 values derived from the application of the effective transmission coefficients and using

Table V.5 Ratio of the rigid body moment of inertia to the effective moment of inertia of the saddle point shapes.

nucleus	average excitation energy of the transition state nucleus (MeV)	τ_{sph}/τ_{eff}	
In^{112}	30	1.55±0.17	(2.03±0.22)[d]
Xe^{132}	30	1.74±0.39	(2.15±0.47)[d]
Tl^{201}	13[a]	1.69±0.09	(1.56±0.08)[e]
	15[b]	1.76±0.05	(1.36±0.03)[e]
	16[c]	2.33±0.18	(1.88±0.13)[e]

a) from the 80-MeV alpha particle bombardment of Au

b) from the 100-MeV alpha particle bombardment of Au

c) from the 120-MeV alpha particle bombardment of Au

d) these values are obtained if the effects of a critical l value are included in the K_0^2 determination.

e) these values are obtained using the common assumption that the angular momentum distribution of the fissioning nuclei is that of the compound nucleus and the the excitation energy is the excitation energy of the compound nucleus.

the mean excitation energy of the fissioning nuclei as calculated in section 5.2.3 (see for instance figure 5.2). Since this procedure should correct for multiple chance fission, the resulting values of τ_{sph}/τ_{eff} should be identical for all energies of the incident alpha particles. From Table V.6 it can be seen that the values from 80- and 100-MeV alpha particle bombardments are consistent with this, but the result from the 120-MeV alpha particle bombardment appears somewhat high. For this latter case, however, it is less certain that in the entrance channel compound nucleus formation is still close to 100% of the initial interactions (see chapter 4). If not the data will have to be treated in the same way as those from the 167-MeV alpha particle irradiations, and no reliable estimate of K_0^2 can be obtained.

For comparison Table V.5 also lists the shape parameters which can be obtained using the common assumption that the angular momentum distribution of the fissioning nuclei is the same as that of the compound nucleus, and that the excitation energy is also that of the compound nucleus. Although the first assumption increases the K_0^2 values by more than a factor of two, the assumption of a high excitation energy cancels this effect out again when τ_{eff} is determined from the ratio of K_0^2 and the temperature of the transition state nucleus. Consequently the shape parameters obtained this way are still reasonably close to the values obtained when multiple chance fission is properly taken into account.

The τ_{sph}/τ_{eff} values in column three of table V.5 are plotted together with previously determined values and the theoretical predictions in Figure 5.13. The excellent agreement that is obtained between the "corrected" shape parameters and results obtained at much lower excitation energies (see figure 5.13) would seem to confirm the validity of this method of analysis of the experimental data, and verifies the theoretical predictions.

Chapter 6 Conclusions

It has been shown that fission can be induced in medium mass nuclei such as silver and tellurium, by alpha particles with energies as low as 80 MeV. The tracks observed in mica detectors from these interactions were interpreted as fission fragment tracks by the following criteria; 1) mica registers only fragments with a mass heavier than 20 amu; 2) measured track length values are consistent with fragments having approximately half the target mass and energies corresponding to Coulombic repulsion of the fragments, and 3) after conversion into the center-of-mass system the angular distribution of the fragments was symmetric around 90°.

A simulation computer program was written which describes the fission of medium mass nuclei and the subsequent stopping of the fission fragments in mica track detectors. By varying the most sensitive parameters in the calculations, (center-of-mass motion, total kinetic energy release and the width of the fragment mass distribution) the best possible agreement with the measured track length distributions in mica of the fission fragments from a number of fissioning systems was sought. Under the restraint of a number of assumptions inherent in the development of such a large simulation code, the deduced values for the center-of-mass motion of the systems studied showed that for the 80-MeV alpha particle bombardments the entrance channel for fission events is compound nucleus formation. For

the 167-MeV alpha particle bombardments significant contributions to the entrance channel are made via different processes (i.e. possible direct interactions leaving a significant amount of excitation energy in the target nucleus or pre-equilibrium emission of particles).

Only upper limits on the total kinetic energy release in the fission process (defined as the kinetic energy release in the case of a symmetric fission event) could be determined, due to the use of the touching spheres approximation in calculating the kinetic energy of fission fragments as a function of mass asymmetry. These limits are in fair agreement with theoretical estimates using the liquid drop model (Nix 69).

Under the restraint of the assumptions used in the calculation of fission fragment track length distributions, it was shown that the width of the fission fragment mass distributions from the silver and tellurium plus alpha systems was relatively narrow. The predicted dramatic broadening of the mass distribution for fissioning systems with fissility parameters close to or beyond the critical x_{BG} VALUE (Nix 69) was, therefore, not substantiated.

A detailed calculation of the competition between fission and particle evaporation in the de-excitation of the compound nucleus shows that although the effects of multiple chance fission are negligible in the case of the silver and tellurium

plus alpha fissioning systems, this effect plays a very dominant role in the gold plus alpha system. Instead of a decreasing probability for fission with an increasing number of evaporated neutrons, the main contribution to the total fission cross section was shown to come from nuclei which have already evaporated six to nine neutrons. By calculating the distribution in angular momentum and excitation energy of the fissioning nuclei using the statistical model, a meaningful analysis of the angular distributions of the fission fragments from the gold plus alpha systems could still be made.

The effective moments of inertia of the saddle point shapes were derived from the angular distribution data and are in excellent agreement with the predictions of Cohen and Swiatecki (Coh 63) and Strutinski et al (Str 63). They confirm that the ratio of the rigid body moment of inertia to the effective moment of inertia of the saddle point shape decreases below fissility parameter values of 0.65.

To summarize, the entrance channels of a fission reaction, even at the medium excitation energies employed in this study, cannot always be calculated under the assumption that all fission events are preceded by compound nucleus formation. Further research in this field will, therefore, have to concentrate more on looking at the entrance channels (for example by measuring lighter particles in coincidence with the fission fragments) as well as the fission exit channels. In those

cases where it was possible to calculate the entrance channels of the fission reaction (i.e. in the case of the 80-MeV alpha particle bombardments) interpretation of the data derived from mica track detectors is still dependent on a number of assumptions used in the development of both the fission track simulation code and the fission-evaporation competition program. More direct measurement of the kinetics of fission processes via telescope detectors could be used to ascertain the results obtained using the fission-track simulation code, while measurement of evaporation residue cross-sections could do likewise for the evaluation of the fission-evaporation program.

Appendix 1 RADICS

1. Mathematical Description

1.1 Some Basic Formulas

To calculate fission parameters such as the width and magnitude of energy and mass distributions some basic parameters have to be evaluated (Nix 69):

The fissility parameter x is defined as the ratio of coulomb to surface energy; hence

$$x = \frac{Z^2/A}{50.88 \left\{1 - 1.7826\left(\frac{N - Z}{A}\right)^2\right\}} \qquad (A1)$$

where N, Z and A represent the neutron number, charge and mass number of the fissioning system respectively.

The unit of surface energy E_s^o:

$$E_s^o = 17.9439 \left\{1 - 1.7826 \left(\frac{N - Z}{A}\right)^2\right\} A^{2/3} \qquad (A2)$$

The nuclear temperature τ at the saddle point is obtained from the expression:

$$A\,\tau^2/8 - \tau = E^* - B_f \qquad (A3)$$

where E^* and B_f are the fissioning nucleus excitation energy and fission barriers respectively.

1.2 Total Kinetic Energy Release

The total kinetic energy release of the system is assumed to be represented by a gaussian distribution around an average value. The average value can be entered as an adjustable parameter or, as an initial estimate, the program will supply a theoretical value. The theoretical values were obtained from the data due to Nix (Nix 69). By fitting these data to a fourth degree polynomial they can be expressed as

$$E = E_s^o \{ C_a + C_b x + C_c x^2 + C_d x^3 + C_e x^4 \} \qquad (A4)$$

where the unit of surface energy E_s^o is given by equation (A2), and x is the fissility parameter.

Table A1 Coefficients in Equation (A4)

C_a	2.6573×10^{-4}
C_b	4.5134×10^{-1}
C_c	-1.8124×10^{-1}
C_d	-1.4306×10^{-1}
C_e	2.1999×10^{-1}

The width of the gaussian distribution around this value is also predicted by Nix (Nix 69). The width of the distribution is not only a function of the fissility

parameter x , but also of the nuclear temperature of the fissioning nucleus. First a 5th degree polynomial was fitted to the curves of reference (Nix 69), which gives the width as a function of x for nuclear temperature values of 0, 1, 2 and 3 MeV. The coefficients of these fits were then fitted as a function of nuclear temperature, so that for any given nuclear temperature value a curve could be generated giving the dependence of the energy on the fissility parameter.

The 5 coefficients for a given τ are obtained from

$$C(I) = C_0(I) + C_1(I)\tau + C_2(I)\tau^2 + C_3(I)\tau^3 \qquad (A5)$$

where I runs from 1 to 5. The values for $C_0(I)$, $C_1(I)$, $C_2(I)$ and $C_3(I)$ are given in table A2.

The width dE (MeV) is then obtained from

$$dE = C(1) + C(2)x + C(3)x^2 + C(4)x^3 + C(5)x^4 + C(6)x^5 \qquad (A6)$$

1.3 Kinetic Energy of Fragments

For the calculation of the kinetic energy of each fragment it is assumed that the variation with mass-asymmetry can be calculated using an approximation in which the scission configuration is taken to that of two touching (tangent) charged spheres. The total kinetic energy is then

Table A2 Coefficients for Equation A5

I	$C_0(I)$	$C_1(I)$	$C_2(I)$	$C_3(I)$
1	-3.7801×10^{-2}	-5.9839×10^{-2}	2.7833×10^{-2}	-6.1302×10^{-3}
2	4.2679×10^{1}	4.3820×10^{0}	4.4449×10^{0}	-8.2171×10^{-1}
3	-2.0068×10^{2}	-9.2173×10^{1}	4.9253×10^{0}	-5.9734×10^{-2}
4	5.7683×10^{2}	3.8465×10^{2}	-3.4010×10^{1}	1.8683×10^{0}
5	-7.4340×10^{2}	-5.5168×10^{2}	4.8646×10^{1}	-2.2766×10^{0}
6	3.7184×10^{2}	2.5313×10^{2}	-1.9872×10^{1}	7.4742×10^{-1}

$$E = C \frac{Z_1 Z_2}{A_1^{1/3} + A_2^{1/3}} \qquad (A7)$$

Where the subscripts 1 and 2 refer to the two fission fragments and the proportionality constant C is obtained by normalization of the calculated average total kinetic energy release to the above data for the case of symmetric fission (i.e. tangent spheres of equal Z and A). Thus

$$C = E \frac{8\ (A/2)^{1/3}}{Z^2} \qquad (A8)$$

where E is the total kinetic energy release for the case of symmetric fission so that

$$E(A_1, A_2) = 8E \frac{(A/2)^{1/3}}{Z^2} \frac{Z_1 Z_2}{A_1^{1/3} + A_2^{1/3}} \qquad (A9)$$

where all symbols have been defined before. In order to obtain the laboratory kinetic energy for each fragment, (under the assumption of compound nucleus formation) the center-of-mass velocity of the system is calculated from

$$V_{CM} = 1/A \sqrt{2A_p E^*}$$

where A_p is the mass of the projectile. The velocity of fragment of mass A_1 in the center-of-mass system is

$$V_1 = \{2E(A_1, A_2)/(A_1 [1 + A_1/A_2])\}^{1/2} \qquad (A10)$$

Then for a given laboratory angle ϕ, the corresponding center-of-mass angle θ is given by

$$\theta = \sin^{-1} \{ (V_{CM}/V_1) \sin \phi \} + \phi \qquad (A11)$$

and the laboratory kinetic energy E_1 for fragment of mass A_1 is expressed by

$$E_1 = 0.5 \{ (V_1 \sin \theta)^2 + (V_{CM} + V_1 \cos \theta)^2 \}^{1/2} \qquad (A12)$$

1.4 Effects Which Add to the Width of Fragment Kinetic Energy Distributions

1.41 Broadening due to experimental angular resolutions:

Since the measurement of track lengths at a unique angle of observation is only possible in the case of an infinite track density on the detector surface, the actual measurements for a given mean angle θ of observation usually cover an angular interval, $\Delta\theta$, of from 1 to 5 degrees. The broadening of the kinetic energy distribution due to this effect is taken into account by calculating the fragment kinetic energy for the mean angle (E_1) as well as for the two extreme angles $\theta - \frac{1}{2}\Delta\theta(E_2)$ and $\theta + \frac{1}{2}\Delta\theta(E_3)$. A width of $(2/3)(E_3-E_2)$ is then added in quadrature to the other widths contributing to the dispersion of E_1.

1.42 The broadening due to the original width in total kinetic energy release for symmetric fission:

Due to the distribution of nuclear elongations at the scission point, the total kinetic energy release in symmetric

fission does not have a unique value, but rather a Gausian (Nix 69) distribution of values around the mean value (see also section 1.1 of this appendix). In order to reflect this in the kinetic energy of the fragment E_1, a Gaussian width (EWIDTH) is added (in quadrature) to the other widths contributing to the dispersion of E_1. If EFWHM is the width of the Gaussian distribution of E_{sym}, then EWIDTH is taken to be given by: $EWIDTH = (EFWHM/E_{sym}) \times E_1$.

1.43 The broadening in energy due to the target thickness TT as well as the shift in average energy due to target thickness

this is accounted for by first calculating the distance that the fragments travel on average through the target material. The target was always at 45° to the beam direction in the experimental set up. The average distance is then

$$d = \frac{(TT/2)\,SIN\ 45^\circ}{SIN\ (135-\phi)^\circ} \quad ; \quad 90^\circ$$

and

$$d = \frac{(TT/2)\,SIN\ 45^\circ}{SIN\ (\phi-45)^\circ} \quad ; \quad 90^\circ \qquad \text{A13}$$

where ϕ is the fission fragment emission angle with respect to the beam direction. The energy loss per unit path length in any target material was obtained by an interpolation of the data due to Northcliffe (Nor 70). This interpolation procedure was necessary for two reasons; a) Northcliffe's tables cover only a limited number of targets and projectiles, and b) the tables, even in their present condensed form are too

bulky to be included as data arrays in the computer program. The objective then, was to be able to generate the specific energy loss of any projectile in any solid target material from as small a number of parameters as possible, without a significant loss in accuracy with respect to the data as given in Northcliffe's tables.

This objective could be accomplished largely due to the fact that the relative stopping power of two materials is independent of the incident ion mass and charge at a given ion velocity (Nor 70); hence the problem was reduced to the calculation of the stopping power of only one material for all possible incident ions, as well as the relative stopping power of that material to all other possible materials. The material for which stopping power data are most reliable is aluminum, and the first step was, therefore, to express these data in the simplest terms. The stopping power of aluminum for ions with a charge of 6, 12, 18, 28, 40, 52, 66, 80 and 95, as a function of the velocity of the incident ion, was taken from the tables of Northcliffe, and an attempt was made to fit a general nth degree polynomial to the data for each incident ion. However, irrespective of the value of n, the coefficients of these fits did not vary smoothly with the charge of the incident ion, so that it was not possible to make a reliable 'cross-fit' of these coefficients. A much better result was obtained by dividing

the stopping power data into two velocity regions: 0 - 0.5 MeV/amu and 0.5 - 5.0 MeV/amu. A 4th degree polynomial was fitted to the data for each of these regions, so that ten coefficients were necessary to describe the variation of the stopping power with the velocity for each of the above mentioned incident ions. These coefficients varied smoothly with the charge of the incident ion, and could be fitted to another 4th degree polynomial. Ten such secondary fits were made, each of them yielding five new coefficients. If we denote the incident ion by its charge number Z, and the fifty secondary coefficients are stored in the matrix CAL(x,y,E) (where E = 1 or 2 depending on the velocity v of the incident ion, y specifies which coefficient of the primary fit we are interested in and x is the index specifying the 5 coefficients of each secondary fit) then the primary coefficients C(y) can be obtained for any z and v from

$$C(y) = CAL(1,y,E) + \sum_{x=2\to5} CAL(x,y,E)\, z^{(x-1)} \qquad A14$$

Hence the stopping power in aluminum for an incident ion of charge z with the velocity v is given by

$$dE/dx_{Al}\ (z,v) = C(1) + \sum_{y=2\to5} C(y)\, v^{(y-1)} \qquad A15$$

Since it was also necessary to obtain the relative stopping power of any solid material with respect to aluminum, the

ratio of the stopping power of materials with Z = 22, 28, 32, 40, 47, 63, 73, 79 and 92 to that of aluminum as a function of the velocity, was obtained from Northcliffe's tables. In fitting these data it was again necessary to divide the data into values for various velocity regions, so that the coefficients of the primary fits ($dE/dx_Z/dE/dx_{Al}$ versus velocity) varied smoothly with the charge of the stopping material. Six velocity regions were needed (0 - 0.04; 0.04 - 0.16; 0.16 -0.5; 0.5 - 1.25; 1.25 - 2.5 and 2.5 - 5.0 MeV/amu) and a simple 1st degree polynomial was fitted to the data in each of the velocity regions. The coefficients of these primary fits were then fitted as a function of the charge of the stopping material to a 4th degree polynomial, yielding a total of 60 secondary coefficients which were stored in the matrix CRAT(x,y,E), where the index numbers have similar meanings to those of the matrix CAL(x,y,E). The ratio of the stopping power of a medium with charge Z to the stopping power of aluminum for a given velocity v, can then be found using the coefficients of the secondary fits to generate the two coefficients of the primary fits

$$\frac{(dE/dx)_Z}{(dE/dx)_{Al}} = R_Z(v) = CRAT(1,1,E) + \sum_{x=2\to5} CRAT(x,1,E)\,Z^{(x-1)} + V\left\{CRAT(1,2,E) + \sum_{x=2\to5} CRAT(x,2,E)\,Z^{(x-1)}\right\} \quad (A16)$$

Table A3 The Matrix CAL (C', C, CR)

FOR CR = 1 (0 0.5 MeV/amu)

	C'_1	C'_2	C'_3	C'_4	C'_5
C_1	.60743E-01	.18266E+00	-.45900E-02	.54542E-04	-.23799E-06
C_2	.21104E+02	.56542E+01	-.94309E-01	.98151E-03	-.37771E-05
C_3	-.20983E+03	-.80386E+01	.11902E-01	.49824E-03	-.36973E-05
C_4	.59916E+03	-.11891E+02	.10657E+01	-.15607E-01	.72037E-04
C_5	-.55794E+03	.27184E+02	-.15749E+01	.22545E-01	-.10317E-03

FOR CR = 2 (0.5 5.0MeV/amu)

	C'_1	C'_2	C'_3	C'_4	C'_5
C_1	.10453E+01	.85306E+00	-.13956E-01	.81100E-04	-.64712E-07
C_2	-.72544E+01	.10083E+01	-.15545E-02	.13915E-03	-.12863E-05
C_3	.35284E+01	-.63908E+00	.55341E-02	-.12563E-03	.99289E-06
C_4	-.69356E+00	.13906E+00	-.14402E-02	.30592E-04	-.24203E-06
C_5	.48516E-01	-.10374E-01	.10803E-03	-.23384E-05	.19099E-07

Table A4. The Matrix CRAT(C',C,CR)

FOR CR = 1 (0 - 0.04 MeV/amu)

	C'_1	C'_2	C'_3	C'_4	C'_5
C_1	.14524E+01	-.61208E-01	.14645E-02	-.17112E-04	.73854E-07
C_2	0	0	0	0	0

FOR CR = 2 (0.04 - 0.16 MeV/amu)

	C'_1	C'_2	C'_3	C'_4	C'_5
C_1	.13727E+01	-.55019E-01	.12669E-02	-.14555E-04	.62351E-07
C_2	.43000E+00	0	0	0	0

FOR CR = 3 (0.16 - 0.50 MeV/amu)

	C'_1	C'_2	C'_3	C'_4	C'_5
C_1	.13945E+01	-.52153E-01	.11571E-02	-.12976E-04	.54719E-07
C_2	.17700E+00	0	0	0	0

FOR CR = 4 (0.50 - 1.25 MeV/amu)

	C'_1	C'_2	C'_3	C'_4	C'_5
C_1	.13266E+01	-.41343E-01	.82962E-03	-.89160E-05	.37035E-07
C_2	.71000E-01	0	0	0	0

FOR CR = 5 (1.25 - 2.5 MeV/amu)

	C'_1	C'_2	C'_3	C'_4	C'_5
C_1	.12509E+01	-.30849E-01	.50229E-03	-.46786E-05	.17849E-07
C_2	.37000E-01	0	0	0	0

FOR CR = 6 (2.5 - 5.0 MeV/amu)

	C'_1	C'_2	C'_3	C'_4	C'_5
C_1	.12308E+01	-.25411E-01	.34568E-03	-.27314E-05	.92414E-08
C_2	.17000E-01	0	0	0	0

where E is a function of v, in so far as it denotes which of the six energy regions is applicable.

The energy loss per unit path length for any ion of charge z in any stopping material (Z) at any velocity (v) can then be found by first calculating the appropriate $R_Z(v)$ ratio using the matrix CRAT, and multiplying by the $(dE/dx)_{Al}(z,v)$ value which can be extracted from the matrix CAL. The average energy loss is then

$$dE_{TT} = d \cdot R_Z(v) \cdot (dE/dx)_{Al}(z,v) \qquad \text{A17}$$

where d was defined in equation A13. In calculating the fragment energy distribution, first of all the average value is decreased by dE_{TT}, and secondly an assumed equivalent width of 2/3 dE_{TT} is added in quadrature to the other dispersions of the fragment kinetic energy value.

1.5 Evaluation of track length or diameter values.

Track length distributions in mica from ions of a unique mass and energy have been shown to be Gaussian with tailing towards lower range values (see section 2.3). Analytically the distribution is represented as

$$\omega_L = N\exp\left\{ - \frac{T^2(2L-2\bar{L}+T^2)}{2W^2} \right\} \quad ; \quad L < \bar{L}-T^2$$

$$\omega_L = N\exp\left\{ - \frac{|L - \bar{L}|^2}{2W^2} \right\} \quad ; \quad L \geqslant \bar{L} - T^2 \qquad \text{A18}$$

In the case of glass, the track diameter distribution is taken to be Gaussian:

$$\omega_D = N\exp\left\{ - \frac{|D - \bar{D}|^2}{2W^2} \right\} \qquad \text{A19}$$

In the above equation N represents a normalization constant, W is the width parameter, T is the tailing parameter while $\bar{D}$ and $\bar{L}$ are the most probable values for the diameter and track length. The tailing and width parameters were extracted from experimental calibration studies.

In order to calculate the track length or diameter distributions from the energy distribution data for each fragment mass value, data arrays were generated for the particular stopping medium, which gave the track length or diameter for each possible fragment mass value for a range of energy values. In the present program (version 8.5) the energy increment is taken as 0.02 MeV/amu. These data can be generated during the execution of the program or provided externally. In the case of glass, usually an externally supplied data set is used, because the diameter is only dependent on the charge and energy of the incident ion, whereas in mica, the track length depends also on the mass of the incident ion.

Since the mass-charge ratio is not constant for every fissioning system, the option is left open to recalculate the track length-mass-energy data for each fissioning system. Basically each track length value in mica is represented by (see section 2.4)

$$R_{A_1 Z_1 E_1}(\text{mg/cm}^2) = -dR_{A_1} + 0.0434 \frac{A_1 (Z_1^{2/3} + 10^{2/3})^{3/2}}{Z_1^{7/6}} E_1^{0.64} \quad \text{(A20)}$$

where the dR values were given in section 2.4 and E_1 is in MeV/amu. Under the assumption of local linearity of the track length (or diameter) versus energy data, such quantities as Gaussian widths expressed in energy terms are converted to widths in terms of track lengths or diameter units. The total width describing the distribution in track length or diameter for each fragment mass is given by

$$W^2 = \rho_E^2 + \rho_{TT}^2 + \rho_{AR}^2 + \rho_R^2 \quad \text{(A21)}$$

where the subscripts E, TT, AR and R represent contributions due to the gaussian width of the original total kinetic energy distribution, the target thickness, the angular resolution and the range straggling effect respectively. This latter factor is treated as an externally supplied variable, together with the tailing parameter, if present.

The normalization factor for each distribution is obtained from the fragment mass yields as described next.

1.6 Fragment mass distribution

The fragment mass distributions in the center-of-mass system are taken to be composed of one or more Gaussians. Three different cases are possible.

Type I — a single Gaussian defined (see figure A1.1) by the FWHM (A) of the distribution

Type II — two Gaussians of equal intensity and width, separated by a distance B

Type III — a triple Gaussian. This is really the sum of a type I and a type II distribution where besides the FWHM of the center peak (C), the relative intensity F is also an additional variable (F = D/E).

All mass distributions in the center-of-mass system can be converted to distributions in the laboratory system by taking into account the fact that the ratio of the number of fragments of a given mass arriving per steradian at laboratory angle ϕ to those emitted at a center-of-mass angle θ is given by

$$R = \frac{\mathrm{SIN}\theta \, d\theta}{\mathrm{SIN}\phi \, d\phi} \qquad \text{A22}$$

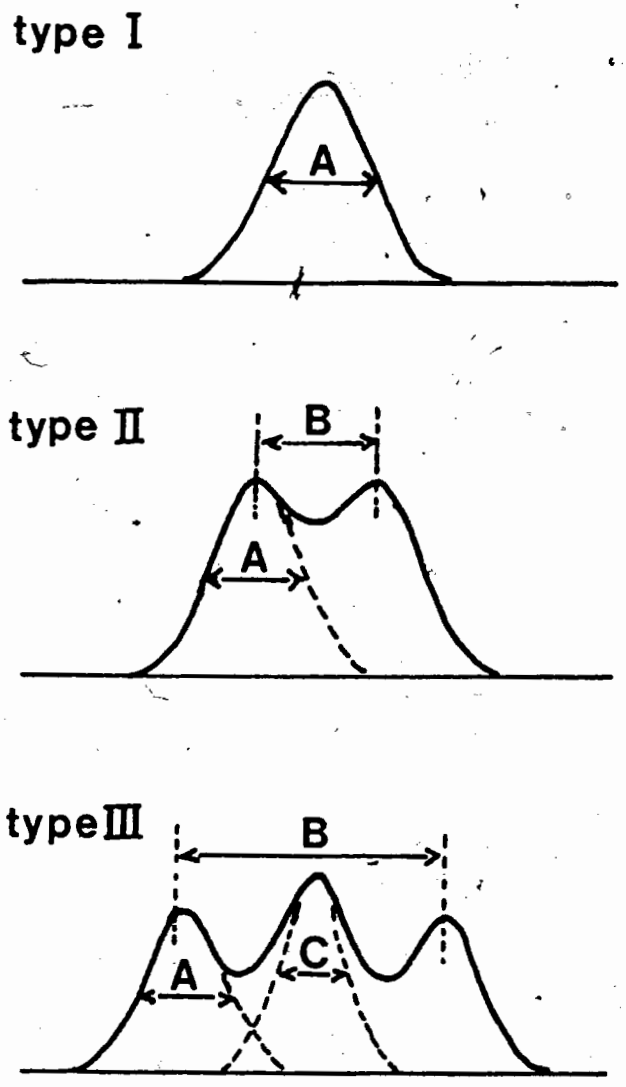

figure A1.1

using equation (A11)

$$R = \frac{\text{SIN } \theta}{\text{SIN } \phi} + \left\{\frac{V_{CM}}{V_F} \text{ SIN } \theta \text{ COS } \phi\right\} \Big/ \left\{\text{SIN } \phi \sqrt{1-\left(\frac{V_{CM}}{V_F} \text{ SIN } \phi\right)^2}\right\} \quad \text{(A23)}$$

In order to find the relative deviation in the mass distribution of fragments arriving at a given laboratory angle, from the original distribution in masses of the emitted fragments, one has to calculate the ratio R for all values of V_{CM}/V_F (corresponding to each possible mass division) and compare with the ratio for the V_{CM}/V_F value corresponding to symmetric mass division. In order to take the experimental angular resolution of a particular measurement into account, the ratio R is integrated over the angular interval considered.

The track length or diameter distributions for each possible fragment, whose shapes were determined earlier, are then normalized to the corrected mass yields as calculated above. The normalization is done by a numerical integration over each track length or diameter distribution and equating the total area to the mass yield in the laboratory system. i.e. for a typical distribution the normalization factor N is obtained from the evaluation of (see also equation A18)

$$N_{A_1} = Y_{A_1} \left\{ \int_0^{\bar{L}_{A_1} - T_{A_1}^2} \exp\left[\frac{T_{A_1}^2 \ (2L - 2\bar{L}_{A_1} + T_{A_1}^2)}{2W_{A_1}^2}\right] dL \right.$$

$$+ \int_{\bar{L}_{A_1} - T^2_{A_1}}^{\infty} \exp \frac{\left| L - \bar{L}_{A_1} \right|^2}{2W^2_{A_1}} \, dL \Bigg\} \qquad \text{(A24)}$$

where Y_{A_1} is the yield in mass for fragment A_1, and all other symbols are those used in section 1.5

1.7 Summation

The final step in the calculation of the track length or diameter is to sum the track length or diameter distributions for all individual fragment mass values over the range of masses considered. For the simple case of glass detectors:

$$W_D = \sum_{A=1}^{A_T} \left\{ N_A \exp \left[- \frac{\left| D - \bar{D}_{A_2} \right|^2}{2W^2_A} \right] \right\} \qquad \text{(A25)}$$

2. Using RADICS on the S.F.U. I.B.M. 370/155 computer

The program makes extensive use of temporary and permanent data files on direct access devices. Device assignments are as follows:

5 CARD READER

6 PRINTER

7 CARD PUNCH

8 DATA SET - INPUT: TRACK LENGTH OR DIAMETER-MASS-ENERGY TABLE

9 DATA SET - TEMP. (INPUT REPEAT)

10 DATA SET - TEMP. (INPUT REPEAT)

11 DATA SET - OUTPUT: CALCULATED TRACK LENGTH OR DIAMETER DISTRIBUTIONS

12 DATA SET - INPUT: EXPERIMENTAL TRACL LENGTH OR DIAMETER DISTRIBUTIONS

14 DATA SET - TEMP.: INTERNALLY CALCULATED TRACK LENGTH OR DIAMETER MASS-ENERGY TABLE

Because of the multitude of input parameters a semi-conversational input language was devised so as to reduce errors in the input data. All input cards have a (A6, 4X, 2A4, 2X, 6F10.4) input format with only two exceptions as described below. All cards start with a main code word, which indicates the nature of the input parameters as well as the operations that are executed immediately. The second code word starting in column 11 and having a maximum of 8 characters specifies the options of the main code word and/or the meaning of up to six numerical parameters starting in column 21, 31, 41, 51, 61 and 71. In table A5, all possible input cards are listed with the variuos options and a brief description of the numerical parameters which can be entered.

Below we will discuss these code words and the direct results of the commands in more detail.

TITLE This command has no other meaning than that it expects to read a 20A4 card next and stores this for use as a heading on printed output.

INITIATE This command does not have any sub-code words and does no calculations. It only serves to enter five basic parameters. The mass and charge of the target and projectile as well as the fission barrier for that system. If the fission barrier is entered as zero, the calculated value (Mye 66) is substituted by the program.

RETABLE This command will result in the generation of a track length (or diameter)-mass-energy table. In the case of mica detectors only the mass and charge of the fissioning system are read in again to permit adjustments of these quantities for such effects as neutron evaporation. If RETABLE is <u>not</u> used then it is assumed that an identical table is already available on device 8 (disc).

ETOTAL Two options are available: THEORY AND EXP. In the case that theory is used the kinetic energy release of the system for symmetric fission is extracted from the data due to Nix (Nix 69). In the case of EXP, this value is read in as one of the numerical parameters. The other two numerical parameters which are read in, relate to the calculation of the excitation energy of the fissioning nucleus. This can be taken as any percentage of the initial excitation energy corresponding to compound nucleus formation. From

this the nuclear temperature is calculated, and this is used to extract an estimate of the width of a gaussian distribution in the total kinetic energy from the data due to Nix.

ENERGY In its present version the program calculates the energy of each possible fragment using a touching spheres approximation for the dependence on mass asymmetry of the kinetic energy release. The laboratory angle of observation is entered as well as the angular resolution. The target thickness, which is also entered is used to calculate the average loss as well as dispersion.

MASS This command serves to enter distributions in fragment mass, i.e. to associate a relative probability factor to each mass number. Up to five of these distributions can be used at the same time in later calculations. Every distribution that is entered therefore receives a label. Hereafter we will refer to five initiators. Each of these initiators can contain a mass distribution and a derived distribution, such as a track length distribution. Commands that involve calculations with arrays stored in the initiators always will have an option, which will allow the "switching on or off" on any or all of these initiators.

In the MASS command the first numerical parameter, therefore, refers to the number of the initiator (1 through 5) into which the described mass distribution will be stored. The sub-code word describes the type of mass distribution, while the other numerical parameters contain the relevant shape parameters.

MCORRECT This command will correct the mass distribution for center-of-mass motion. Any or all of the initiators can be corrected by switching them on (1.0) or off (0.) using the first five numerical parameters as representations of the five initiators.

Warning: since knowledge of the laboratory angle is essential, an ENERGY command should have preceded the MCORRECT command.

RANGE In its present version the program will convert energy-mass data to track length or diameter data for mica and glass detectors respectively. It will use the tables generated by the RETABLE command or use the data supplied on device 8. The lightest mass that can be 'seen' by the detector is entered as a numerical parameter. The track length or diameter of all fragments lighter than this limit is set equal to zero.

WIDTH This command will generate the shape parameters of the track length or diameter distribution for each

fragment mass. The two sub-code words refer to the shape of the distribution in track length or diameter which would be obtained with heavy ions with a known constant mass and energy. The FWHM value as well as the tailing parameter entered, should, therefore, correspond to such a distribution. It will use these values as well as the dispersion in the energy (converted into track length or diameter units), to calculate the overall shape parameters for each distribution associated with a particular fragment mass.

SUM — Summing of individual fragment mass track length (diameter) distributions can only be done if the commands RANGE and WIDTH did precede the SUM command. Any or all of the initiators can be used to generate master distributions in the same way as was discussed under MCORRECT. After this command, a series of normalization constants is generated by comparisons of the area of the distribution for each fragment mass with the calculated yield for that particular fragment. The distributions for all possible fragment masses are summed, weighting each distribution with the appropriate normalization factor.

REPEAT — The REPEAT command takes a special place among the other commands, in so far that the REPEAT

command is only used to control other command cards. Very often it is necessary to repeat a calculation with only a few changes in parameters. As long as these changes are in commands which do not relate directly to any other commands, a change will not result in having to rewrite the whole procedure. However, most commands result in calculations which will have a direct bearing on the calculations of other commands. It was for this reason that a "repeat" facility was designed. A good example of the usefullness of this facility is the calculation of track length distributions at a number of laboratory angles of observation. The procedure would look as follows:

```
TITLE
   EXAMPLE A
INITIATE              108.     47.     4.     2.    51.
ETOTAL     EXP         77.    100.    80.
REPEAT     START
ENERGY     SPHERES     10.      5.     .1
MASS       SINGLE       1.     50.
MCORRECT                1.
RANGE      MICA        26.
WIDTH      TAIL          .2      .3
SUM                     1.
PLOT       RANGE        1.
REPEAT     RETURN
REPEAT     ANGLE       20.      5.
REPEAT     ANGLE       30.      5.
STOP
```

The section of the calculations that needs to be repeated for each laboratory angle is put between the two commands REPEAT-START and REPEAT-RETURN.

Any time after this when another REPEAT command is found the sub-code word indicates the change in the REPEAT loop which will be made, and the whole loop is executed once more with this change. A number of different quantities can be changed using this procedure; the laboratory angle and the angular resolution; the projectile energy and the amount of excitation energy still present just before fission, the total kinetic energy release of the system and the mass and charge of the target material. If two quantities are varied simultaneously a double looping system is used, as will be illustrated with the same example as before. This time we want to calculate at three different angles but also at three different projectile energies.

The following commands would be necessary:

```
TITLE
   EXAMPLE B
INITIATE            108.    47.     4.     2.     51.
REPEAT    START
ETOTAL    EXP        77.   100.    80.
ENERGY    SPHERES    10.     5.     1.
MASS      SINGLE      1.    50.
MCORRECT              1.
RANGE     MICA       26.
WIDTH     TAIL         .2     .3
SUM                   1.
PLOT      RANGE       1.
REPEAT    CONTINUE
REPEAT    ANGLE      20.     5.
REPEAT    ANGLE      30.     5.
REPEAT    RETURN
REPEAT    ENERGY    100.    80.
REPEAT    ENERGY    120.    80.
STOP
```

The REPEAT-CONTINUE command terminates the first loop in this case. A track length distribution is therefore generated nine times using this procedure.

EXPERIM This serves to enter a measured track length or diameter distribution into initiator 5. One of the 5 initiators is used, so that the experimental data can be normalized to the same total area as the calculated distributions, and hence represented in the same plot as the calculated distributions. Since the array spacing is 0.05 mg/cm^2 for mica and .25 microns for glass, any experimental distribution is converted to this grid size. In order to facilitate this the histogram interval of experimental data should be given in units of mg/cm^2 (mica) or microns (glass).

Warning: it will replace whatever the contents of initiator 5 were.

PRINT Various amounts of printed output can be obtained by choosing the appropriate sub-code word:

HEAD, only a small summary of input quantities is given.

TABLES, a summary of mass yield factors as well as range and width parameters is printed.

WIDTH, a detailed analysis of contributing factors to the total width of the individual distributions for given fragment mass.

ALL, prints all the above.

RANGES, part or all of the track length (diameter)-mass-energy tables is printed.

PLOT This command will produce a print-plot of mass distributions (sub-code MASS) or track length (diameter) distributions (sub-code RANGE). Any or all of the five initiators can be plotted at the same time by switching them on or off as for MCORRECT.

DUMP This will result in the contents of any or all of the initiators being written on a disc file. Only the track length (diameter) distributions are written out.

PUNCH Will do the same operation as DUMP, except that the distributions are punched out on cards.

The following three examples together with Table A5 should explain the use of the command cards even further.

Example 1

Problem: You want to obtain track length distributions in mica for the system of 80 MeV α's + Te assuming a mass distribution with a single gaussian width of 30, 60 or 100 amu at a laboratory angle of 90°. Assume that the fission barrier is 50 MeV.

Control cards necessary:

```
TITLE
   EXAMPLE NO. 1
INITIATE              128.      52.      4.      2.     50.
ETOTAL     THEORY      80.     100.
ENERGY     SPHERES     90.       5.      .1
MASS       SINGLE       1.      30.
MASS       SINGLE       2.      60.
MASS       SINGLE       3.     100.
MCORRECT                1.       1.      1.
RANGE      MICA        26.
WIDTH      TAIL          .2       .3
SUM                     1.       1.      1.
PLOT       RANGE        1.       1.      1.
PRINT      ALL
STOP
```

Example 2

Problem: You want to determine the sensitivity of the final range distributions to the magnitude of the tailing parameter. Again take 80 Mev α 's + Te and a mass distribution with a single gaussian width of 60 amu.

Control cards necessary:

```
TITLE
   EXAMPLE NO. 2
INITIATE            128.      52.      4.      2.     50.
ETOTAL    THEORY     80.     100.
ENERGY    SPHERES    90.       5.      .1
MASS      SINGLE      1.      60.
MASS      SINGLE      2.      60.
MASS      SINGLE      3.      60.
MASS      SINGLE      4.      60.
MASS      SINGLE      5.      60.
MCORRECT              1.       1.      1.      1.      1.
RANGE     MICA       26.
WIDTH     TAIL         .2      .15
SUM                   1.
WIDTH     TAIL         .2      .20
SUM                             1.
WIDTH     TAIL         .2      .25
SUM                                     1.
WIDTH     TAIL         .2      .30
SUM                                             1.
WIDTH     TAIL         .2      .35
SUM                                                     1.
PLOT      RANGE        1.      1.      1.      1.      1.
PRINT     ALL
STOP
```

Example 3

Problem: You want to write on a disc file as well as punch out on cards the track diameter distributions which are calculated for the system 80 MeV α 's + Te at laboratory angle intervals of 20 degrees. Assume a single gaussian mass distribution with a width of 40 amu.

Control cards necessary:

```
TITLE
   EXAMPLE NO. 3
INITIATE              128.      52.     4.      2.     50.
ETOTAL    THEORY       80.     100.
REPEAT    START
ENERGY    SPHERES      20.       5.      .1
MASS      SINGLE        1.      40.
MCORRECT                1.
RANGE     MICA         26.
WIDTH     TAIL           .2       .3
SUM                     1.
DUMP                    1.
PUNCH                   1.
REPEAT    RETURN
REPEAT    ANGLE        40.       5.
REPEAT    ANGLE        60.       5.
REPEAT    ANGLE        80.       5.
REPEAT    ANGLE       100.       5.
REPEAT    ANGLE       120.       5.
REPEAT    ANGLE       140.       5.
REPEAT    ANGLE       160.       5.
STOP
```

Table A5 Code Words and Options

MAIN CODE WORD column 1-10	sub-code word column 11-20	numerical parameters starting in columns 21, 31, 41, 51, 61 and 71
INITIATE	--	(1) target mass (amu) (2) target charge (3) projectile mass (amu) (4) projectile charge (5) fission barrier (MeV)
ETOTAL	THEORY	(1) projectile energy (MeV) (2) % of excitation energy left when fissioning
	EXP	(1) projectile energy (MeV) (2) % of excitation energy left when fissioning (3) kinetic energy release for symmetric fission (MeV)
ENERGY	SPHERES	(1) laboratory angle of observation (2) angular resolution (3) target thickness (mg/cm^2)
	SPHEROIDS	--- as yet not available
MASS	SINGLE	(1) initiator (one to five) (2) FWHM of the single gaussian (amu)

Table A5 (continued)

MAIN CODE WORD column 1-10	sub-code word column 11-20	numerical parameters starting in columns 21, 31, 41, 51, 61 and 71
MASS	DOUBLE	(1) initiator (one to five) (2) FWHM of the two gaussian peaks (amu) (3) separation between the peaks (amu)
	TRIPLE	(1) initiator (one to five) (2) FWHM of the outer two gaussian peaks (amu) (3) separation between the outer peaks (amu) (4) FWHM of the center peak (5) relative height of center to outer peaks
MCORRECT	--	(1) initiator one on/off 1./0. (2) initiator two on/off 1./0. (3) initiator three on/off 1./0. (4) initiator four on/off 1./0. (5) initiator five on/off 1./0.
RANGE	MICA	(1) lower detector threshold (amu)
	GLASS	(1) lower detector threshold (amu)
	MAKROFOL	-- as yet not available
WIDTH	GAUSSIAN	(1) FWHM due to straggling

Table A5 (continued)

MAIN CODE WORD column 1-10	sub-code word column 11-20	numerical parameters starting in columns 21, 31, 41, 51, 61 and 71		
WIDTH	TAIL	(1) FWHM due to straggling		
		(2) tailing parameter		
SUM	--	(1) initiator one	on/off	1./0.
		(2) initiator two	on/off	1./0.
		(3) initiator three	on/off	1./0.
		(4) initiator four	on/off	1./0.
		(5) initiator five	on/off	1./0.
RETABLE	MICA	(1) mass of fissioning system (amu)		
		(2) charge of fissioning system		
	GLASS			
DUMP	--	(1) initiator one	on/off	1./0.
		(2) initiator two	on/off	1./0.
		(3) initiator three	on/off	1./0.
		(4) initiator four	on/off	1./0.
		(5) initiator five	on/off	1./0.
PUNCH	--	(1) initiator one	on/off	1./0.
		(2) initiator two	on/off	1./0.
		(3) initiator three	on/off	1./0.
		(4) initiator four	on/off	1./0.
		(5) initiator five	on/off	1./0.

Table A5 (continued)

MAIN CODE WORD column 1-10	sub-code word column 11-20	numerical parameters starting in columns 21, 31, 41, 51, 61 and 71		
PRINT	ALL			
	TABLES			
	HEAD			
	WIDTH			
	RANGES	(1) starting mass number (amu) (2) stop mass number (amu) (3) interval size (amu)		
PLOT	MASS	(1) initiator one	on/off	1./0.
		(2) initiator two	on/off	1./0.
		(3) initiator three	on/off	1./0.
		(4) initiator four	on/off	1./0.
		(5) initiator five	on/off	1./0.
	RANGE	(1) initiator one	on/off	1./0.
		(2) initiator two	on/off	1./0.
		(3) initiator three	on/off	1./0.
		(4) initiator four	on/off	1./0.
		(5) initiator five	on/off	1./0.

Table 5A (continued)

MAIN CODE WORD column 1-10	sub-code word column 11-20	numerical parameters starting in columns 21, 31, 41, 51, 61 and 71
TITLE	--	should always be followed by a 20A4 title card
REPEAT	START	
	CONTINUE	
	RETURN	
	ANGLE	(1) laboratory angle (2) angular resolution
	ENERGY	(1) projectile energy (MeV) (2) % of excitation energy left when fissioning
	ETOTAL	(1) kinetic energy release for symmetric fission (MeV)
	INITIATE	(1) target mass (2) target charge
EXPERIM	IDISC	(1) number of channels (2) starting channel (3) step or bin size

Table A5 (continued)

EXPERIM	READ	(1) number of channels (2) starting channel (3) step or bin size
	--------if the read sub-code word is used the experimental spectrum should follow immediately using a 10F5.0 input format.	

Appendix 2 Conversion of the three dimensional coordinate system of scattering chambers to the two dimensional coordinate system of mica detectors.

The three dimensional coordinate system can be defined by the cartesian coordinates x, y and z. The origin of this system is taken to be the beam spot on the target (idealized as a point). The x coordinate is perpendicular to the beam direction in the horizontal plane of the beam, y is measured alson the beam direction while z follows the axis of the scattering chamber (see figure A2.1). The two dimensional coordinate system (x', y') of the mica surface is shown in figure A2.2. Its origin is taken to be the point at which the y axis is the first coordinate system intersects the mica surface. The common point B is the tip of the cone of which the mica surface is a part. Under the assumption that the target is properly centered in the scattering chamber, this point will lie on the z-axis as well as on the y'-axis.

Defining the distance OA as d (where O is the target spot) so that the distance BA = D = d/cos , where is the angle at which the mica is oriented with respect to the beam direction, and also defining $\alpha = x'/(y' + D)$ where x' and y' are the coordinates of a point P in (x',y') space. The coordinates of the intercept I (x'_I, y'_I) of the line BP with the circle M are given by:

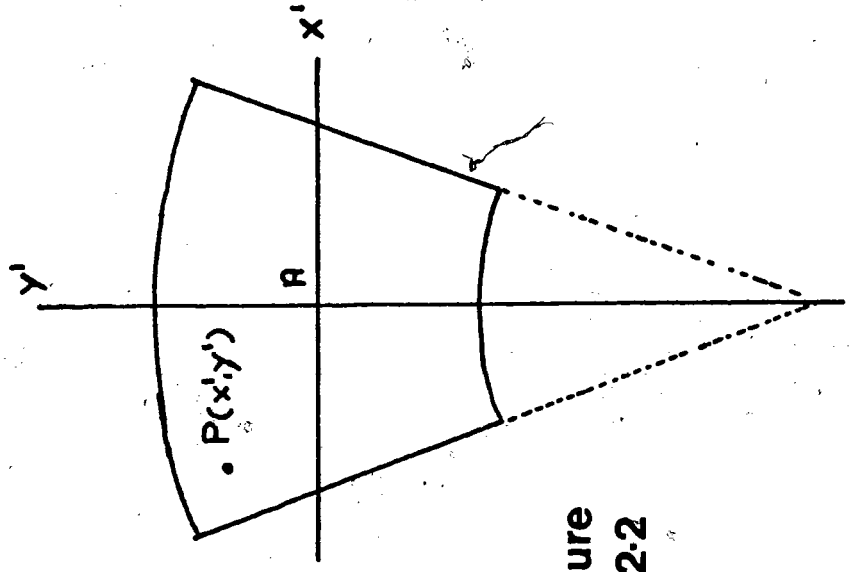

figure A2·2

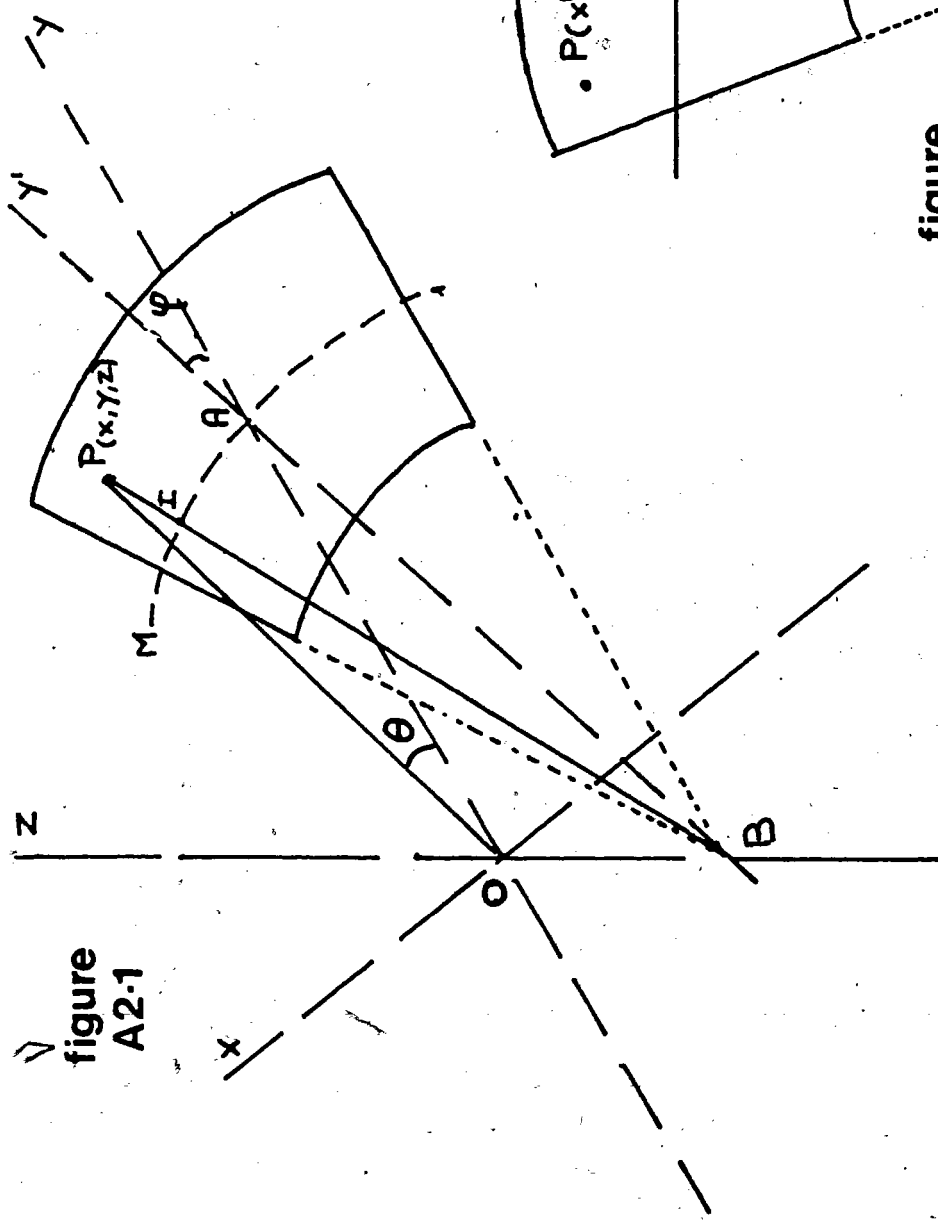

figure A2·1

$$y'_I + D(\sqrt{(1 + \alpha^2)^{-1}} - 1) \; ; \quad x'_I = y'_I D + \alpha D$$

It can be shown that the two coordinate systems are then related by the following set of equations:

$$x = b \sin \phi$$

$$y = b \cos \phi$$

$$z = a \sin$$

where $$a = \sqrt{x'^2 + (y'+D)^2} - \sqrt{x'^2_I - (y'_I+D)^2}$$

$$b = d + a \cos$$

$$\phi = \frac{a + D}{b} \arctan \alpha$$

Also the angle θ (the angle between lines OA and OP) at which the fragment is emitted to arrive at point P is given by

$$\theta = \arctan \{\sqrt{z^2 + x^2} / y\}$$

Appendix 3 FISMAP - fission-evaporation competition program.

1. Description of the program

The computer program FISMAP, written in the FORTRAN IV language, is based on the formulation presented in chapter 5. Treatment of particle evaporation is, at least in principle, identical to the method used in the SFUSMAP program (Rud 68). Fission competition is calculated for each "nuclear state" of the initial compound nucleus in a E - I matrix. The step sizes in this matrix are 2 MeV and 2 units of angular momentum, with maximum values of 200 MeV and 100 $\hbar$ units of angular momentum. (i.e. a matrix with a maximum size of 100 X 50). The probability of fission from each nuclear state is summed with the probability of emitting a neutron, proton and alpha particle from that state and all these probabilities are then normalized to the population of that state. The intermediate output consists of the distribution in nuclear states of the neutron, proton and alpha particle daughters as well as the distribution in nuclear states of the residual nucleus (i.e. those states from which particle evaporation or fission is not possible because of energy restrictions). The distribution in nuclear states of those nuclei that fissioned is also stored for later output. After this first first cycle in the calculation, the program uses the output of the distribution in E and I of the neutron daughter as the next nucleus in the de-excitation chain and repeats the above mentioned calculations. It continues to repeat these calculations

for sucessive neutron daughters until particle evaporation and fission is no longer possible from any of the nuclear states of the nucleus under consideration, or, until it has reached a given maximum number of evaporated neutrons, specified as input for the calculations. The program will then start this cycle all over again for the proton daughter of the initial compound nucleus. This sequence of calculations assures that all possible contributions to the distribution in nuclear states of a nucleus are added up before decay of the nucleus is considered in the calculations.

A vast amount of data is needed before these calculation can be performed. Inverse reaction cross-sections, binding energies, fission barriers and level density parameters are only a number of these parameters which enter into the main calculation. Instead of entering all this information as input data to the program these parameters are calculated internally with a number of options being specified to make adjustments to take into account some experimentally observed effects which are not included in the theoretical calculations. Provisions have, however, been made to enter all these data as input to the program.

2. Organization of the program

The program consists of a main program and some 20 subroutines. The main program performs the bulk of the calculations with

the aid of the subroutines BRANCH and FISSIO, which calculate the probability of particle evaporation and fission from any nuclear state respectively. Of the remaining subroutines, three are used to assist in the handling of the large data sets, while the others calculate the input parameters for the main calculation. Fig. A3.1 shows in a schematic diagram the organization of the program.

The program is still in a rather crude form and could use a considerable amount of further optimization to reduce both core requirements (presently as much as 640K bytes) and the execution time (typically hours of CPU time). Core requirements are high because of the generous use of "Direct Access Files" (a FORTRAN IV feature which allows the random access of files on direct access devices) which require large amounts of buffer space. The use of these files does, however, reduce the overall execution time requirements somewhat. The direct access files themselves take up another 13 million bytes of storage on either disk or tape.

3. Using the FISMAP program

Input data for the program can (usually) be entered on no more than three cards:

CARD 1 title card

format (20A4)

any 80 characters can be entered

figure A3-1

organization of the FISMAP program

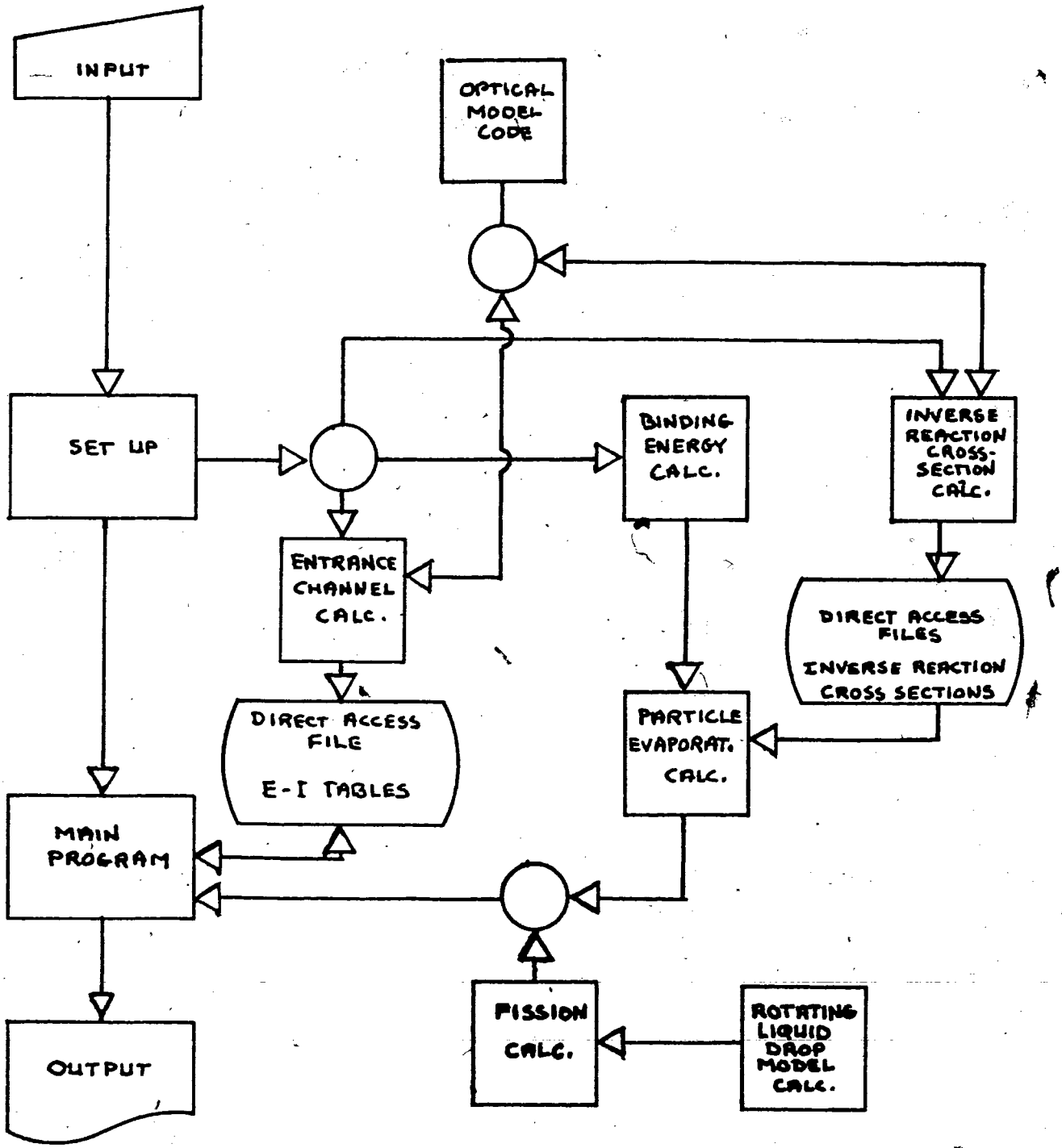

CARD 2 data card

format (8E10.3)

columns	name	description
1 - 10	AT	target mass
11 - 20	ZT	target charge
21 - 30	AP	projectile mass
31 - 40	ZP	projectile charge
41 - 50	Q	Q value of the reaction. If zero is entered the program will calculate Q.
51 - 60	ELAB	Laboratory Kinetic energy of the projectile
61 - 70	AFAN	ratio of fission to projectile level density parameters.

CARD 3 option control card

format (40I2)

columns	name	description
1 - 2	IHBZ	number of protons that are allowed to be evaporated from the compound nucleus (maximum 9)
3 - 4	IMBN	number of neutrons that are allowed to be evaporated from the compound nucleus (maximum 11)
5 - 6	ITL	If left blank the transmission coefficients used for calculating inverse cross sections are only calculated for

		the initial compound nucleus. If set to 1, the transmission coefficients will be recalculated for each nucleus in the de-excitation chain.
7 - 8	IENTR	If left blank the initial distribution in angular momentum of the compound nucleus is calculated using an optical model code. If set to 1 the program will read in the partial absorption cross section for each L value of the entrance channel. (see optional card 6)
9 - 10	IPAIR	If left blank no pairing energy corrections are made in calculating the level densities. If set to 1, a crude approximation is used to calculate pairing energies while if set to 2, the program will read in pairing energies (see option card 5)
11 - 12	IFISS	If left blank, the competition from fission in the de-excitation of the excited nucleus is taken into account. If set to -1, fission barrier penetration and reflection is also considered, while if set to +1, fission is assumed not to compete

13 - 14	MMC	If left blank, the binding energies which are calculated from the Myers and Swiatecki mass formula include shell effects. If set to 1, no such correction is made
15 - 16	MMP	If left blank, pairing energies are not included in the binding energy calculations. For MMP=1, the binding energies are adjusted for pairing effects. In this latter case IPAIR is automatically set to 1, unless IPAIR=2 was specified
17 - 18	IBARF	If left blank that fission barier calculated from the rotating liquid drop model are not corrected for shell effects. If set to 1 this correction is included.
19 - 20	IBIND	If left blank the binding energies are calculated from the Myers and Swiatecki mass formula. For IBIND=1, the program will read in the binding energies (see optional card 4). For IBIND=2, mass excess values are read in from which binding energies are calculated (see optional card 4)

Optional cards

CARDS 4 Binding energies (IBIND=1)

format (3F10.4)

The neutron, proton and alpha particle binding energies (in MeV) are entered of all nuclei in the IHBZ X IHBN matrix.

Mass excess values (IBIND=2)

format (6F10.4)

The mass excess values (in MeV) of the nuclei in the (IHBZ+2) X (IHBN+2) matrix are read in

CARDS 5 Pairing energy corrections (IPAIR=2)

format (11F5.2)

Pairing energy correction values (in MeV) are entered for all nuclei.

CARDS 6 Entrance channel data (IENTR=1)

format (5E10.3)

Partial absorption cross section values (in mB) are entered starting with the value for L=0. The last value should be zero, even if this means inserting a blank card.

Output of the program consist mainly of the yield of all evaporation products (in mB) in the specified IHBZ X IHBN matrix as well as the yield of those nuclei that fissioned within the limits of that same matrix. Also given are the distribution

in excitation energy and angular momentum of all evaporation products as well as the fissioning nuclei.

References:

Ale 60 J.M. Alexander and M.F. Gazdik, Phys. Rev. 120 (1960) 874

Ara 65 N.K. Aras, M.P. Menon and G.E. Gordon, Nuc. Phys. 69 (1965) 337

Bas 73 R. Bass, Phys. Lett. 47B (1973) 139

Bat 63 G.L. Bate, R. Chaudhry and J.R. Huizenga, Phys. Rev. 131 (1963) 722

Bec 68 K. Becker, Biophysik 5 (1968) 207

Beh 71 A.N. Behkami, Nucl. Data Tables 10 (1971) 1

Bel 59 S.T. Belyaev, Mat. Fys. Medd. Dan. Vid. Selsk. 31 (1959) 11

Ben 69 E.V. Benton and R.P. Henke, Nuc. Inst. & Methods 67 (1969) 87

Ber 61 R. Beringer and W.J. Knox, Phys. Rev. 121 (1961) 1195

Bet 37 H.A. Bethe, Rev. Mod. Phys. 9 (1937) 69

Bim 71 R. Bimbot and Y. Lebeyec, J. de Physique 32 (1971) 243

Bla 66 M. Blann, Nucl. Phys. 80 (1966) 223

Bla 68 M. Blann, Phys. Rev. Letters 21 (1968) 1357

Bla 70 M. Blann and F.M. Lanzafame, Nucl. Phys. A142 (1970) 559

Bla 71 M. Blann, Phys. Rev. Letters 27 (1971) 337

Bla 71b M. Blann, University of Rochester Report UR-3591-20 (1971), University of Rochester, Rochester, New York

Bla 72 M. Blann and F. Plasil, Phys. Rev. Lett. 29 (1972) 303

Bla 73 M. Blann and F. Plasil, "ALICE, a nuclear evaporation code", U.S.A.E.C. Report COO-3494-10 (1973) (unpublished)

Bod 62 D. Bodansky, Ann. Rev. Nucl. Sci. 12 (1962) 79

Boh 36 N. Bohr, Nature 137 (1936) 344

Boh 39 N. Bohr and J.A. Wheeler, Phys. Rev. 56 (1939) 426

Bra 67 R. Brandt, F. Cabonara, E. Cieslak, M. Dakowski, Ch. Gfeller, H. Piekarz, J. Piekarz, W. Riesler, R. Rinzivillo, E. Sassi, M. Sowinski and J. Zakrzewski, Nuc. Phys. A90 (1967) 177

Bra 71 R. Brandt, F. Carbonara, E. Cieslak, H. Piekarz, J. Piekarz and J. Zakrzewski, CERN report 71-2 (1971), European Organization for Nuclear Research Geneva

Bra 72 M. Brack, J. Damgaard, A.S. Jensen, H.C. Pauli, V.M. Strutinski and C.Y. Wong, Rev. Mod. Phys. 44 (1972) 320

Bre 36 G. Breit and E. Wigner, Phys. Rev. 49 (1936) 519

Bur 64 D.S. Burnett, R.C. Gatti, F. Plasil, P.B. Price, W.J. Swiatecki and S.G. Thomson, Phys. Rev. 134 (1964) B952

Cha 62 R. Chaudhry, R. Vandenbosch and J.R. Huizenga, Phys. Rev. 126 (1962) 220

Cof 58 C.T. Coffin and I. Halpern, Phys. Rev. 112 (1958) 536

Coh 74 S. Cohen, F. Plasil and W.J. Swiatecki, Ann. Phys. 82 (1974) 557

Dav 65 J.A. Davies, L. Eriksson and R. Jespergaard, Nuc. Inst. & Methods 38 (1965) 245

Fas 66 B. Fastrup, P. Hvelpund and C.A. Sautter, Kgl. Danske Videnskab Selskab. Mat. Fys. Medd. 35 (1966) no. 10

Fer 73 R.L. Furguson, F. Plasil, H. Freisleben, C.E. Bemis Jr. and H.W. Schmitt, Phys. Rev. C8 (1973) 1104

Fle 64 R.L. Fleischer, P.B. Price, R.M. Walker and E.L. Hubbard, Phys. Rev. 133 (1964) a1443

Fle 65 R.L. Fleischer, P.B. Price and R.M. Walker, Ann. Rev. Nuc. Sci. 15 (1965) 1

Fon 69 P. Fong, "Statistical Theory of Nuclear Fission", Gordon & Breach, New York, 1969

Fra 47 S. Frankel and N. Metropolis, Phys. Rev. 72 (1947) 914

Fra 66 J.S. Fraser and J.C.D. Milton, Ann. Rev. Nuc. Sci. 16 (1966) 379

Gin 67 J.E. Gindler and J.R. Huizenga, in "Nuclear Chemistry" (1. Yaffe ed.), Vol II, Chapter 7, Academic Press, New York, 1967

Gol 70 Ch. Goldstein, These d'Universite, Orsay, France 1970

Gri 63 J.J. Griffin, Phys. Rev. 132 (1963) 316

Gri 66 J.J. Griffin, Phys. Rev. Letters 17 (1966) 478

Hal 55 I. Halpern and V.M. Strutinski, Proc. of the First United Nations International Conf. on the Peaceful Uses of Atomic Energy, Geneva (1955), (United Nations, New York, Vol. 15, p. 408 (1958))

Hal 59 I. Halpern, Ann. Rev. Nuc. Sci. 9 (1959) 245

Hen 71 R.P. Henke and E.V. Benton, Nuc. Inst. & Methods 97 (1971) 483

His 60 J.R. Hiskes, University of California Lawrence Radiation Laboratory Report UCRL-9275 (1960)

Hof 56 R. Hofstadter, Rev. Mod. Phys. 28 (1956) 214

Hon 71 S. Hontzeas and H. Blok, Phys. Scripta 4 (1971) 229

Hop 69 U. Hoppner, E. Konecny and G. Fiedler, Nuc. Inst. & Methods 74 (1969) 285

Hud 69 J. Hudis and S. Katcoff, Phys. Rev. 180 (1969) 1122

Hui 62 J.R. Huizenga and R. Vandenbosch, in "Nuclear Reactions" (P.M. Endt and P.B. Smith, eds.), Chapter II, North-Holland Publ., Amsterdam (1962)

Hui 62b J.R. Huizenga, R. Chaudhry and R. Vandenbosch, Phys. Rev. 126 (1962) 210

Hui 65 J.R. Huizenga in "Nuclear Structure and Electromagnetic Interactions" (N. MacDonald ed.), Plenum, New York, 1965

Hui 69 J.R. Huizenga, A.N. Behkami and L.G. Moretto, Phys. Rev. 177 (1969) 1826

Hyd 64 E.K. Hyde, "Nuclear Properties of the Heavy Elements", Vol III, Fission Phenomena, Prentice Hall, Englewood Cliffs, New Jersey (1964)

Igo 59 G. Igo, Phys. Rev. 115 (1959) 1665

Itk 72 M.G. Itkis, K.G. Kuvatov, C.N. Okolovich, G. Ya. Ruskina, G.N. Smirenkin and A.S. Tishin, Yad. Fiz. 16 (1972) 258, translated in Sov. J. Nuc. Phys. 16 (1973) 144

Joz 71 K. Jozefowicz, Nuc. Inst. & Methods 93 (1971) 359

Kas 72 V.I. Kasilov, A.V. Mitrofanova, Yu.N. Ranyuk and P.V. Sorokin, Yad. Fiz. 15 (1972) 406, translated in Sov. Journal of Nuc. Phys. 15 (1972) 228

Kho 66 A. Khodai-Joopari, Thesis Rep. UCRL-16489, Univ. of California, Berkley (1966)

Kie 73 F.M. Kiely and B.D. Pate, Nuc. Inst. & Methods 109 (1973) 355

Kon 65 V.A. Konshin, E.S. Matesevich and V.I. Regushevski J. Nuc. Phys (USSR) 2 (1965) 682, translated in Sov. J. Nuc. Phys. 2 (1966) 489

Lam 62 R.W. Lamphere, Nucl. Phys. 38 (1962) 561

Lan 63 D.W. Lang, Proc. of the Third conf. on Reactions between Complex Nuclei, ed. by A. Ghiorso, R.M. Diamond and H.E. Conzett, U. of Cal. Press, Berkley, D9, 248 (1963)

Lan 63b D.W. Lang, Nucl. Phys. 42 (1963) 353

Lec 71 M. Lecerf, These de Troisieme Cycle, Institute de Physique Nucléaire, Orsay, France, 1971

Lec 72 M. Lecerf and J. Péter, Nuc. Inst & Methods 104 (1972) 189

Lin 63 J. Lindhard, M. Scharff and H.E. Sciøtt, Kgl. Danske Videnskab Selskab. Mat. Fys. Medd. 33 (1963) no. 14

Mei 39 L. Meitner and O.R. Frisch, Nature (London) 143 (1939) 239

Met 71 T. Methasiri and S.A.E. Johansson, Nuc. Phys. A167 (1971) 97

Mig 59 A.B. Migdal, Nucl. Phys. 13 (1959) 655

Mor 70 L.G. Moretto and R. Stella, Phys. Lett. B32 (1970) 558

Mye 66 W. Myers and W.J. Swiatecki, Nuc. Phys. 81 (1966) 1

Nak 69 H. Nakahara, J.W. Harvey and G.E. Gordon, Can. J. Phys. 47 (1969) 2371

Nat 70 J.B. Natowitz, Phys. Rev. C1 (1970) 623

Nat 72 J.B. Natowitz, E.T. Chulick and M.N. Namboodiri, Phys. Rev. C6 (1972) 2133

Nic 60 W.J. Nicholson Jr., Ph. D. thesis, University of Washington (1960) (unpublished)

Nix 65 J.R. Nix and W.J. Swiatecki, Nucl. Phys. 71 (1965) 1

Nix 67 J.R. Nix, Ann. Phys. 41 (1967) 52

Nix 69 J.R. Nix, Nucl. Phys. A130 (1969) 241

Nix 72 J.R. Nix, Ann. Rev. Nuc. Sci. 22 (1972) 65

Nor 70 L.C. Northcliffe and R.F. Schilling, Nuc. Data Tab. 47 (1970) 233

Orm 63 J.H. Omrod and H.E. Duckworth, Can. J. Phys. 41 (1963) 1424

Par 63 J.T. Park and E.J. Zimmerman, Phys. Rev. 131 (1963) 1611

Pat 71 B.D. Pate and J. Péter, Nuc. Phys. A173 (1971) 520

Pik 58 G.A. Pik-pichak J.E.T.P. 34 (1958) 341, English translation: Sov. Phys. JETP 7 (1958) 238

Pik 62 G.A. Pik-pichak J.E.T.P. 42 (1962) 1294, English translation: Sov. Phys. JETP 15 (1962) 897

Pik 62b G.A. Pik-pichak J.E.T.P. 43 (1962) 1701, English translation: Sov. Phys. JETP 16 (1963) 1201

Pla 66 F. Plasil, D.S. Burnett, M.C. Britt and S.G. Thompson, Phys. Rev. 142 (1966) 696

Pla 73 F. Plasil, R.L. Ferguson and F. Pleasonton, paper IAEA-SM-174/71 in Proc. Third IAEA Symposium on the Physics and Chemistry of Fission (Rochester New York, 1973)

Pre 40 R.D. Present and J.K. Knipp, Phys. Rev. 57 (1940) 751

Pre 46 R.D. Present, F. Reims and J.K. Knipp, Phys. Rev. 70 (1946) 557

Pre 63 M.A. Preston, Physics of the Nucleus, Addison Welsey, Reading, Massachusetts (1963)

Pri 71 P.B. Price and R.L. Fleischer, Ann. Rev. Nuc. Sci. 21 (1971) 295

Ral 69 J. Ralarosy, R. Schmitt, G. Mosinski, J. Tripier, M. Debeauvais, R. Stein and G. Remy, Le Journal de Physique 39 (1969) 1

Ral 71 J. Ralarosy, J. Tripier, R. Stein, G. Remy and M. Debeauvais, Le Journal de Physique 32 (1971) 733

Ral 73 J. Ralarosy, M. Debeauvais, G. Remy, J. Tripier, R. Stein and D. Huss, Phys. Rev. C8 (1973) 2372

Ram 70 V.S. Ramamurthy, S.S. Kapoor and S.K. Kataria, Phys. Rev. Lett. 25 (1970) 386

Rei 66 R.F. Reising, G.L. Bate and J.R. Huizenga, Phys. Rev. 141 (1966) 1161

Rud 68 F.H. Ruddy, Ph. D. thesis, Simon Fraser University (1968) (unpublished)
F.H. Ruddy, B.D. Pate and E.W. Vogt, Nucl. Phys. A127 (1969) 323

Rut 11 E. Rutherford, Phil. Mag. 21 (1911) 669

Sar 67 D.G. Sarantites and B.D. Pate, Nucl. Phys. A93 (1967) 545

Sar 71 E.J. Hoffman and D.J. Sarantites, Nucl Phys. 173 (1971) 177, and Nucl. Phys. A180 (1972) 177; J.H. Barker and D.G. Sarantites, Phys. Rev. C9 (1974) 607; D.G. Sarantites, J.H. Barker and N.H. Lu, Phys. Rev. C9 (1974) 603

Sau 65 C.A. Sautter and E.J. Zimmerman, Phys. Rev. 140 (1965) A490

Sel 59 E.C.H. Selk and R.S. Barnes, Phil. Mag. 4 (1959) 970

Sik 62 T. Sikkeland, E.L. Haines and V.E. Viola Jr., Phys. Rev. 125 (1962) 1350

Spe 74 H.J. Specht, Rev. Mod. Phys. 46 (1974) 773

Str 67 V.M. Strutinsky, Nucl. Phys. A95 (1967) 420

Tep 62 Y.A. Teplova, V.S. Nikolgev, I.S. Dmitriev and L.N. Fateeva, Sov. Phys. JETP 15 (1962) 31

Tho 64 T.D. Thomas, Nucl. Phys. 53 (1964) 558

Van 72 R. Vandenbosch and U. Mosel, Phys. Rev. Lett. 28 (1972) 1726

Van 73 R. Vandenbosch and J.S. Huizenga, "Nuclear Fission", Academic Press, New York and London, 1973.

Var 70 M. Varnagy, J. Csikai, S. Szagedi and S. Nagy, Nuc. Inst. & Methods 89 (1970) 27

Vio 71 V.E. Viola Jr., M.M. Minor, A.E. Salwin, R.O. Bondelid and R.B. Theus, Nucl. Phys. A174 (1971) 321

Vio 74 V.E. Viola Jr., C.T. Roche, W.G. Meyer and R.G. Clark, Report MNC-4028-0014 (1974) (University of Maryland, College Park, Maryland)

Wei 40 V.F. Weiskopf and D.H. Ewing, Phys. Rev. 57 (1940) 472

Whe 63 J.A. Wheeler, in "Fast Neutron Physics", (J.B. Marion and J.L. Fowler, eds.), Wiley (Interscience), New York (1963)

Wil 64 L. Wilets, "Theory of Nuclear Fission", Oxford Univ. Press (Clarendon), London and New York, 1964

Wil 72 F.C. Williams Jr., G. Chan and J.R. Huizenga, Nucl. Phys. A187 (1972) 225

Wil 73 J. Wilczynski, Nucl. Phys A216 (1973) 166

Zeb 74 A.M. Zebelman, L. Kowalski, J. Miller, K. Beg, Y. Eyal, G. Jaffe, A. Kandil and D. Logan, Phys. Rev. C10 (1974) 200